Interactive effects of ocean acidification with other environmental drivers on marine plankton

Alexandra R. Bausch

Submitted in partial fulfillment of the
requirements for the degree
of Doctor of Philosophy
in the Graduate School of Arts and Sciences

Columbia University

2018

Abstract

Interactive effects of ocean acidification with other environmental drivers on marine plankton

Alexandra R. Bausch

Planktonic organisms form the base of the marine food web and may be impacted by environmental change in many ways. The interactive effects of multiple, simultaneous climate-driven changes on these organisms are not well understood. This dissertation examined the impacts of ocean acidification in combination with other environmental stressors on marine plankton and determined spatial patterns of one of these potential interactive drivers. Chapter 2 investigated the synergistic effects of ocean acidification and hypoxia on the harmful dinoflagellate *Amphidinium carterae*. Findings indicated that empirical studies may be crucial to accurately predict organismal responses to multi-stressors. Results also suggested that photorespiration may serve a previously unrecognized role in dinoflagellate metabolism. Chapter 3 examined the combined effects of ocean acidification and lithogenic trace metals on the growth of another harmful dinoflagellate, *Cochlodinium polykrikoides*. Results indicated that high suspended sediment loads may deliver toxic concentrations of trace elements to marine phytoplankton in acidified coastal ecosystems. Chapter 4 examined the interactive effects of ocean acidification and bacteria on the severity and extent of dissolution in the shells of larval gastropods and the adult pteropod *Limacina helicina*. Research findings indicated that microbial communities on the shell surfaces of some planktonic molluscs may mediate certain types of shell dissolution in acidified, upwelled waters. Chapter 5 explored the use of thorium isotope fluxes as a proxy for dust and lithogenic iron in the Indian Ocean. Results suggested that the gradient of dust fluxes in the region could impose thresholds for biological productivity. Together, these interdisciplinary studies demonstrate coupled biological and chemical changes in marine ecosystems as a result of increased anthropogenic environmental change.

Table of contents

List of figures

List of tables

Acknowledgments

As in my research, nothing in my life exists in isolation. I would like to gratefully acknowledge financial support from the Columbia University Dean's Fellowship, the NASA Earth and Space Science Fellowship, and the Chevron Student Initiative Fund. I am deeply grateful for the support and encouragement from my doctoral research advisor Andrew Juhl, whose excellent, practical advice and patient guidance made me a better writer, teacher, and scientist. I also want to thank the other members of my dissertation committee for their continued support and invaluable feedback: Robert Anderson, Hugh Ducklow, Kevin Griffin, and Christopher Hayes. I sincerely want to thank Sonya Dyhrman for welcoming me into the Dyhrman lab family and becoming my unofficial mentor; Sheean Haley for being such an absolute joy to work beside and sharing so many delicious baked goods; and all the members of the Dyhrman lab for being such thoughtful, collaborative office mates and such dear friends. I want to thank my undergraduate mentor, Amanda Grannas, who included me in unique research opportunities that not only enriched my professional trajectory but also made me a better human being. I would also like to thank Martin Fleisher, whose patience and technical expertise (and strong coffee) were greatly appreciated; Peter Morton for teaching me everything I ever wanted to know about measuring trace metals and inviting me to so many wonderful family dinners; Terrie Klinger and Jonathan Havenhand for being such strong advocates for my work and such positive role models; Kimberly Popendorf and Beth Stauffer for teaching me the fundamentals of ocean science outside the classroom; Allison Jacobel and Ángel Muñoz for assisting me with LaTeX; and all the members of the Columbia community who made me feel like I belonged. I would like to acknowledge Dyson, my canine companion, for being my stress relief, my confidant, and my little buddy. I want to thank my friends and family for unconditional support, laughter, encouragement, silliness, patience, empathy, and so much love. I would like to dedicate this dissertation to my mom, who was my most enthusiastic supporter and who always encouraged me to follow my heart. Finally, I want to thank my husband, Andreas, for being endlessly patient, loving, and inspiring. For being my calm and my voice of reason. For being my best friend. I'm so glad we met in the Southern Lehigh High School cafeteria.

For my mom, Pamela

Chapter 1

Introduction

1.1 Background and motivation

Anthropogenic climate change, predominantly caused by increases in atmospheric carbon dioxide (CO_2) from fossil fuel combustion and industrial operations, has already led to a cascade of simultaneous effects in the ocean including warming, ocean acidification, deoxygenation, and changing marine food webs (Breitberg et al., 2015). These stressors threaten the health of marine ecosystems (Halpern et al., 2008) and trigger wide-ranging perturbations to fisheries yields and broader ecological communities (Klinger et al., 2017).

Although some impacts of rising atmospheric CO_2 are widely recognized (e.g., ocean acidification), the consequences of climate change in combination with other concurrent climate-driven environmental drivers are not well understood. Empirical studies are essential to address the cumulative anthropogenic impacts on marine ecosystems and ultimately provide insights to management and policy decision-makers. This dissertation focuses on the following fundamental questions: (1) what are the implications of ocean acidification in conjunction with other co-occurring stressors (e.g., deoxygenation, lithogenic trace metal toxicity, microbial activity) on marine plankton and (2) how can the supply of aerosol iron delivered from dust inform thresholds of biological productivity? The interdisciplinary research outlined in this dissertation aims to address these questions using a wide variety of research approaches.

1.1.1 Planktonic organisms

Plankton – organisms that drift with ocean currents – are sensitive indicators of climate change (Hays et al., 2005). Many of these floating organisms, including phytoplankton and zooplankton, serve as the base of the marine food web and play crucial roles in the global carbon cycle (Falkowski, 2012).

Phytoplankton are single-celled, largely autotrophic organisms that drift in the euphotic zone – the sunlit, upper layers of the ocean (Falkowski, 2012). Phytoplankton growth and primary production – the synthesis of organic matter from CO_2 – depend on photosynthesis to convert sunlight into chemical energy. Rates of photosynthesis rely on the availability of light, carbon, and macro- and micronutrients (e.g., iron; Fe). In the light-dependent reactions of photosynthesis, cells use light to oxidize water, release oxygen (O_2), and generate high-energy electrons to produce energy (adenosine triphosphate; ATP) and reducing equivalents (nicotinamide adenine dinucleotide phosphate; NADPH). In the subsequent light-independent reactions – collectively known as the Calvin cycle – cells use ATP and NADPH to incorporate ("fix") CO_2 and ultimately form sugars and other organic molecules required for growth (Peterhansel et al., 2010). Cells can also use O_2 as a substrate instead of CO_2 in a diversion from carbon fixation known as photorespiration. Although photorespiration is energetically expensive (Peterhansel et al., 2010), it serves important roles in balancing the light-dependent and -independent reactions of photosynthesis (Bagby and Chisholm, 2015) and maintaining cell function, particularly under stress conditions (Bauwe et al., 2010).

Zooplankton are heterotrophic plankton that drift or weakly swim with ocean currents. These organisms may exist in the plankton for their entire lives (holoplankton) or for a portion of their life cycles in early development stages (meroplankton; Hays et al., 2005). Zooplankton play important roles in the flow of energy and nutrients between autotrophic phytoplankton and higher trophic levels (Gazeau et al., 2013; Hays et al., 2005) and the export of carbon to the deep ocean (Manno et al., 2017).

Understanding the impact of climate change on both phytoplankton and zooplankton is a key issue in numerous current research efforts (Doney et al., 2012; Hays et al., 2005). Climate change differentially impacts many species of marine plankton (Doney et al., 2009):

for example, some increase growth or survival rates as a result of changing nutrient concentrations or decreasing predation pressure (known as ecological "winners"); others decrease growth or physiological performance as a result of suboptimal environmental conditions (so-called "losers"); others are relatively unaffected (Doney et al., 2012; Dutkiewicz et al., 2013). However, the effects of multiple, concurrent climate-driven stressors on marine plankton are not well understood. Therefore, it is essential to demonstrate how marine planktonic organisms – both at the individual and community level – respond to anthropogenic changes in ocean chemistry.

1.1.2 Ocean acidification

The unprecedented rate of increase of CO_2 in the atmosphere has been tempered by the ocean, which has absorbed nearly one third of anthropogenic CO_2 (Sabine et al., 2004). However, the oceanic uptake of atmospheric CO_2 is not without consequence. It causes fundamental changes in ocean chemistry and decreases in pH together known as ocean acidification (Caldeira and Wickett, 2003). The seawater carbonate chemistry associated with ocean acidification is relatively straightforward (Figure 1.1). CO_2 not only dissolves in seawater, it reacts with it to form carbonic acid (H_2CO_3). H_2CO_3 then dissociates by losing hydrogen ions (H^+) to form bicarbonate (HCO_3^-) and carbonate (CO_3^{2-}) ions (Doney et al., 2009). In addition, aqueous H_2CO_3 reacts with CO_3^{2-} to form HCO_3^-. Increasing the amount of CO_2 in the atmosphere therefore increases aqueous CO_2, HCO_3^-, and H^+ concentrations. This increase in H^+ concentration causes a decrease in seawater pH:

$$pH = -\log_{10}[H^+] \tag{1.1}$$

Ocean surface pH has decreased by approximately 0.1 pH units over the past 150 years, corresponding to about a 30% increase in acidity (Doney et al., 2012), and is expected to decrease by an additional 0.3 to 0.5 pH units by the end of this century (Caldeira and Wickett, 2005). If CO_2 emissions continue to increase unabated over the next few centuries, the ocean may experience pH changes unlike anything experienced in the past 300 million years (Caldeira and Wickett, 2003).

Increasing the concentration of hydrogen ions in seawater also decreases the concentration of CO_3^{2-} ions (Figure 1.1), which are necessary for calcifying organisms (e.g., corals,

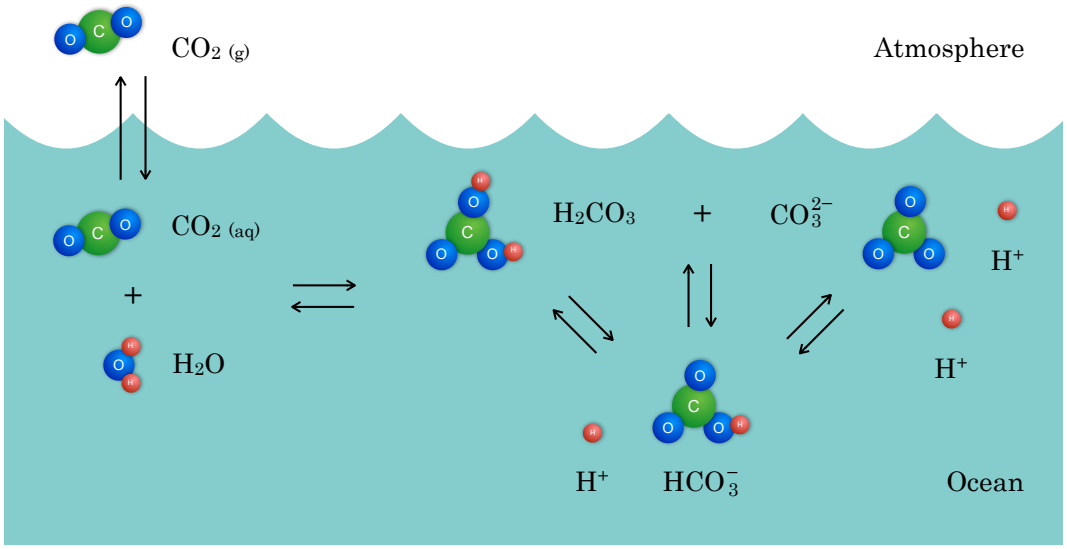

Figure 1.1: Chemical reactions governing seawater carbonate chemistry.

calcareous plankton) to build shells and skeletons out of calcium carbonate ($CaCO_3$; Doney et al., 2009). The impact on these calcifying organisms largely depends on the $CaCO_3$ saturation state (Ω) of seawater:

$$\Omega = \frac{[Ca^{2+}][CO_3^{2-}]}{K'_{sp}} \tag{1.2}$$

where K'_{sp} is the apparent solubility product for $CaCO_3$. Decreasing seawater Ω under ocean acidification conditions significantly impacts shelled organisms. In general, $CaCO_3$ formation occurs in regions where $\Omega > 1$ (i.e., saturated) and dissolution occurs where $\Omega < 1$ (undersaturated; Doney et al., 2009). Ocean acidification has already increased the extent of corrosive, undersaturated surface waters (e.g., Feely et al., 2008).

Although the biological responses to ocean acidification are wide-ranging and highly species-specific, fundamental changes in ocean chemistry will likely have severe consequences for both calcifying and non-calcifying plankton, as well as broader marine ecosystems (Doney et al., 2009; Guinotte and Fabry, 2008). One phytoplankton group of particular interest includes harmful algal bloom (HAB) species. Toxic dinoflagellates may be particularly sensitive to climate-driven changes. Blooms are often associated with eutrophication

– high nutrient inputs in coastal waters that cause high algal productivity in surface waters and oxygen depletion in the subsurface. The intensity and frequency of HAB blooms will likely increase with ocean acidification and with a number of other anthropogenic changes (Fu et al., 2012). Thus, understanding how combined environmental stressors impact HABs is of critical importance.

Among the zooplankton groups impacted by climate-driven stressors, planktonic marine shelled molluscs are of particular interest (Doney et al., 2009; Gazeau et al., 2013). Pteropods – holoplanktonic snails known as "sea butterflies" – are sensitive to changes in ocean chemistry and therefore serve as early indicators of anthropogenic ocean acidification (e.g., Bednaršek et al., 2012a; Manno et al., 2017). The thin shells of these molluscs are composed of aragonite, a relatively soluble form of $CaCO_3$, which is especially sensitive to dissolution (Guinotte and Fabry, 2008; Manno et al., 2017). Rapid degradation of the shell matrix has been shown to occur under acidic, low aragonite saturation state conditions (Ω_{arag}; e.g., Bednaršek et al., 2012b; Gazeau et al., 2013). It is essential to improve mechanistic understanding of shell dissolution under the influence of multiple climate-driven drivers.

1.1.3 Concurrent environmental drivers

Ocean acidification does not occur in isolation. Acidification can potentially interact with a number of other environmental stressors in marine ecosystems (e.g., increases in temperature and some macronutrients; decreases in O_2 and sea ice; changes in stratification, precipitation, and marine habitats), all of which have the potential to impact both autotrophs and heterotrophs (Breitberg et al., 2015; Halpern et al., 2008). The effects of these combined drivers can be additive, greater than the sum of the individual stressors (synergistic), or less than the sum (antagonistic; Boyd and Hutchins, 2012; Breitberg et al., 2015). This dissertation focuses on three processes occurring in concert with ocean acidification that may significantly impact marine plankton: decreasing O_2 levels, increasing lithogenic trace metal inputs, and changing microbial activity.

Ocean deoxygenation is a critical threat to marine organisms often occurring together with acidification. Low O_2 conditions are fundamentally linked to acidification via microbial

respiration, which releases CO_2 and consumes O_2 (Gobler and Baumann, 2016). Eutrophic, coastal waters are projected to become not only more deoxygenated but also more acidic in a process known as coastal acidification (Wallace et al., 2014). In addition, hypoxic zones – with O_2 levels below an operationally defined threshold – are predicted to expand and intensify with increased warming, high nutrient loads, and changes in stratification (Breitburg et al., 2018; Keeling et al., 2010). These regions are often called "dead zones" due to the potentially lethal impacts on marine life (Diaz and Rosenberg, 2008). The combination of hypoxia and acidification has been shown to synergistically impact some invertebrates (Baumann, 2016). However, the interactive effects of ocean acidification and hypoxia on phytoplankton have not previously been examined.

Anthropogenic climate change may also alter inputs of lithogenic trace metals to marine ecosystems. Lithogenic particles (e.g., suspended sediments or aerosol dust) contain bioactive trace metals including Fe, which can be beneficial to phytoplankton growth (e.g., Duce and Tindale, 1991; Martin, 1990). However, at high concentrations, some lithogenic trace metals can also be toxic (Jordi et al., 2012; Paytan et al., 2009). As a result of changing climate and land use, sediment loads are projected to increase in coastal ecosystems over the course of this century (Ito, 2007; Yang et al., 2003). Increasing atmospheric CO_2 may also increase desertification, mineral dust loads, and lithogenic trace metal inputs to some regions of the ocean (Mahowald et al., 2009; Woodward et al., 2005). However, long-term predictions of natural dust are highly uncertain (Mahowald et al., 2010). Ocean acidification conditions have been shown to cause changes in trace metal solubility and speciation (Hoffmann et al., 2012; Millero et al., 2009). It has also been demonstrated that sediments can release metals and other contaminants during disturbance events (Eggleton and Thomas, 2004). However, the combined effects of ocean acidification and lithogenic trace metals mobilized from suspended sediments on phytoplankton have not previously been assessed.

In addition to essential micronutrients and toxic trace metals, lithogenic particles also contain radionuclides including thorium (Th). In seawater, the isotopes ^{230}Th and ^{232}Th can be used to quantify aerosol dust supply and the supply of lithogenic Fe dissolved from dust. Both ^{230}Th (sourced from the decay of ^{234}U) and ^{232}Th (delivered from aeolian dust) are removed from the ocean by adsorption onto sinking particles in a process known as

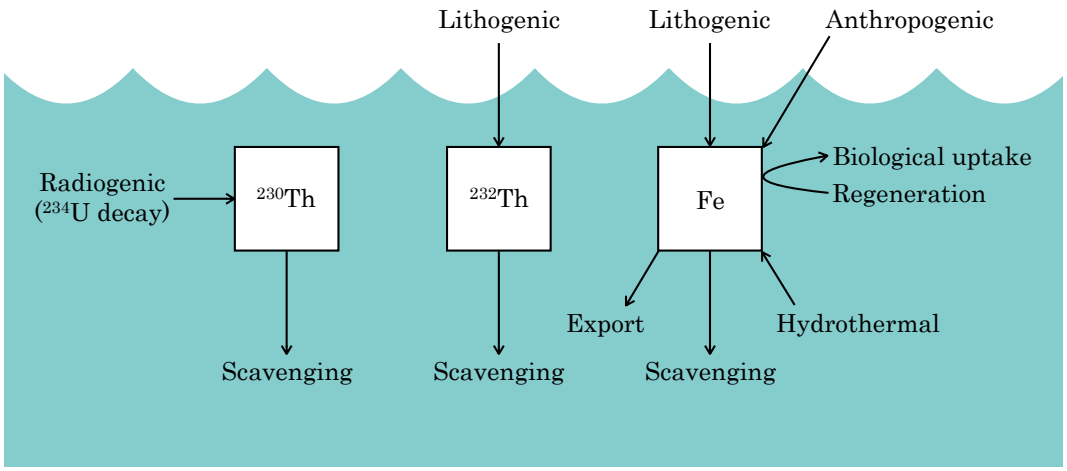

Figure 1.2: Sources and sinks of dissolved Th and Fe.

scavenging (Figure 1.2; Hayes et al., 2015b; Henderson and Anderson, 2003). Although the cycle of seawater Fe is far more complex than that for Th (Figure 1.2), ^{232}Th can be used as a tracer for aerosol Fe since both are sourced from dust (Hayes et al., 2015b). Th-based measurements are particularly useful to determine the spatial extent of dust deposition and the consequent thresholds of Fe availability in highly biologically productive marine ecosystems such as the Indian Ocean. However, Th-based inputs of dust and residence times of aerosol Fe in the Indian Ocean have not previously been measured.

Changing climate conditions may also influence microbial activity (e.g., bacterial production, degradation activity; Liu et al., 2010). Ocean acidification has been shown to increase rates of bacterial enzyme activity (e.g., Maas et al., 2013) and organic matter degradation (Liu et al., 2010). These climate-driven changes may impact bacteria living on the surface of shelled zooplankton. It is possible that shell-associated bacteria may influence the extent of aragonite shell degradation among gastropods (Clark, 1999; Glover and Kidwell, 1993) – particularly under ocean acidification conditions – but this has not previously been tested.

1.2 Dissertation overview

It is essential to use an interdisciplinary framework to address the multiple, simultaneous environmental stressors impacting marine planktonic organisms (Breitberg et al., 2015) and to address the knowledge gaps outlined above. Therefore, the overarching objective of this dissertation is to use diverse approaches to examine and help better predict the impacts of anthropogenic climate change on the base of the marine food web.

Part I of this dissertation uses controlled incubation experiments with marine plankton to examine the potential interactive effects of ocean acidification with other environmental stressors. Chapter 2 examines the impacts of acidification and hypoxia – both individually and in combination – on the HAB dinoflagellate species *Amphidinium carterae*. Chapter 3 focuses on the combined impacts of acidification and high suspended sediment concentrations on another HAB dinoflagellate, *Cochlodinium polykrikoides* (newly designated as *Margalefidinium polykrikoides*; Gómez et al., 2017). Chapter 4 examines the influence of acidification and shell-associated bacterial activity on gastropod larvae and the adult pteropod *Limacina helicina*. Part II of this dissertation uses Th isotopes to better characterize spatial patterns of a potential interactive environmental driver in marine ecosystems. Chapter 5 focuses on the inputs of atmospheric dust – a major source of Fe for phytoplankton – in surface waters of the Indian Ocean.

Part I

Effects of multiple stressors

Chapter 2

Synergistic negative effects of simulated acidification and hypoxia on the harmful dinoflagellate *Amphidinium carterae*

Note: A modified version of this chapter is in preparation as Bausch, A. R., Juhl, A. R., Donaher, N. A., and A. M. Cockshutt (in prep). Synergistic negative effects of simulated acidification and hypoxia on the growth, carbon metabolism, and photophysiology of the harmful dinoflagellate *Amphidinium carterae*.

2.1 Abstract

Hypoxia and ocean acidification frequently co-occur in coastal marine ecosystems. These combined stressors will likely become more intense and persistent with anthropogenic climate change. Although the separate effects of low seawater pH and low dissolved oxygen (O_2) concentrations have been previously described for some marine phytoplankton, the combined effects of these stressors are not known. This study is the first to use factorial experiments to show the interactive effects of acidification and hypoxia on the growth, metabolism, and photophysiology of a phytoplankton species. Multi-stressor incubation experiments were performed using the harmful dinoflagellate *Amphidinium carterae* to examine the effects of acidification and hypoxia both individually and in combination. Long- (7-d) and short-term (6-h) incubation experiments were performed under controlled dis-

solved carbon dioxide (CO_2) and O_2 conditions to examine the interactive effects of the stressors and to assess the underlying physiological mechanism driving the interaction. In the long-term experiment, synergistically negative effects were observed for *A. carterae* growth, carbon fixation, and photosynthetic efficiency under combined high CO_2 (low pH) and low O_2 concentrations. In the short-term experiment to examine the timescale for onset of physiological impacts, delayed recovery of photosystem II (PSII) reaction centers was observed following photoinhibition, suggesting high CO_2 (low pH) and low O_2 conditions negatively affect photosynthesis in relatively short periods of time. These findings suggest that the affinity of the enzyme ribulose-1,5-bisphosphate-carboxylase/oxygenase (RuBisCO) for CO_2 relative to O_2 may not predict *in vivo* organismal responses to dissolved CO_2 and O_2 concentrations. In *A. carterae*, it is possible that photorespiration is important in balancing the light-dependent and -independent reactions of photosynthesis, although other unmeasured mechanisms may also contribute. Therefore, the combined effects of low pH and O_2 concentrations may strongly impact the growth of some harmful dinoflagellates in coastal marine ecosystems.

2.2 Introduction

Ocean acidification is the ongoing decrease in ocean pH and change in seawater carbonate chemistry driven by the oceanic uptake of anthropogenic carbon dioxide (CO_2) from the atmosphere (Caldeira and Wickett, 2003; Doney et al., 2009). By the end of this century, atmospheric CO_2 concentrations are predicted to increase up to 1150 ppmv (IPCC, 2013), causing a decrease in the average surface ocean pH by 0.3-0.5 units (Caldeira and Wickett, 2005). These high CO_2 (low pH) conditions will have significant, wide-ranging consequences for many marine organisms (Doney et al., 2009; Guinotte and Fabry, 2008; Kroeker et al., 2013).

Coastal hypoxia is another critical threat to marine ecosystem health occurring in concert with ocean acidification. Low dissolved oxygen (O_2) conditions commonly occur in aquatic ecosystems as a result of microbial metabolic processes (Gobler and Baumann, 2016; Keeling et al., 2010). Hypoxic conditions, operationally defined as O_2 concentrations

< 62.5 μmol L^{-1} (Cai et al., 2011; Vaquer-Sunyer and Duarte, 2008), are often exacerbated by eutrophication in coastal waters. Eutrophication – high nutrient inputs leading to blooms of algae – typically causes high O_2 conditions in surface waters due to high photosynthesis and low O_2 conditions in the subsurface due to stratification and high microbial respiration (Cai et al., 2011; Diaz and Rosenberg, 2008). In some cases though, low O_2 conditions can characterize the whole water column (e.g., Gobler and Baumann, 2016). Over the course of this century, so-called hypoxic "dead zones" are predicted to significantly expand as a result of increased eutrophication in highly populated coastal zones (Diaz and Rosenberg, 2008; Gruber, 2011; Rabalais et al., 2010). Hypoxia will likely have serious negative impacts on marine organisms and ecosystems, since its effects can be lethal depending on the affected species (Diaz and Rosenberg, 2008).

Coastal acidification is a secondary effect of respiration-driven O_2 depletion in coastal zones (Wallace et al., 2014). While ocean acidification is driven by the uptake of atmospheric CO_2, coastal acidification is controlled by the biological production of CO_2. The same metabolic processes that drive hypoxia also release CO_2, thereby decreasing seawater pH (Cai et al., 2011; Sunda and Cai, 2012; Wallace et al., 2014). In stratified, eutrophic waters for example, high O_2 and low CO_2 conditions can occur near the surface together with low O_2 and high CO_2 conditions at depth, though with sufficient nutrient loading, hypoxic and acidic conditions can characterize the entire water column (e.g., Wallace et al., 2014). In addition, low O_2, high CO_2 conditions occur in deeper waters in natural oxygen minimum zones (OMZs; Gobler and Baumann, 2016; Rabalais et al., 2010). It is predicted that the frequency and intensity of low O_2, low pH zones will increase over the course of this century with enhanced climatic warming and eutrophication (Keeling et al., 2010; Rabalais et al., 2010). In addition, due to the strong coupling of hypoxia and coastal acidification in combination with ocean acidification, coastal waters with low O_2 may become disproportionately more acidic (Cai et al., 2011; Melzner et al., 2013).

Despite the co-occurrence of acidification and hypoxia in many coastal marine ecosystems and the likelihood of significant changes by the end of this century, little is known about the interactive effects of decreasing pH in conjunction with decreasing O_2 on marine organisms (Baumann, 2016). While many studies have examined the individual effects of

low seawater pH (e.g., Doney et al., 2009; Guinotte and Fabry, 2008; Kroeker et al., 2013) or low dissolved O_2 (e.g., Diaz and Rosenberg, 2008; Rabalais et al., 2010; Vaquer-Sunyer and Duarte, 2008), few studies have examined the combined effects of these environmental stressors (Gobler and Baumann, 2016) even though the combination of acidification and hypoxia may have stronger negative effects on some marine organisms than the sum of each individual stressor (Baumann, 2016; Guinotte and Fabry, 2008). Notably, experimental studies examining the interactive effects of hypoxia and acidification in marine ecosystems have focused on heterotrophic organisms (Baumann, 2016). These recent studies have shown synergistic negative effects of CO_2 and O_2 on the survival and fitness of some marine fish and invertebrates (DePasquale et al., 2015; Gobler et al., 2014). Nevertheless, autotrophic organisms including phytoplankton are also sensitive to changes in O_2 and CO_2 concentrations individually (e.g., Hattenrath-Lehmann et al., 2015; Wu et al., 2012), together (e.g., Bagby and Chisholm, 2015), and in combination with other stressors (e.g., Bausch et al., 2017; Fu et al., 2012). Among the phytoplankton taxa that are likely particularly sensitive to the combination of CO_2 and O_2 in coastal waters, harmful algal bloom (HAB) species are of particular interest. Given their potential for deleterious impacts and their connection to eutrophication in coastal systems (Fu et al., 2012), it is essential to understand the interactive impacts of high CO_2 and low O_2 concentrations on HAB species, such as toxin-producing dinoflagellates, in addition to other marine photoautotrophs.

Photoautotrophic organisms fix carbon using the enzyme ribulose-1,5-bisphosphate-carboxylase/oxygenase (RuBisCO). RuBisCO is likely affected by ambient CO_2 and O_2 concentrations because it catalyzes both photosynthesis (CO_2 fixation) and photorespiration (O_2 fixation) in the chloroplasts of photoautotrophic organisms (Bowes et al., 1971; Peterhansel et al., 2010). Despite the fact that it may be the most abundant protein on Earth (Ellis, 1979), RuBisCO has among the lowest catalytic efficiency of any biological catalyst (Tabita et al., 2007). This is because the enzyme has a slow catalytic turnover rate (Tabita et al., 2007) and a poor affinity for CO_2, which serves as a substrate for carbon fixation, due to competitive binding of O_2, a substrate for photorespiration (Foyer and Noctor, 2000). When the CO_2:O_2 ratio at the active site is high, RuBisCO uses CO_2 as a substrate for carbon fixation, resulting in the formation of 3-phosphoglycerate (3PGA), which is in-

tegrated into the Calvin cycle (Peterhansel et al., 2010). However, when the CO_2:O_2 ratio is low, RuBisCO uses O_2 as a substrate instead of CO_2, consuming O_2 and releasing CO_2. This oxygen fixation results in the formation of the toxic intermediate 2-phosphoglycolate (2PG), which is converted to 3PGA via photorespiration, consuming energy (ATP) and reducing equivalents (NADPH) and releasing ammonia (NH_3) and CO_2 (Bauwe et al., 2010; Peterhansel et al., 2010). Thus, maximal rates of photorespiration occur under low CO_2, high O_2 conditions (Foyer and Noctor, 2000). Since photorespiration is an energetically expensive diversion from carbon fixation, it is often perceived as a wasteful process (Peterhansel et al., 2010). However, photorespiration serves an important role in cell physiology by balancing the light-dependent and -independent reactions of photosynthesis (Bagby and Chisholm, 2015; Takeba and Kozaki, 1998). Photorespiration also recovers carbon in 2PG, removes toxic intermediates, protects cells from photoinhibition during stress conditions, and supports cell defense mechanisms (Bauwe et al., 2010; Peterhansel et al., 2010).

The capacity of RuBisCO to differentiate between the substrates CO_2 and O_2 (i.e., RuBisCO specificity; Tortell, 2000) is determined by its distinct structural form (Tabita et al., 2007) and the availability of CO_2 relative to O_2 (Foyer and Noctor, 2000). RuBisCO CO_2/O_2 specificity is highly taxon-specific and correlated with the atmospheric conditions of CO_2 and O_2 in the evolution of various phytoplankton taxa (Tortell, 2000). Most dinoflagellates contain form II RuBisCO (Jenks and Gibbs, 2000), which is particularly inefficient at discriminating between CO_2 and O_2 (Tabita et al., 2007). This structural form of RuBisCO may cause dinoflagellates to be particularly sensitive to ambient CO_2 and O_2 conditions compared to some other phytoplankton taxa (Eberlein et al., 2014; Tortell, 2000). Thus, dinoflagellates have a lower RuBisCO specificity than many other groups of phytoplankton.

Amphidinium carterae is a cosmopolitan, bloom-forming dinoflagellate found in temperate to tropical coastal and estuarine waters (Hargraves and Maranda, 2002; Steidinger and Jangen, 1996). It is considered a HAB species (Murray et al., 2012) and is known to produce toxic ichthyotoxins (Huang et al., 2009) and hemolytic substances (Echigoya et al., 2005). Since *A. carterae* has ecological importance, particularly in coastal marine environments (Hargraves and Maranda, 2002; Murray et al., 2012), and has published RuBisCO specificity measurements (Whitney and Andrews, 1998), it is an ideal model organism to

examine the effects of CO_2 and O_2. The measured RuBisCO substrate specificity of *A. carterae* is higher than that of any other form II RuBisCO found in anaerobic bacteria (Whitney and Andrews, 1998). However it is extremely low compared to that of other eukaryotic photoautotrophs, indicating a reduced affinity for CO_2 relative to O_2 (Whitney and Andrews, 1998; Young et al., 2016). It is therefore likely that *A. carterae* uses a carbon-concentrating mechanism (CCM) to concentrate CO_2 at the active site of RuBisCO (Badger et al., 1998; Burns and Beardall, 1987; Jenks and Gibbs, 2000; Whitney and Andrews, 1998), particularly in light of the large number of dinoflagellate genes involved in CCMs (Hennon et al., 2017). However, since *A. carterae* lacks external carbonic anhydrase (CA), its capacity for active bicarbonate uptake may be limited (Dason et al., 2004) and its growth may be stimulated at high CO_2 concentrations (Fu et al., 2012).

In this study, factorial experiments were performed using *A. carterae* to examine the impacts of simulated hypoxia and acidification both individually and in combination. Cultures were maintained in up to four experimental treatments: (1) control, which reflects current atmospheric levels of CO_2 and O_2; (2) high CO_2 (low pH), which reflects ocean acidification conditions associated with "worst-case scenario" CO_2 levels by 2100 (IPCC, 2013); (3) low dissolved O_2, which reflects coastal hypoxic conditions predicted to intensify by 2100 (Rabalais et al., 2010); and (4) combined high CO_2 and low dissolved O_2, which reflects co-occurring coastal acidification and hypoxia (Wallace et al., 2014). Both long- (7-d) and short-term (6-h) incubations were performed under these controlled CO_2 and O_2 conditions.

The primary objective of this study was to examine the interactive effects of acidification and hypoxia on *A. carterae*. Since cellular carbon metabolism is controlled by the concentrations of CO_2 and O_2 at the active site of RuBisCO, as well as the CO_2/O_2 specificity of RuBisCO (Foyer and Noctor, 2000; Tortell, 2000), *in vitro* RuBisCO specificity was hypothesized to predict *A. carterae* organismal responses to dissolved CO_2 and O_2 concentrations. Specifically, elevated CO_2 and low O_2 conditions were predicted to particularly benefit *A. carterae* growth, metabolism, and physiology since these conditions should drive carbon fixation and prevent oxygen fixation. Since findings from this study did not support this

hypothesis, the second research objective was to determine the physiological mechanism driving synergistic, negative effects at high CO_2 and low O_2 on an organismal level.

2.3 Materials and methods

2.3.1 Algal culture and medium

Axenic cultures of *Amphidinium carterae* (CCMP 1314; Hulburt, 1957), obtained from the National Center for Marine Algae and Microbiota, were grown in L1 medium without added silicate (Guillard and Hargraves, 1993). Medium was prepared using 0.2 μm-filtered (Pall Acropak), autoclave-sterilized coastal seawater collected from the University of Connecticut Avery Point Campus, Connecticut, USA (salinity = 32). Cultures were maintained at a temperature of 20°C and a light intensity of 100 μmol quanta m^{-2} s^{-1} (Dixon and Syrett, 1988) with a photoperiod of 13 hours light: 11 hours dark.

2.3.2 Long-term effects on growth, metabolism, and physiology

A. carterae cultures were maintained in four experimental treatments: (1) control (400 ppmv CO_2 and 21% O_2); (2) high CO_2 (1200 ppmv CO_2 and 21% O_2); (3) low dissolved O_2 (400 ppmv CO_2 and 2% O_2); and (4) combined high CO_2 and low dissolved O_2 (1200 ppmv CO_2 and 2% O_2). All experimental designs were consistent with recommendations from Cornwall and Hurd (2016). Responses were defined as synergistic when the combined effects of multiple drivers were greater than the additive effects of individual drivers (Breitberg et al., 2015).

Before each experiment, the medium in each culture flask was bubbled for at least 1 h using high-efficiency particulate air- (HEPA-) filtered 3-component compressed gas mixtures of CO_2 (400 or 1200 ppmv), O_2 (2 or 21%), and N_2 (balance). When the desired pH and dissolved O_2 levels were reached, bubbling was stopped and *A. carterae* cells were inoculated in the gas-amended media. To maintain constant pH and dissolved O_2 conditions while preventing shear stress from bubbling (e.g., Juhl and Latz, 2002), the culture flask headspaces were continuously purged with the corresponding compressed gas mixture. Gas flow rates were maintained at 0.1 LPM using needle valve flow meters (Cole Parmer).

Flasks were fitted with porous cheesecloth stoppers and swirled continuously on orbital shaker tables (45 RPM). Comparison to unshaken flasks suggested that shaking did not affect growth rate but did enhance gas diffusion.

Experiments were performed over 7 d to examine *A. carterae* responses following long-term exposure to treatment conditions. *A. carterae* cells were initially acclimated for 3 d under controlled pH and dissolved O_2 conditions with initial cell concentrations ranging from 4.4×10^3 to 6.6×10^3 cells mL^{-1} and final concentrations ranging from 1.9×10^4 to 3.9×10^4 cells mL^{-1} in each treatment. Acclimated culture was then inoculated in each of four replicate flasks in each of the four treatments with initial cell concentrations ranging from 8.5×10^2 to 1.2×10^3 cells mL^{-1}. Cultures were maintained for another 4 d under the same conditions as the acclimation with final cell concentrations ranging from 5.9×10^3 to 1.5×10^4 cells mL^{-1} in each treatment. Low cell concentrations minimized changes in pH and dissolved O_2 over time due to algal metabolism and were intended to be comparable to typical *in situ* concentrations.

Subsamples of *A. carterae* were collected daily, preserved in acid Lugol's solution (2% final concentration), and counted at 100× magnification (Axiostar Plus microscope, Zeiss). Growth rates for each flask were determined using the exponential growth equation of cell counts during the last four time points ($R^2 > 0.950$ in each case).

Estimates of *in vivo* chlorophyll *a* were determined daily using a handheld active fluorometer (*Aqua*Flash, Turner Designs) with a 10 × 10 mm square glass cuvette with blank correction using filtered culture media. Extracted chlorophyll *a* concentrations were measured at the end of each 7-d incubation. Culture samples (25 mL) were filtered onto GF/F filters (Whatman), stored at -20°C, and extracted in 10 mL of 90% acetone. Chlorophyll *a* concentrations of the extract were measured using the *Aqua*Flash fluorometer before and after acidification (Strickland and Parsons, 1972). The measured *in vivo* and extracted chlorophyll *a* values at the end of the 7-d incubation were linearly correlated ($R^2 = 0.83$, n = 16).

Measurements of dark minimum chlorophyll *a* fluorescence (Fo) and dark maximum fluorescence (Fm) were determined daily using the *Aqua*Flash fluorometer with blank correction

using filtered culture media. Potential quantum yield (Fv/Fm) was then calculated:

$$Fv/Fm = \frac{Fm - Fo}{Fm} \tag{2.1}$$

Dissolved O_2 concentrations were determined by subsampling from the culture flasks into glass scintillation vials fitted with non-invasive O_2 sensor spots (PSt3, PreSens). Dissolved O_2 concentrations were measured daily using a single-channel fiber optic O_2 transmitter with temperature, pressure, and salinity compensation (Fibox 4, PreSens).

Rates of dark respiration and net photosynthesis were determined at the end of the 7-d incubation by measuring changes in dissolved O_2 over 5 hours in dark (0 μmol quanta m^{-2} s^{-1}) and light (100 μmol quanta m^{-2} s^{-1}) scintillation vials, respectively. Rates of gross photosynthesis were determined based on differences between O_2 measurements in the light and dark vials. Note that this calculation assumes equivalent light and dark respiration rates and does not account for photorespiration. Slow diffusion into the scintillation vials in the low O_2 treatments could not be avoided, and thus low O_2 measurements were corrected by the rate of diffusion (1.83 μmol O_2 L^{-1} h^{-1}; $R^2 = 0.9652$, n = 3), measured in sterile seawater.

Measurements of pH on the total hydrogen scale (pH_T) were obtained daily using a modified version of the spectrophotometric method with 1 mL of sample and two 5-μL aliquots of *m*-cresol purple indicator (adapted from SOP 6b; Dickson et al., 2007). Spectroscopic measurements were performed using a double-beam UV-Vis spectrophotometer (UV-1800, Shimadzu), fitted with 20 mm path-length special optical glass spectrophotometric cells (18B-SOG-20, Starna). To ensure analytical quality control, sample pH values were calibrated against that of Tris buffer reference standard (Andrew Dickson, Scripps Institution of Oceanography; batch T28).

Total alkalinity (A_T) measurements were obtained at the beginning and end of the 7-d incubation experiment using the potentiometric titration method (SOP 3b; Dickson et al., 2007). Samples (140 mL) were fixed with saturated mercuric chloride solution (20 μL $HgCl_2$; 0.01% final concentration) and analyzed using an automatic potentiometric titrator (888 Titrando, Metrohm) with Tiamo software (version 2.5). Sample A_T values were calibrated against that of certified CO_2 reference material (Andrew Dickson, Scripps Institution of Oceanography; batches 149 and 156).

The partial pressure of CO_2 (pCO_2) in each flask was calculated from temperature, salinity, pH_T, and A_T data using CO_2calc (Robbins et al., 2010) with the dissociation constants of Mehrbach et al. (1973), as refit by Dickson and Millero (1987).

Nutrient samples were collected at the beginning and end of the 7-d incubation experiment. Samples were 0.22 μm syringe-filtered and stored at -20°C. Concentrations of ammonium, nitrate, nitrite, and phosphate were measured at the Nutrient Analytical Services Laboratory at the Chesapeake Biological Laboratory using a discrete analyzer (Konelab Aquakem 250, Thermo Scientific). Briefly, dissolved inorganic ammonium, nitrite, and orthophosphate were determined using automated colorimetry; dissolved inorganic nitrate plus nitrite was determined using the enzyme catalyzed reduction method.

Samples for isotopic analysis were collected at the end of the 7-d experiment to determine the natural carbon and nitrogen isotopic signatures (δ^{13}C and δ^{15}N, respectively) of the *A. carterae* cells. Culture samples (150 mL) were filtered onto combusted GF/F filters (Whatman), stored at -20°C, and freeze-dried. In addition, a labeling incubation experiment using stable isotope tracers (^{13}C and ^{15}N) was performed to determine changes in natural isotopic composition following ^{13}C/^{15}N labeling due to carbon and nitrogen uptake (e.g., Raven, 1997). Culture samples (200 mL) were incubated under treatment conditions with a final concentration of 1 mM ^{13}C-labeled sodium bicarbonate (< 50% of DIC) and 0.5 mM ^{15}N-labeled sodium nitrate (< 50% of L1 nitrate) for 3 h. At the end of the 3-h incubation, samples (150 mL) were filtered onto combusted GF/F filters (Whatman), stored at -20°C, and freeze-dried.

All isotopic analyses were performed at the Stable Isotope Laboratory at Lamont-Doherty Earth Observatory. Sample filters were weighed, encapsulated into tin capsules, and stored in a desiccator until analysis. Briefly, stable isotope δ^{13}C and δ^{15}N values were analyzed via the combustion method using an elemental analyzer (ECS 4010, Costech) fitted with a universal continuous flow interface (ConFlo IV, Thermo Scientific) and an isotope ratio mass spectrometer (Delta V, Thermo Scientific). Carbon and nitrogen contents were calibrated by acetanilide. Carbon isotope (δ^{13}C) measurements were calibrated by three-point regression of natural isotope standards (USGS40, USGS41, and USGS24). Similarly, nitrogen isotope (δ^{15}N) measurements were calibrated by standard regression (USGS40,

USGS41, and IAEA-N3). It is important to note that even the enriched samples following $^{13}C/^{15}N$ labeling were determined by extrapolation of these three-point regressions using natural abundance isotope standards. Therefore, the enriched $\delta^{13}C$ and $\delta^{15}N$ data may be skewed and may have larger errors than those reported here. However, the $\delta^{13}C$ and $\delta^{15}N$ signatures were only compared among treatments in this experiment and therefore represent relative values.

Samples for total protein and RuBisCO content were collected at the end of the 7-d incubation experiment. *A. carterae* culture samples (100 mL) were filtered onto 0.8-μm polycarbonate filters (Nucleopore, Whatman), folded cell-to-cell, cryo-preserved in liquid nitrogen, and stored at -80°C.

Protein extractions were prepared using the FastPrep-24 and bead lysing "matrix D" (MP Biomedicals), with 3 cycles of 60 s at 6.5 m s^{-1} in 500 μL of 1× extraction buffer (AS08 300, Agrisera) containing 0.4 mM 4-(2-aminoethyl)benzenesulfonyl fluoride hydrochloride (AEBSF; Bioshop Canada), then spun at 16,000 g for 8 min. The supernatant was assayed for total protein content using the detergent compatible (DC) assay kit against bovine γ-globulin (BGG) standard (Bio-Rad), then prepared for electrophoresis based on equivalent total protein loads using 1× lithium dodecyl sulfate (LDS) sample buffer (Life Technologies) and 50 mM dithiothreitol (DTT) heated for 5 min at 70°C. Separation of proteins was performed in a Bolt 4-12% Bis Tris sodium dodecyl sulfate polyacrylamide gel electrophoresis (SDS-PAGE) gel (Life Technologies) with 200 V power for 40 min alongside a molecular marker (MagicMark, Life Technologies), then transferred to a polyvinylidene difluoride (PVDF) membrane (Bio-Rad) for 60 min using 30 V. Each gel also had a four-point quantitation curve using the large subunit of RuBisCO (RbcL) Form II (AS15 2955S, Agrisera).

Membranes were blocked for 1 h in $2\%_{w/v}$ enhanced chemiluminescence (ECL) blocking agent (GE Healthcare) dissolved in Tris-buffered saline and Tween (TBS-T, containing 20 mM Tris, 137 mM NaCl, $0.1\%_{v/v}$ Tween-20), then incubated in 1:20,000 rabbit polyclonal anti-RbcL Form II antibody for 1 h (AS15 2955, Agrisera) and finally in 1:20,000 goat anti-rabbit IgG horseradish peroxidase (HRP) conjugated antibody (AS09 602, Agrisera) for 1 h. After each antibody incubation, membranes were rinsed with TBS-T solution five times.

Chemiluminescent images were obtained using ECL Select reagent (GE Healthcare) and a VersaDoc charge coupled device (CCD) imager (Bio-Rad). Band densities for samples were determined against the standard curve using ImageLab software (version 4.0, Bio-Rad).

2.3.3 Short-term impacts on metabolism

Short-term experiments were performed over 6 h using the same basic experimental design as the long-term experiments but without an acclimation period. Stock *A. carterae* culture was transferred to four replicate flasks in each of the four treatments with initial cell concentrations ranging from 6.6×10^3 to 8.4×10^3 cells mL^{-1}. Cells were incubated for 6 h to examine rates of respiration and photosynthesis following short-term exposure to treatment conditions.

Measurements of cell counts, *in vivo* chlorophyll *a*, Fv/Fm, dissolved O_2, pH_T, A_T, and pCO_2 were determined at the beginning of the 6-h incubation as described above. At the end of the incubation, rates of dark respiration, gross photosynthesis, and net photosynthesis, as well as Fv/Fm were determined as described above.

2.3.4 Short-term impacts on photophysiology

Additional short-term experiments were performed to examine photophysiology responses under two of the treatment conditions: (1) control and (2) combined high CO_2, low dissolved O_2. Stock *A. carterae* cells were inoculated with initial cell concentrations ranging from 3.3×10^4 to 4.8×10^4 cells mL^{-1} in each of three replicate flasks. Cells were incubated for 6 h to assess the timescale of photophysiology responses of *A. carterae* following short-term exposure to treatment conditions.

Cell counts, *in vivo* chlorophyll *a*, Fv/Fm, dissolved O_2, and pH_T were determined at the beginning of the 6-h incubation as described above. Measured A_T from the previous short-term experiment was used to calculate pCO_2 values since the same medium was used in both experiments. At the end of the incubation, Fv/Fm was measured as described above. In addition, light curves (Brooks and Niyogi, 2011) were measured at the end of the incubation using a xenon pulse amplitude modulated (PAM) fluorometer (Xe-PAM, Walz) with blank correction using filtered culture media. Cultures were subsampled into

fluorescence cuvettes, sealed, and dark-adapted for 5 min (Possmayer et al., 2011). Samples were exposed to a very low-intensity measuring light (Schreiber et al., 1993) pulsed at 2 Hz to measure Fo, following by a saturating light flash (4000 μmol quanta m^{-2} s^{-1}) for 0.8 s to measure Fm (Cao et al., 2011; Possmayer et al., 2011). Samples were then illuminated using the actinic halogen source at eight consecutive, increasing light levels up to 1700 μmol quanta m^{-2} s^{-1} for 1 min each, with superimposed saturation flashes every 1 min (Possmayer et al., 2011) to measure steady-state fluorescence under actinic light (F) and maximum fluorescence under actinic light (Fm′). Effective quantum yield under actinic illumination (Fv′/Fm′) was calculated:

$$Fv'/Fm' = \frac{Fm' - F}{Fm'} \tag{2.2}$$

The relative electron transport rate (ETR) was also determined at each actinic light level (as in Wu et al., 2010):

$$ETR = Fv'/Fm' \times I \times 0.84 \times 0.5 \tag{2.3}$$

where I is the actinic light intensity, the coefficient 0.84 indicates that 84% of incident light was absorbed by the sample, and the coefficient 0.5 indicates that 50% of absorbed quanta reached photosystem II (PSII). Photosynthesis-irradiance (PI) curves were generated by plotting the relative ETR as a function of actinic light intensity. Note that ETR was not normalized to biomass and therefore represents only a relative measure of photosynthesis. Following exposure to actinic light, six consecutive saturation pulses were applied to examine dark recovery of quantum yield up to 18 min after illumination. The coefficients of photochemical quenching (qP) and non-photochemical quenching (NPQ) were also determined during dark recovery:

$$qP = \frac{Fm' - F}{Fm' - Fo} \tag{2.4}$$

$$NPQ = \frac{Fm - Fm'}{Fm'} \tag{2.5}$$

PAM data were obtained using WinControl software (version 2.08, Walz).

2.3.5 Statistical analyses

Data were analyzed using Prism GraphPad software (version 7). Linear regressions, paired t-tests at 95% confidence, and one-way analyses of variance (ANOVA) with Fisher's least significant difference (LSD) *post hoc* tests were used to determine significant differences in measurements among treatments. Note that many of the figures use letters to denote statistical significance: variables with different letters are significantly different, while variables with the same letter are not.

2.4 Results

2.4.1 Long-term effects on growth, metabolism, and physiology

Growth rates of *Amphidinium carterae* calculated from exponential increases in cell counts (Figure A.1 in the Appendix) were higher in the high CO_2 treatment (one-way ANOVA, $p = 0.0027$; Figure 2.1) but significantly lower in the combined high CO_2, low dissolved O_2 treatment compared to the control ($p < 0.0001$). Growth rates were not significantly different between the control and the low O_2 treatments. Growth rates calculated from changes in *in vivo* chlorophyll *a* over time were consistent with those based on cell counts (data not shown).

Daily measurements of dissolved O_2 concentrations and pH_T in the period following acclimation remained relatively constant over time in each treatment (Table 2.1; Table A.1 in the Appendix). Macronutrient concentrations were high enough to not be limiting during exponential growth (Table A.2 in the Appendix). At the final time point, nitrate and phosphate concentrations were all above 1.5×10^{-4} M and 3.2×10^{-5} M, respectively (data not shown).

Rates of dark respiration, gross photosynthesis, and net photosynthesis were calculated from linear regressions of oxygen production corresponding to respiration per cell ($R^2 > 0.6566$), gross photosynthesis per cell ($R^2 > 0.9471$), and net photosynthesis per cell, respectively ($R^2 > 0.9479$; e.g., Figure A.2 in the Appendix). Dark respiration rates were significantly lower in the combined high CO_2, low O_2 treatment relative to the control treatment (one-way ANOVA, $p = 0.0084$; Figure 2.2a). Respiration rates were not significantly

Table 2.1: Average treatment conditions in the long- (7-d) and short-term (6-h) *Amphidinium carterae* experiments (mean ± SEM), including number of individual bottles per treatment (N), irradiance (I), temperature (T), salinity (S), pH on the total scale (pH_T), total alkalinity (A_T), partial pressure of carbon dioxide (pCO_2), and dissolved oxygen concentration (O_2).

Treatment	N	I (µmol m^{-2} s^{-1})	T (°C)	S	pH_T	A_T (µmol kg^{-1})	pCO_2 (µatm)	O_2 (µmol L^{-1})
Long-term experiment (following acclimation)								
Control	4	104.4 ± 6.4	19.96 ± 0.02	32	8.04 ± 0.02	2030.9 ± 6.9	331.4 ± 10.9	239.7 ± 10.1
High CO_2	4	102.6 ± 9.4	19.94 ± 0.02	32	7.64 ± 0.01	2055.5 ± 9.3	1129.0 ± 36.3	251.8 ± 5.7
Low O_2	4	103.0 ± 11.0	19.98 ± 0.04	32	7.91 ± 0.01	1998.4 ± 6.2	512.3 ± 16.9	62.9 ± 5.8
High CO_2, low O_2	4	102.9 ± 7.9	20.00 ± 0.00	32	7.60 ± 0.02	2019.4 ± 5.1	1080.5 ± 44.1	59.7 ± 5.0
Short-term experiment examining metabolism								
Control	4	106.5 ± 6.8	19.90	32	7.93 ± <0.01	1993.1 ± 3.2	489.9 ± 6.6	254.6 ± 4.0
High CO_2	4	104.3 ± 8.3	19.95	32	7.63 ± <0.01	1993.1 ± 3.2	1056.7 ± 7.4	253.0 ± 2.5
Low O_2	4	102.5 ± 7.1	20.00	32	7.90 ± <0.01	1993.1 ± 3.2	519.9 ± 3.0	65.9 ± 0.7
High CO_2, low O_2	4	101.3 ± 6.3	20.05	32	7.60 ± <0.01	1993.1 ± 3.2	1111.1 ± 12.6	66.2 ± 0.8
Short-term experiment examining photophysiology								
Control	3	98.7 ± 1.8	20.00	32	7.92 ± 0.01	1993.1 ± 3.2	496.7 ± 13.3	247.0 ± 2.5
High CO_2, low O_2	3	95.0 ± 2.0	19.95	32	7.51 ± <0.01	1993.1 ± 3.2	1392.5 ± 11.3	52.8 ± 1.0

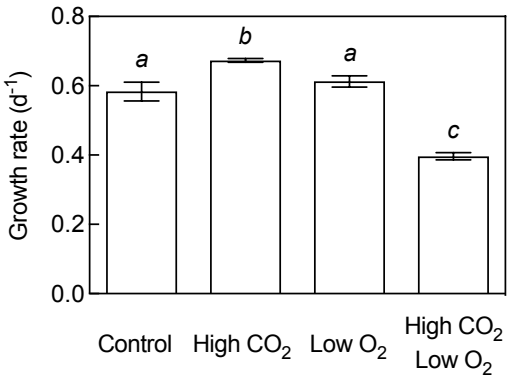

Figure 2.1: *Amphidinium carterae* growth rates during 7-d incubation (mean ± SEM; n = 4 for all treatments), calculated from exponential increases in cell counts over the last 3 d. Different letters indicate statistical significance compared to the other treatments (one-way ANOVA, $p < 0.05$).

different among the control, the high CO_2, and the low O_2 treatments. Rates of gross and net photosynthesis were lower in the low O_2 treatment ($p = 0.0157$ and $p = 0.0392$, respectively; Figure 2.2b and c, respectively) and were significantly lower in the combined high CO_2, low O_2 treatment relative to the control ($p < 0.0001$). Gross or net photosynthesis rates were not significantly different between the control and the high CO_2 treatments even though growth rates were significantly different. Relative differences in dark respiration, gross photosynthesis, and net photosynthesis rates calculated per unit RuBisCO were consistent with those calculated per cell (data not shown).

Relative to the control treatment, natural $\delta^{13}C$ values in harvested cells were significantly higher (less negative) in the low O_2 treatment (one-way ANOVA, $p = 0.0099$; Figure A.3a in the Appendix) and lower (more negative) in the high CO_2 treatment ($p < 0.0001$) and the combined high CO_2, low O_2 treatment ($p = 0.0174$). Natural $\delta^{15}N$ values were significantly higher in the combined high CO_2, low O_2 treatment relative to the control (one-way ANOVA, $p = 0.0046$; Figure A.3b in the Appendix). $\delta^{15}N$ values were not significantly different among the high CO_2, the low O_2, and the control treatments.

Over the course of the 3-h $^{13}C/^{15}N$ labeling incubation, $\delta^{13}C$ values significantly increased over time in each treatment as a result of ^{13}C uptake (paired t-test, $p < 0.0200$;

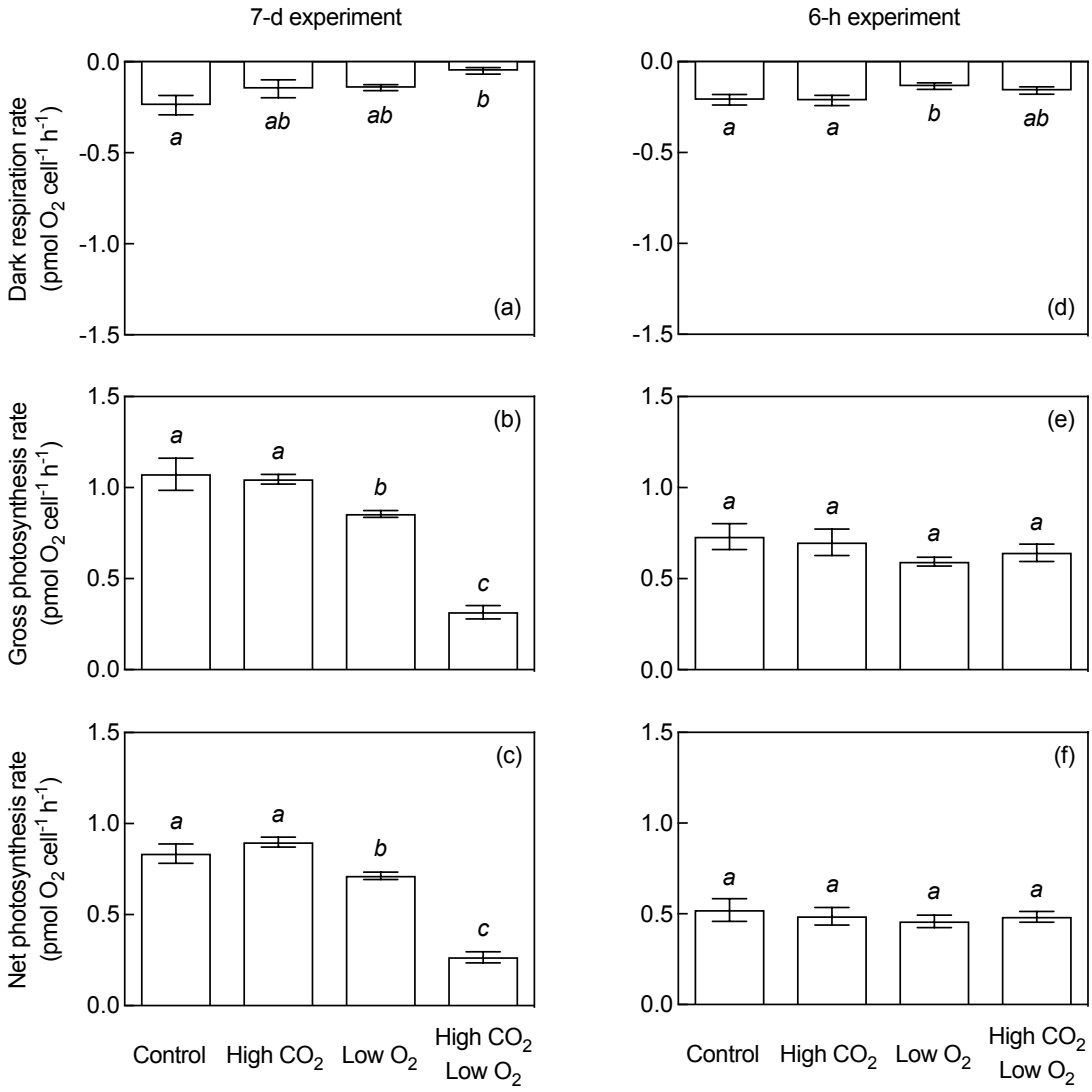

Figure 2.2: Rates of *Amphidinium carterae* dark respiration, gross photosynthesis, and net photosynthesis per cell (a, b, c) after 7-d (mean ± SEM; n = 4 for all treatments) and (d, e, f) 6-h incubations (n = 3 for all treatments), calculated from changes in O_2 evolution over 5 h. Different letters indicate statistical significance compared to the other treatments (one-way ANOVA, $p < 0.05$).

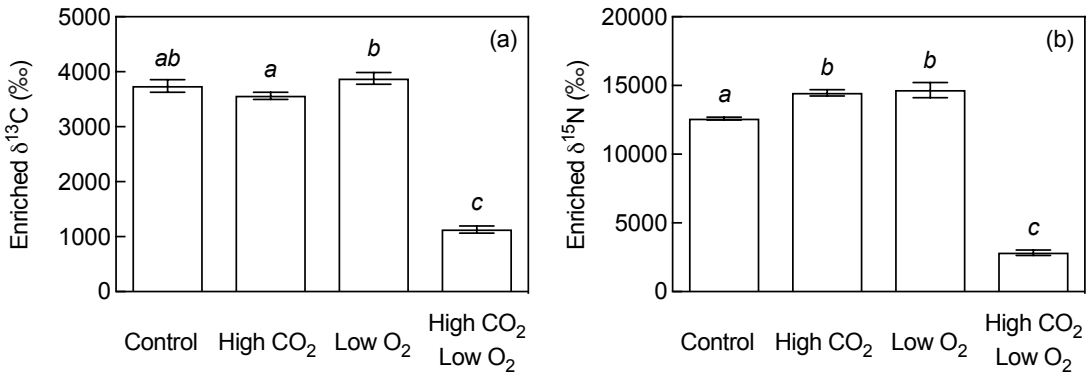

Figure 2.3: Enriched (a) δ^{13}C signatures and (b) δ^{15}N signatures of *Amphidinium carterae* cells at the end of the 7-d experiment after an additional 3-h ^{13}C- and ^{15}N-labeling incubation (mean ± SEM; n = 4 for all treatments). Different letters indicate statistical significance compared to the other treatments (one-way ANOVA, $p < 0.05$).

Figure 2.3a). Similarly, δ^{15}N values significantly increased in each treatment due to ^{15}N uptake ($p < 0.0088$; Figure 2.3b). These trends indicate substantial uptake of both labels. Note that the δ^{13}C and δ^{15}N measurements represent relative values and must be compared among treatments in this experiment. Enriched δ^{13}C values in harvested cells were significantly lower in the combined high CO_2, low O_2 treatment relative to the control treatment (one-way ANOVA, $p < 0.0001$; Figure 2.3a). Labeled δ^{13}C signatures were not significantly different between the control and the high CO_2 treatment or the low O_2 treatment. Enriched δ^{15}N signatures were significantly higher relative to the control in the high CO_2 treatment ($p = 0.0014$; Figure 2.3b) and the low O_2 treatment ($p = 0.0006$) but significantly lower in the combined high CO_2, low O_2 treatment relative to the control ($p < 0.0001$).

Total protein content per cell was significantly lower in all treatments compared to the control (one-way ANOVA, $p < 0.0130$; data not shown) but was not significantly different among the high CO_2, the low O_2, and the combined high CO_2, low O_2 treatments. Relative to the control treatment, RuBisCO content as a percentage of total protein was significantly higher in the combined high CO_2, low O_2 treatment (one-way ANOVA, $p = 0.0207$; Figure

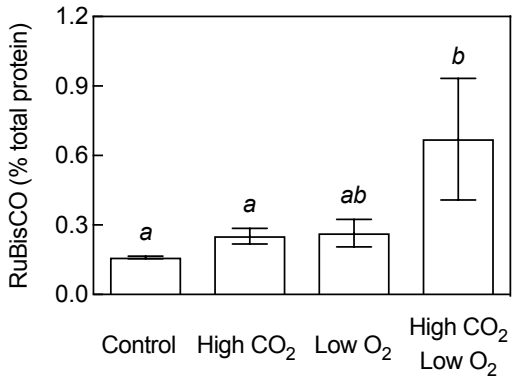

Figure 2.4: RuBisCO content in *Amphidinium carterae* cells after 7-d incubation (mean ± SEM; n = 4 for all treatments). Different letters indicate statistical significance compared to the other treatments (one-way ANOVA, $p < 0.05$).

2.4). Differences in RuBisCO per cell were consistent with differences in percent RuBisCO content (data not shown). Compared to the control treatment, extracted chlorophyll *a* per cell was higher in the high CO_2 treatment (one-way ANOVA, $p = 0.0430$; data not shown), the low O_2 treatment ($p < 0.0001$), and the combined high CO_2, low O_2 treatment ($p = 0.0125$) at the end of the 7-d incubation.

Potential quantum yield was significantly lower in the low O_2 treatment (one-way ANOVA, $p = 0.0001$; Figure 2.5a), the high CO_2 treatment ($p = 0.0310$), and the combined low O_2 and high CO_2 treatment relative to the control ($p < 0.0001$).

2.4.2 Short-term impacts on metabolism

Cell counts and *in vivo* chlorophyll *a* measurements at the beginning of the short-term incubation were within the range of values measured the end of the long-term experiment (data not shown). Dissolved O_2 and pH_T concentrations were comparable to those in the long-term experiment (Table 2.1).

Rates of respiration and gross and net photosynthesis following short-term incubation were determined from linear regressions of respiration per cell ($R^2 > 0.9290$), gross photosynthesis per cell ($R^2 > 0.9588$), and net photosynthesis per cell, respectively ($R^2 > 0.9458$).

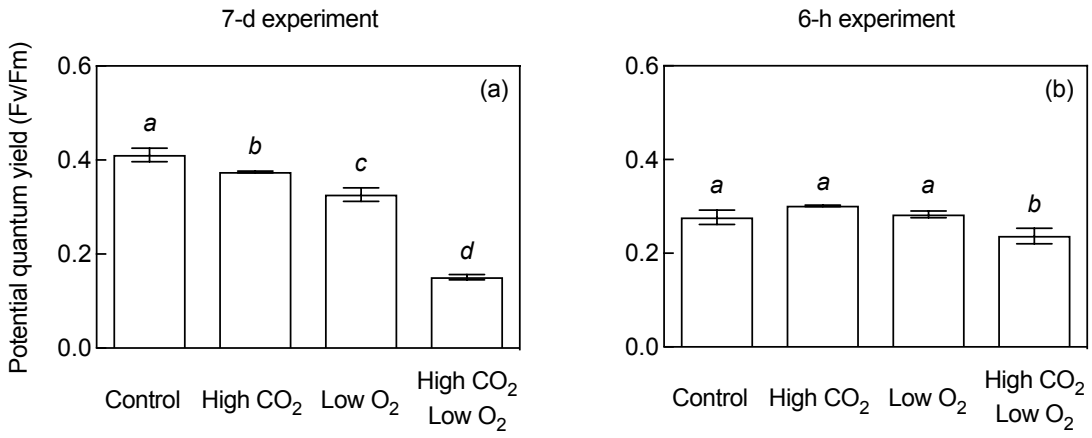

Figure 2.5: Potential quantum yield of photosystem II (Fv/Fm) in *Amphidinium carterae* cells (a) after 7-d (mean ± SEM; n = 4 for all treatments) and (b) after 6-h incubations (n = 4 for all treatments). Different letters indicate statistical significance compared to the other treatments (one-way ANOVA, $p < 0.05$).

Dark respiration rates were significantly lower in the low O_2 treatment compared to the control treatment (one-way ANOVA, $p = 0.0489$; Figure 2.2d). Respiration rates were not significantly different among the control, the high CO_2, and the combined high CO_2, low O_2 treatments. Rates of gross and net photosynthesis rates were not significantly different among all treatments (Figure 2.2e and f, respectively).

Potential quantum yield was not initially different between the control treatment and each of the other treatments (one-way ANOVA; data not shown). After 6-h incubation under the treatment conditions, potential quantum yield in the combined high CO_2, low O_2 treatment was significantly lower than the control (one-way ANOVA, $p = 0.0362$; Figure 2.5b). Yield was not significantly different among the control, the high CO_2, and the low O_2 treatments.

2.4.3 Short-term impacts on photophysiology

Cell counts and *in vivo* chlorophyll *a* measurements were higher than those measured at the end of the long-term experiment in order to improve signal strength on the PAM

(data not shown). Dissolved O_2 concentrations and pH_T values were similar to those from the other experiments (Table 2.1).

Relative differences in initial and final potential quantum yield measurements were consistent with the findings from the previous short-term experiment (data not shown). Photophysiology measurements were obtained after 6-h incubation under the treatment conditions using the Xe-PAM. Under increasing actinic light intensities (Figure 2.6a), effective quantum yield was not significantly different between the control and the combined high CO_2, low O_2 treatments (Figure 2.6b). Similarly, relative ETR during actinic irradiation was not significantly different between the two treatments (Figure A.4 in the Appendix). However, during dark recovery in the 0.667 to 3.667 min following actinic illumination, effective quantum yield in the combined high CO_2, low O_2 treatment was significantly lower than the control treatment (paired t-test, $p < 0.0135$; Figure 2.6b). Additionally, 3.667 min following actinic illumination during dark recovery, qP was significantly lower in the combined high CO_2, low O_2 treatment relative to the control (paired t-test, $p = 0.0454$; Figure A.5a in the Appendix). NPQ was slightly higher in the combined high CO_2, low O_2 treatment than the control during recovery, but the trend was not significant (Figure A.5b in the Appendix).

2.5 Discussion

2.5.1 Overview

Contrary to expectations, the combination of low O_2 and high CO_2 conditions decreased growth rates of the harmful dinoflagellate *Amphidinium carterae*. Synergistic effects were much larger than the effect of CO_2 alone, O_2 alone, or any additive effect. Cells exhibited physiological indicators of stress under combined high CO_2, low O_2 conditions including increased allocation of RuBisCO and decreased Fv/Fm. *A. carterae* response times were rapid, with changes in physiology apparent within hours. These findings are consistent with photosynthetic imbalances in *A. carterae* cells under combined acidification and hypoxia conditions.

This is the first investigation of the synergistic effects of CO_2 and O_2 on the growth, metabolism, and photophysiology of a phytoplankton species from the perspective of simu-

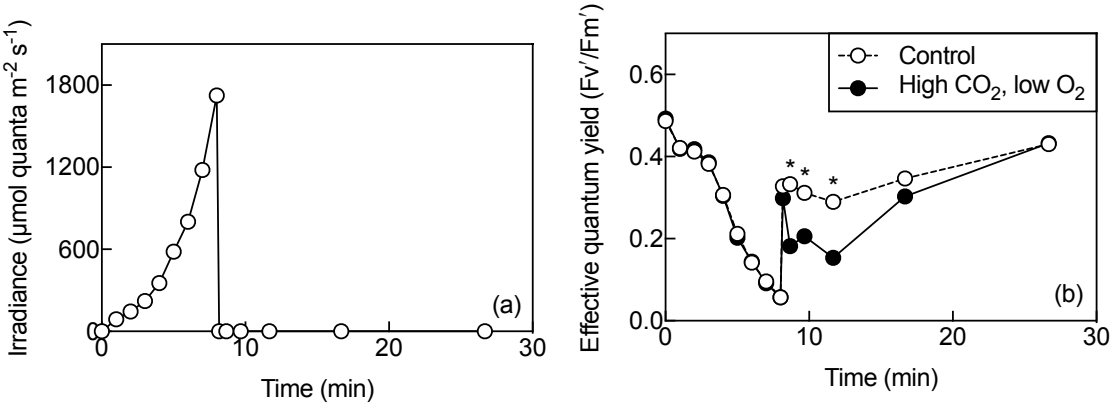

Figure 2.6: Results of the induction-recovery curves following 6-h incubation including (a) actinic light exposure levels and (b) the resulting effective quantum yield of photosystem II of *Amphidinium carterae* cells (mean ± SEM; n = 3 for both treatments). The asterisk indicates statistical significance between the treatments at a particular time point (paired t-test, $p < 0.05$).

lating hypoxia and ocean and coastal acidification. Other studies have examined the effects of varying CO_2 and O_2 concentrations on freshwater and marine phytoplankton (e.g., Bagby and Chisholm, 2015; Bunt, 1971; Pope, 1975), as well as on symbiotic algae (e.g., Badger et al., 1998; Kitaya et al., 2008). Studies measuring phytoplankton photorespiration have also manipulated CO_2 and O_2 concentrations together (e.g., Birmingham et al., 1982; Peltier and Thibault, 1983). In addition, many laboratory studies investigating the effects of hypoxia have inadvertently manipulated CO_2 and O_2 conditions together by bubbling with nitrogen gas (Gobler et al., 2014). However, this is the first study to use factorial experiments to examine these stressors in combination with the express purpose of comparing ocean acidification, coastal hypoxia, and coastal acidification.

2.5.2 Growth responses

Results of both the long- and short-term incubation experiments do not support the initial hypothesis that high CO_2, low O_2 conditions would particularly benefit *A. carterae*. To the contrary, combined high CO_2, low O_2 conditions had synergistically negative effects

on *A. carterae* growth (Figure 2.1). This effect was not the result of CO_2 (pH) conditions alone since elevated CO_2 actually stimulated *A. carterae* growth (Figure 2.1). The growth response at combined high CO_2, low O_2 was also not caused solely by low O_2 conditions since O_2 alone did not significantly affect growth rates (Figure 2.1). Low growth rates were also not caused by changes in temperature, irradiance, pH, pCO_2, O_2, or macronutrient concentrations within each treatment over the course of the grow-out (Table A.1, Table A.2 in the Appendix). There were no significant changes in stoichiometric nutrient ratios in the *A. carterae* culture media (Table A.2 in the Appendix).

The increase in *A. carterae* growth under high CO_2 is consistent with some previous studies, which have suggested that *A. carterae* growth may be stimulated under elevated CO_2 concentrations due to the lack of external CA (Dason et al., 2004; Fu et al., 2012), despite some evidence of a CCM (Burns and Beardall, 1987). It is important to note that among phytoplankton, the effects of CO_2 are highly species-specific even within the same taxonomic group (e.g., Liu et al., 2017; Sobrino et al., 2008; Young et al., 2015a). Among dinoflagellates, some species including *Alexandrium fundyense* have been shown to increase growth rates under high CO_2 (Hattenrath-Lehmann et al., 2015), while others including *Prorocentrum minimum* either decrease their growth rates (Hennon et al., 2017) or remain unaffected by CO_2 (Fu et al., 2008).

The finding that O_2 did not affect *A. carterae* growth rates is novel in that, to the best of our knowledge, the impacts of hypoxia on the growth rates of dinoflagellates have yet to be described in the literature. However, hypoxia has been shown to decrease growth rates of the diatom *Skeletonema costatum* (Wu et al., 2012). Hyperoxia (characterized by high O_2) has also been shown to decrease growth rates of sea ice microalgae presumably due to production of active oxygen radicals (McMinn et al., 2005).

The significant decrease in *A. carterae* growth rates under combined high CO_2, low O_2 conditions is surprising, given that these conditions should maximize carbon fixation and minimize oxygen fixation (Foyer and Noctor, 2000; Tortell, 2000), particularly in an organism with such a low RuBisCO substrate specificity (Whitney and Andrews, 1998). Previous work has also indicated enhanced growth of some phytoplankton species under high CO_2 and low O_2 conditions. Growth rates of the cyanobacterium *Anacystis nidulans*

and the diatom *Phaeodactylum tricornutum* under various CO_2 and O_2 conditions have been shown to generally increase at low O_2 and high CO_2 (Pope, 1975). Growth of the symbiotic dinoflagellate *Amphidinium* sp. separated from the flatworm *Amphiscolops* sp. (cultured without prior acclimation) has been shown to slightly – albeit not significantly – increase with increasing CO_2 conditions from 20 ppmv to 1000 ppmv (Kitaya et al., 2008). Under a range of CO_2, growth rates have also been shown to slightly increase with increasing O_2 concentration from 0.3% to 5% and slightly decrease with increasing O_2 from 5% to 21% (Kitaya et al., 2008). However, growth rates of the cyanobacterium *Prochlorococcus* have been shown to significantly decrease with decreasing O_2 from 21% to $< 0.001\%$ under a range of CO_2, which suggests that O_2 may serve a photoprotective role via the process of photorespiration (Bagby and Chisholm, 2015).

2.5.3 Possible role of photorespiration

We find the possibility that photorespiration may be beneficial for *A. carterae* to be especially intriguing. Photorespiration has been shown to decrease significantly under high CO_2, low O_2 conditions in the green alga *Chlamydomonas reinhardtii* (Peltier and Thibault, 1983) and in a number of freshwater algae (Birmingham et al., 1982). In addition, decreases in photorespiratory gene expression have been shown to correspond to decreases in productivity of the symbiotic dinoflagellate *Symbiodinium* sp. (Crawley et al., 2010). It has also been demonstrated that photorespiratory conditions can prevent damage to PSII reaction centers under high light conditions (Foyer and Noctor, 2000), while nonphotorespiratory conditions can compromise photosynthesis (Bauwe et al., 2012). In this study, maximal photorespiratory conditions occurred in the control treatment (when the CO_2:O_2 ratio was low), while nonphotorespiratory conditions occurred in the high CO_2, low O_2 treatment (as discussed by Foyer and Noctor, 2000). It is possible that high rates of photorespiration protected the *A. carterae* cells by dissipating excess energy and reducing equivalents (e.g., NADPH) and balancing the redox poise of the electron transport chain (Bagby and Chisholm, 2015), even though the experiments were not performed under high light conditions. Therefore, the nonphotorespiratory conditions at high CO_2, low O_2 may have caused a photosynthetic impedance mismatch – defined as resistance in dissipating excess light

energy – even under moderate light conditions (as demonstrated by Bagby and Chisholm, 2015) and may have contributed to *A. carterae* growth inhibition.

However, it is important to note that we did not measure alternative mechanisms for O_2 uptake. The Mehler reaction – involving the reduction of O_2 to form reactive oxygen species – has been shown to be photoprotective in the symbiotic dinoflagellate *Symbiodinium* sp. (Roberty et al., 2014). Like photorespiration, this reaction is inhibited under low O_2 conditions (Roberty et al., 2014) and therefore may play a role in the observed *A. carterae* growth responses. CO_2 and O_2 conditions also affect RuBisCO activase, the protein that causes RuBisCO to release ribulose-1,5-bisphosphate (RuBP) and allows binding of CO_2 at the active site of RuBisCO (Jensen, 2000). RuBisCO activase activity has been shown to be inhibited under high CO_2, low O_2 conditions (Crafts-Brandner and Salvucci, 2000) and it is possible that this decrease in activity contributed to the synergistic, negative effects on *A. carterae*. In addition, it is possible that other unmeasured factors (e.g., chlororespiration, cyclic electron flow) may have contributed to the biological response observed in this study.

2.5.4 Metabolic responses

Combined high CO_2, low O_2 conditions also had negative effects on *A. carterae* metabolism (Figure 2.2). During the long-term experiment, these conditions significantly decreased rates of dark respiration (Figure 2.2a), although these responses were not synergistic. In addition, rates of gross and net photosynthesis decreased under low O_2 conditions, but the effects became synergistically negative in combination with high CO_2 conditions (Figure 2.2b and c). During the short-term incubation, combined high CO_2, low O_2 conditions did not significantly affect respiration or photosynthesis rates (Figure 2.2d, e, and f). However, short-term respiration rates were negatively impacted at low O_2 (Figure 2.2d). Therefore, the synergistic effects of CO_2 and O_2 on *A. carterae* metabolism were not immediate and rather developed over time.

The finding that high CO_2, low O_2 conditions significantly decreased respiration rates is consistent with some previous work. Low O_2 has been shown to decrease respiration rates among some macroalgae including *Gracilaria tikvahiae*, but not *Cladophora vagabunda* (Peckol and Rivers, 1995). Additionally, low O_2 conditions have been shown to decrease

community respiration on a reef flat (Gruber et al., 2017). Among some land plants, respiration has also been shown to decrease under high CO_2 conditions (Azcón-Bieto et al., 1994; Gonzàlez-Meler et al., 1996; Tcherkez et al., 2008). This may be driven in part by the decrease in photorespiration (Tcherkez et al., 2008) or the inhibition of mitochondrial enzymes including cytochrome *c* oxidase and succinate dehydrogenase (Gonzàlez-Meler et al., 1996). Among dinoflagellates, responses in respiration rates to ocean acidification conditions are variable. Respiration has been shown to increase in *Alexandrium tamarense* (Eberlein et al., 2014) and *Symbiodinium* sp. (Crawley et al., 2010); however, respiration does not seem to be affected in *Scrippsiella trochoidea* (Eberlein et al., 2014).

The significant decrease in photosynthesis rates following long-term incubation under high CO_2, low O_2 conditions is internally consistent with the decrease in *A. carterae* growth rates. Similar findings have also been discussed in several previous studies. For some species of marine phytoplankton, low O_2 concentrations have been shown to decrease carbon fixation rates (Bagby and Chisholm, 2015; Bunt, 1971). However, different species of phytoplankton have been shown to exhibit significantly different carbon fixation rates under a range of dissolved CO_2 and O_2 conditions (Bunt, 1971; Pope, 1975). The finding that photosynthesis rates were not affected following short-term incubation is also in line with previous research. Photosynthesis of the diatom *Thalassiosira weissflogii* has been shown to remain unaffected under a range of CO_2 conditions following 6-h incubation (Goldman et al., 2017).

2.5.5 Carbon and nitrogen uptake

Synergistic, negative effects were also observed for both enriched isotopic $\delta^{13}C$ and $\delta^{15}N$ signatures following the 3-h labeling incubation under high CO_2, low O_2 conditions (Figure 2.3). The significant decreases in enriched $\delta^{13}C$ and $\delta^{15}N$ following labeling at high CO_2, low O_2 are consistent with the low growth and photosynthesis rates observed under these treatment conditions. Decreased $\delta^{13}C$ signatures under high CO_2 conditions are consistent with some previous studies. In plant leaves, the carbon isotope composition of respired CO_2 has been shown to slightly decrease with increasing CO_2 (Tcherkez et al., 2012). Among marine phytoplankton including the diatom *Phaeodactylum tricornutum*, $\delta^{13}C$ values have

also been shown to decrease under increasing CO_2 (decreasing pH) conditions (Biswas et al., 2015; Laws et al., 1997). It has been suggested that among dinoflagellates, carbon isotope fractionation may be driven by inorganic carbon fluxes (Hoins et al., 2016).

2.5.6 RuBisCO content

Surprisingly, combined high CO_2, low O_2 conditions significantly increased *A. carterae* RuBisCO content despite decreased growth rates (Figure 2.4), although this response was not synergistic. It is possible that *A. carterae* cells increased RuBisCO to compensate for reduced growth efficiency or possibly decreased RuBisCO activase activity. This finding is consistent with several previous studies on diatoms, which have been shown to increase RuBisCO allocation under stress conditions including low nitrogen (Li and Campbell, 2017) and low temperature (Losh et al., 2013; Young et al., 2015b). In addition, psychrophilic isolates of the green alga *Chloromonas* sp. have been shown to increase RuBisCO, presumably to offset low RuBisCO efficiency under low temperature (Devos et al., 1998). The RuBisCO percentages measured in this study ($< 1\%$ total protein) are within the range of values measured in some natural phytoplankton populations (Losh et al., 2013).

2.5.7 Fv/Fm responses

High CO_2, low O_2 conditions also caused synergistically negative effects on *A. carterae* physiology (Figure 2.5). Following the 7-d incubation, Fv/Fm significantly decreased in the high CO_2, low O_2 treatment, and to a lesser extent, in the high CO_2 treatment and low O_2 treatment (Figure 2.5a). Although photosynthesis was not yet affected after the 6-h incubation, Fv/Fm significantly decreased at high CO_2, low O_2 (Figure 2.5b). The decreases in Fv/Fm were largely driven by decreases in Fm, indicating a greater number of closed PSII reaction centers (Ulstrup et al., 2005).

The finding that both high CO_2 and low O_2 significantly decreased Fv/Fm is consistent with numerous previous studies. In plant leaves, nonphotorespiratory (i.e., low O_2) conditions have been shown to decrease Fv/Fm as a result of photodamage (Peñuelas and Llusià, 2002). In the green alga *Scenedesmus obliquus*, low O_2 conditions have been shown to disrupt electron flow from PSII (Schreiber and Vidaver, 1974). Similarly, in the sym-

biotic dinoflagellate *Symbiodinium* sp., low O_2 conditions have been shown to reduce the electron transport chain, close PSII reaction centers, decrease Fm, and ultimately decrease Fv/Fm (Ulstrup et al., 2005). *A. carterae* has been shown to decrease Fv/Fm under nutrient deficient conditions (Li et al., 2016), but the impacts of CO_2 and O_2 concentrations on *A. carterae* physiology have yet to be reported.

2.5.8 Induction-recovery responses

Photophysiology of *A. carterae* was also affected following 6-h incubation, as demonstrated in the light curves with dark recovery (Figure 2.6). During the period of recovery following actinic irradiation, Fv'/Fm' decreased significantly under high CO_2, low O_2 conditions (Figure 2.6b), as did qP (Figure A.5a in the Appendix). These findings indicate delayed recovery of PSII reaction centers following photoinhibition and potentially suppressed repair of PSII (Takahashi et al., 2007) under high CO_2 and low O_2 conditions. In addition, these photophysiology responses of *A. carterae* were observed rapidly after only 6-h incubation, unlike metabolic responses, which took more time to develop.

These short-term results are consistent with the idea that photorespiration may serve a photoprotective role even under moderate light (e.g., Bagby and Chisholm, 2015). In land plants, high photorespiratory conditions have been shown to improve tolerance to light stress (Takahashi et al., 2007). In the cyanobacterium *Synechocystis* sp., photorespiration has been shown to protect cells from photoinhibition (Hackenberg et al., 2009).

Alternatively, the results of the short-term experiment may be explained by state transitions – the migrations of the light-harvesting system between PSII and PSI to balance absorbed light energy (Lemeille and Rochaix, 2010). State transitions have been shown to alter pathways of electron flow to regulate cellular ATP levels under changing light conditions (Lemeille and Rochaix, 2010). Under anoxic conditions, state transitions rely on hydrogenase activity for induction of electron transport between PSII and PSI (Schreiber and Vidaver, 1974). In *Chlamydomonas reinhardtii* mutants lacking hydrogenase activity, delays in state transitions have been shown to occur under low O_2 conditions, consistent with the timescale of recovery in our short-term experiments (i.e., several minutes; Godaux et al., 2015). It is possible that hydrogenase activity decreased in *A. carterae* cells under

high CO_2, low O_2 conditions, thereby inducing a lag in PSII activity. However, it is important to note that to our knowledge, there is no evidence that dinoflagellates undergo state transitions.

Therefore, the photosynthetic imbalances in *A. carterae* cells under high CO_2, low O_2 conditions are consistent with (1) a photosynthetic impedance mismatch under nonphotorespiratory conditions driven by an imbalance between light excitation energy and carbon fixation (Bagby and Chisholm, 2015) and/or (2) decreased hydrogenase activity (Godaux et al., 2015). We propose that the first explanation may be more plausible, since there is no evidence to show that *A. carterae* cells undergo state transitions.

2.5.9 Conclusions

Additional experiments are required to better understand the photoprotective role of photorespiration on the growth of phytoplankton under a range of CO_2:O_2 ratios. In particular, other phytoplankton species need to be examined since *in vivo* organismal responses to the interactive effects of multiple stressors are likely species- and even strain-dependent (Fu et al., 2012). Additionally, the extent of oxidative damage to phytoplankton cells under low photorespiratory conditions needs to be assessed under a wide range of light, temperature, CO_2, and O_2 concentrations. Such studies would further assess the previously unrecognized role of photorespiration in phytoplankton metabolism.

The experimental results of this study demonstrate a strong synergistic interaction between CO_2 and O_2 in a toxic dinoflagellate. Since interactive effects of ocean acidification with other environmental drivers are often surprising (e.g., Bausch et al., 2017), we caution that predicting synergies among phytoplankton species will be difficult – if not impossible – without performing empirical studies. We also suggest that combined coastal acidification and hypoxia may have negative, synergistic impacts on the growth, metabolism, and physiology of some phytoplankton in coastal ecosystems over the course of this century, as shown in the case of *A. carterae*. These findings are consistent with the idea that photorespiratory conditions may be especially beneficial to *A. carterae*. Specifically, photorespiration may be an important, photoprotective strategy to maintain the balance between the light-dependent and -independent reactions of photosynthesis. These results may help improve

understanding of the effects of multi-stressors on an organismal level in coastal ecosystems, as well as the broader impacts of future anthropogenic climate change on the base of the food web in zones of both acidification and hypoxia.

2.6 Acknowledgements

The authors would like to thank Sonya Dyhrman and Sheean Haley at Lamont-Doherty Earth Observatory (LDEO) for providing laboratory space and logistical support; Hugh Ducklow, Robert Anderson, Kevin Griffin, and Gwenn Hennon at LDEO for providing feedback on the manuscript; Wei Huang at LDEO for performing the isotopic analyses; Jerry Frank at the Chesapeake Biological Laboratory for performing the nutrient analyses; Andrew Dickson at Scripps Institution of Oceanography for providing the CO_2 seawater reference materials; and Naomi Shelton and Clara Chang for providing laboratory assistance. This work was partly supported by NASA Headquarters under the NASA Earth and Space Science Fellowship Program grant 15-EARTH15R-5. Funding was also provided by the Natural Sciences and Engineering Research Council of Canada and the Chevron Student Initiative Fund in the Department of Earth and Environmental Sciences at Columbia University.

Chapter 3

Toxic effects of sediments on the harmful dinoflagellate *Cochlodinium polykrikoides* under ocean acidification conditions

Note: A modified version of this chapter was originally published as Bausch, A. R., Boatta, F., Morton, P. L., McKee, K. T., Anderson, R. F., Gomes, H. R., and J. I. Goes (2017). Elevated toxic effect of sediments on growth of the harmful dinoflagellate *Cochlodinium polykrikoides* under high CO_2. *Aquatic Microbial Ecology* 80(2):139–152. DOI: 10.3354/ame01848.

3.1 Abstract

Ocean acidification will likely have significant impacts on phytoplankton growth in marine ecosystems over the course of this century. Coastal waters, which can be strongly influenced by suspended sediments, can also be particularly sensitive to ocean acidification. While the individual effects of trace metal inputs and ocean acidification have each been well documented, the combined effects of high trace metal concentrations due to mobilization from sediments and high dissolved carbon dioxide (CO_2) concentrations (low seawater pH) on the growth of marine phytoplankton are not known. In this study, a batch culture experiment was performed using the model organism *Cochlodinium polykrikoides* over 35 days under a range of CO_2 (400, 800, and 1200 ppmv) following sediment additions. At

high CO_2, dissolved iron (Fe) and nickel (Ni) concentrations increased over time. Dissolved Ni concentrations were significantly higher after 35 days at 1200 ppmv CO_2 compared to the other treatments and corresponded to significant decreases in *C. polykrikoides* growth rates. In addition, a toxicity bioassay experiment was performed over 29 days under a range of Ni or Cd concentrations at ambient CO_2. The growth responses of *C. polykrikoides* were dose-dependent and were significantly lower under increasing Ni or Cd concentrations. The findings suggest that a combination of elevated total dissolved Ni supplied from sediments and high CO_2 conditions could suppress the growth rates and photosynthesis of *C. polykrikoides* in coastal marine ecosystems. This is the first study to examine the synergistic, toxic effects of lithogenic trace metals and CO_2 on phytoplankton growth.

3.2 Introduction

Increasing atmospheric carbon dioxide (CO_2) concentrations are expected to strongly impact both marine organisms and ecosystem processes via ocean acidification (Doney et al., 2009). By 2100, global atmospheric CO_2 concentrations are projected to reach up to 1150 ppmv (IPCC, 2013), causing sea surface pH to decrease by 0.3-0.5 units (Caldeira and Wickett, 2005). Although the biological responses to decreased seawater pH are complex, variable, and species-specific, ocean acidification will likely have profound effects on many marine calcifying organisms, some noncalcifying phytoplankton, and more generally, marine food webs and ecosystems (Connell and Russell, 2010; Doney et al., 2009; Guinotte and Fabry, 2008).

Some coastal waters may be particularly susceptible to ocean acidification over the course of this century, especially in regions with high riverine inputs or strong mixing (Strong et al., 2014). Such systems can have high concentrations of total suspended solids due to inputs of lithogenic particles in freshwater or resuspension of bottom sediments (Geyer et al., 2004). The Hudson River estuary (New York, USA), the Eel River shelf (California, USA), and the Amazon shelf (Brazil) can all experience suspended sediment concentrations in excess of 1000 mg L^{-1} (Geyer et al., 2004). On a global scale, changes in

climate and land use may increase riverine sediment inputs to coastal marine ecosystems by the end of this century (Ito, 2007; Yang et al., 2003).

Coastal areas of the Persian Gulf may be vulnerable to the interactive effects of ocean acidification and lithogenic particle loads. The Persian Gulf marine ecosystem is predicted to have one of the highest cumulative anthropogenic impacts by the end of this century (Halpern et al., 2008). Additionally, coastal waters in the region are strongly influenced by high concentrations of suspended sediments ranging from 125 to 2295 mg L^{-1} from the Shatt al-Arab River (Al Yamani, 2008; Gaillardet et al., 1999) and, to a lesser extent, atmospherically forced mineral dust from the Arabian Peninsula (Mackey et al., 2010; Tindale and Pease, 1999). Over the course of this century, high concentrations of both atmospheric CO_2 and suspended lithogenic particles will likely impact marine organisms within the ecosystem.

Lithogenic particles play an important role in carbon cycling, storage, and climate (Jickells et al., 2005; Mahowald et al., 2010; Turner and Millward, 2002). Sediments and dust contain iron (Fe; Duce and Tindale, 1991; Martin, 1990), as well as other bioactive trace metals such as nickel (Ni) and cadmium (Cd; Mackey et al., 2012; Modaihsh, 1997; Sunda et al., 2005). The bioactive trace metals mobilized from lithogenic particles can stimulate phytoplankton growth at relatively low concentrations (Ho et al., 2013; Morel and Price, 2003; Twining and Baines, 2013). In addition, lithogenic particles (Moore et al., 2009; Srinivas and Sarin, 2013) and trace metals such as Ni (Ho, 2013) have been shown to stimulate oceanic nitrogen fixation. However, some trace metals supplied by mineral particles can also be toxic at high concentrations (Jordi et al., 2012; Paytan et al., 2009). Trace elements such as Cd, copper (Cu), and lead (Pb) have been shown to negatively affect the growth of marine phytoplankton (Brand et al., 1986; Echeveste et al., 2012; Herzi et al., 2013). Sub-lethal toxic effects of Cu and Pb have been described for the harmful dinoflagellate *Cochlodinium polykrikoides* (Ebenezer and Ki, 2012). Despite varying sensitivities and growth responses to trace metals among phytoplankton species (Sunda, 1989), potential future changes in lithogenic particle inputs could significantly impact marine biogeochemical dynamics (Mahowald et al., 2010).

While many studies have examined the individual effects of CO_2 or trace metals on phytoplankton physiology (e.g., Doney et al., 2009; Morel and Price, 2003), few studies have explored the combined interactions of ocean acidification and trace metal chemistry on phytoplankton growth (Millero et al., 2009). Ocean acidification can impact the biogeochemistry of lithogenic trace metals by altering their solubility and speciation, including their capacity to form complexes with organic ligands (Eggleton and Thomas, 2004; Hoffmann et al., 2012; Millero et al., 2009). Decreased seawater pH has been shown to alter the chemical speciation of Fe, leading to significant impacts on the uptake rates of Fe by phytoplankton (Shi et al., 2010). Both seawater pH and complexing agents have been shown to impact the bioavailability and uptake rates of zinc (Zn) and Cd (Xu et al., 2012). In high-nutrient, low-chlorophyll (HNLC) waters of the North Pacific, ocean acidification has been shown to influence Fe uptake from desert dust deposition (Mélançon et al., 2015). However, no studies have examined the potential toxic effects of lithogenic trace metals on the growth of phytoplankton (e.g., *C. polykrikoides*) under varying ocean acidification scenarios. This is a critical area of research that requires attention (Hoffmann et al., 2012).

In the present study, the dinoflagellate *C. polykrikoides* was used as a model organism to assess the interactive effects of increasing atmospheric CO_2 and trace metal release from sediments on the growth of a harmful algal bloom (HAB) species. *C. polykrikoides* blooms have been observed in the Persian Gulf and Sea of Oman (Al Azri et al., 2014; Richlen et al., 2010) and have been associated with mass mortalities of fish and shellfish in the region (Al Gheilani et al., 2011; Saeedi et al., 2011). Here, sediments collected from Oman were added to batch cultures to assess the toxicity of lithogenic trace metals under three different CO_2 conditions: 400 ppmv (current atmospheric levels), 800 ppmv (projected "business-as-usual scenario" levels in 2100), and 1200 ppmv (projected "worst-case scenario" levels in 2100; IPCC, 2013). The concentrations of bioactive trace metals released from the sediments and the growth responses of the model organism *C. polykrikoides* were examined over 35 days. In addition, a toxicity bioassay experiment was performed to assess *C. polykrikoides* growth responses under a range of concentrations of Cd or Ni (two potentially toxic lithogenic trace metals) at ambient CO_2 over 29 days.

The research objectives of this assessment were threefold: (1) to assess the changes in trace metal concentrations released from sediments under high CO_2; (2) to examine the physiological responses of *C. polykrikoides* to high suspended sediment loads under elevated CO_2; and (3) to determine the toxicity responses of *C. polykrikoides* to Cd and Ni. Based on previous studies (e.g., Millero et al., 2009), the release of trace metals from sediment was predicted to increase under increasing CO_2 (Hypothesis 1). In addition, based on other recent studies (e.g., Paytan et al., 2009), increased concentrations of dissolved lithogenic trace metals were predicted to negatively affect the growth of *C. polykrikoides* (Hypothesis 2). This is the first study to examine the synergistic, toxic effects of sediment on the growth of a HAB species under high CO_2. It is also the first study to examine the toxicity responses of *C. polykrikoides* to Ni and Cd. Such information is essential to improve understanding of the changing biogeochemical dynamics associated with anthropogenic ocean acidification in marine ecosystems.

3.3 Materials and methods

3.3.1 Algal culture and media

Culture isolates of *Cochlodinium polykrikoides* (strain CP1) came from Flanders Bay in Long Island, New York, USA (Gobler et al., 2008; Tang and Gobler, 2009). This culture strain (the "American/Malaysian" ribotype) was the same strain identified in the Persian Gulf and Sea of Oman in 2008-2009 based on ribosomal RNA (Iwataki et al., 2008; Richlen et al., 2010). Cultures were maintained at a constant temperature of 24.7 ± 0.04°C (mean ± SEM) in an incubator fitted with a bank of 34-W cool white lights with a light intensity of ~100 μmol quanta m^{-2} s^{-1} and with a photoperiod of 11.5 hours light: 12.5 hours dark.

Seawater was collected from Corson's Inlet in Dennisville, New Jersey, USA (salinity = 34), 0.2 μm capsule-filtered, and autoclave-sterilized. Three types of modified L1 media (Guillard and Hargraves, 1993) were prepared using coastal seawater as the base: (1) media with no added trace metals, ethylenediaminetetraacetic acid (EDTA), or silicate, used for the CO_2/sediment incubation experiment (in all treatments including the reference cultures); (2) media with no added Cd or silicate, used for growing the cultures and for the

Cd bioassay experiment; and (3) media with no added Cd, Ni, or silicate, used for the Ni bioassay experiment. Note that the media used in the bioassay experiment contained EDTA disodium salt dihydrate (1.17×10^{-5} M), a synthetic chelator that binds to metal ions in media (Sunda et al., 2005).

All polycarbonate culture flasks and Teflon/Tygon tubing used for the incubation experiments were soaked in hydrochloric acid (5% HCl, technical grade) for at least three days and rinsed with ultrapure water (Millipore Milli-Q). All Teflon bottles used for the collection and storage of trace metal samples were soaked in 2% detergent (Micro-90) for one day, rinsed with deionized (DI) and ultrapure water, acid-soaked (10% HCl, technical grade) for three days, acid-soaked (1% HCl, reagent grade) for another three days, rinsed with ultrapure water, and stored with acidified ultrapure water (0.024 M HCl, quartz distilled).

3.3.2 Sediment

Sediment was obtained from an undisturbed, terrestrial source point near the coast in Muscat, Oman (23.607° N, 58.595° E). The sediment particles were size-fractionated to collect the 60-100 μm fraction using acid-cleaned, sonicated synthetic nylon screens. This size fraction of particles was within the range of sediment grain sizes observed in the Persian Gulf (Emery, 1956). The trace metal composition of the sediment was determined in the Class-1000/100 Geochemistry facilities at the National High Magnetic Field Laboratory (NHMFL; Tallahassee, Florida, USA) via microwave digestion (CEM MARS Xpress) with nitric acid (HNO_3) and hydrofluoric acid (HF), followed by quantification using high-resolution magnetic sector inductively coupled plasma-mass spectrometry (ICP-MS; Thermo ELEMENT 2; Morton et al., 2013). The trace metal composition of the sediment was compared to that of upper continental crust (Rudnick and Gao, 2003) and Oman ophiolite (Table B.1 in the Appendix; Hanghøj et al., 2010).

3.3.3 CO_2/sediment incubation experiment

C. polykrikoides cultures were maintained in a total of three CO_2 treatments (400, 800, and 1200 ppmv) in an ocean acidification experimental design consistent with recommendations from Cornwall and Hurd (2016). Five days prior to the start of the experiment,

the media in each of the reservoir headers were purged continuously using 3-component compressed gas mixtures of CO_2 (400, 800, or 1200 ppmv), 21% O_2, and balance N_2. One day prior to the start of the experiment, *C. polykrikoides* cells were centrifuged (300 RCF, 3 min), resuspended, and acclimated in L1 media with no added trace metals, EDTA, or silicate. At the start of the experiment, after the desired pH levels were maintained in the reservoirs, 1 L of the compressed gas-amended media from each of the reservoir headers was carefully siphoned into each of five culture flasks per CO_2 treatment. Aliquots of acclimated *C. polykrikoides* cells were then transferred into three experimental flasks (culture with sediment) and one reference flask (culture without sediment) per treatment to yield initial cell concentrations of 2.4×10^3 cells L^{-1} in each flask. Cell concentrations were low in order to prevent changes in pH or dissolved oxygen over time. Equal aliquots (500 mg) of the size-fractionated sediment were added to each of the three experimental flasks and one sediment blank flask (sediment only, no culture) per treatment. The flask containing only sediment was used as a blank for chlorophyll *a* concentrations. The amount of sediment added in this incubation experiment was within the range of observed levels of suspended solids in coastal waters of the Persian Gulf (Al Yamani, 2008; Gaillardet et al., 1999).

The flasks were randomly positioned in the incubator and gently swirled at least once a day over the course of the 35-day batch culture incubation experiment. Cultures were maintained over an extended period of time since trace metals have been shown to exhibit a broad range of dissolution rates from mineral particles (Mackey et al., 2015). The media in the reservoirs (not in the culture flasks) were continuously purged with compressed gas throughout the experiment. The headspace of each bubbled reservoir was connected to the headspaces of all five associated flasks to maintain constant pH and dissolved oxygen concentrations. In order to show that the *C. polykrikoides* cells in the experimental treatments were trace metal limited, L1 trace metals and EDTA were added to the reference flask in each treatment after 16 days to stimulate *C. polykrikoides* growth (Figure B.1 in the Appendix). Trace metals and EDTA were not added to the experimental flasks containing sediment. Samples were obtained throughout the experiment by careful airtight siphoning of approximately equal volumes from all flasks.

Since the pH and dissolved oxygen of overlying water have been shown to impact trace metal release from sediments (Atkinson et al., 2007) and since algal cultures can impact the concentrations of dissolved gases during exponential growth, both pH and dissolved oxygen were monitored throughout the course of the incubation experiment to ensure that these concentrations remained constant in the growth media. Measurements of pH on the National Bureau of Standards (NBS) scale were obtained using a bench-top pH meter calibrated against NBS buffers (Thermo Scientific Orion Star A211) to determine relative differences in pH among treatments (Table B.2 in the Appendix). Dissolved oxygen concentrations were measured using a 4-channel fiber-optic sensor with an external probe for automatic temperature compensation (FireSting; Table B.2 in the Appendix).

Trace metal samples collected at the start of the experiment (following sediment addition), after 22 days, and after 35 days of incubation were 0.22 μm filtered through ultrapure water-rinsed polyvinylidene fluoride (PVDF) filters with modified acrylic housings using rinsed polypropylene/polyethylene (PP/PE) syringes. Samples were stored in trace metal clean Teflon fluorinated ethylene propylene (FEP) bottles, immediately acidified (0.024 M HCl, quartz distilled), and stored double-bagged (Uline Minigrip) at room temperature for less than a month until trace metal pre-concentration, extraction, and analysis via ICP-MS. Dissolved trace metals including Fe, Cd, Ni, Cu, Zn, Pb, manganese (Mn), and cobalt (Co) were quantified in the trace metal clean facilities at the NHMFL. Aliquots of the filtered, acidified samples were UV-oxidized in the FEP bottles for 1.5 hours to release metals (e.g., Cu and Co) from organic ligands and subsampled (5 mL) into quartz tubes. Each sample aliquot was spiked with two standards: (1) an enriched stable isotope standard (^{57}Fe, ^{111}Cd, ^{62}Ni, ^{65}Cu, ^{68}Zn, and ^{207}Pb) to quantify concentrations by isotope dilution and (2) a monoisotope standard (Mn and Co) to quantify concentrations by standard additions (Milne et al., 2010). Trace metals were extracted from the seawater matrix using an automated form of the extraction procedure used by Milne et al. (2010) with a chelating resin column containing Nobias Chelate PA-1 resin as described by Biller and Bruland (2012). Samples were buffered in-line with ammonium acetate (0.4 M) to pH 5.5-5.8. Metals were eluted from the column with 0.5 mL of HNO_3 (1.0 M, quartz distilled) at a pre-concentration factor of ~10. Eluted samples were analyzed along with isotope dilution calibration stan-

dards using high-resolution magnetic sector ICP-MS (Thermo ELEMENT 2; Table B.3 in the Appendix). Concentrations of dissolved trace metals were determined in experimental treatments and background pure L1 media (Table B.3 in the Appendix). The rates of change of dissolved trace metals were also determined within each treatment (Table B.4 in the Appendix).

Nutrient samples were 0.22 μm syringe-filtered and frozen at -80°C until analysis. Concentrations of phosphate, nitrate, nitrite, ammonium, and silicate were determined using a modular nutrient analyzer (Seal Analytical AA3 AutoAnalyzer; Table B.5 in the Appendix).

In vivo fluorescence was measured using a bench-top fluorometer (Turner Designs Trilogy). Chlorophyll *a* concentrations were calculated using a calibration of *in vivo* fluorescence and extracted chlorophyll *a* ($R^2 = 0.999$; Table B.6 in the Appendix; Huot and Babin, 2011; JGOFS, 1996). Growth responses of *C. polykrikoides* were assessed using chlorophyll *a* concentrations rather than cell counts (e.g., Ebenezer and Ki, 2012) due to the interference of sediment particles in cell count measurements. Chlorophyll *a* concentrations were correlated with cell counts in pooled data from all experimental treatments ($R^2 = 0.604$; data not shown). Subsamples of *C. polykrikoides* culture were preserved in neutral Lugol's iodine solution (2% final concentration) and counted using a bench-top automated particle analysis instrument (FlowCam B3 Series) fitted with a 4× objective and a 300-μm field-of-view flow cell. Growth rates were determined using the exponential growth equation of chlorophyll *a* concentrations over the exponential phase of growth at the last four time points from 19 to 35 days ($R^2 > 0.911$ except at 1200 ppmv where growth was inhibited; Table B.7 in the Appendix). Growth rates for reference cultures were determined in the same way. *C. polykrikoides* cell morphology was examined after 37 days of incubation using a multiphoton confocal microscope (Nikon A1R MP) at the Herbert Irving Comprehensive Cancer Center at Columbia University. Images were obtained in order to provide a qualitative assessment of the combined effects of CO_2 and trace metals on *C. polykrikoides* morphology.

3.3.4 Toxicity bioassay experiment

C. polykrikoides batch cultures were maintained in a total of five Cd treatments and six Ni treatments over a range of relevant concentrations based on dissolved trace metal

concentrations from the CO_2/sediment incubation experiment. The trace metals Cd and Ni were chosen for the bioassays based on temporal trends in the CO_2/sediment incubation experiment. In addition, Cd has been reported to be toxic to phytoplankton (Brand et al., 1986; Echeveste et al., 2012; Herzi et al., 2013).

One day prior to the start of the experiment, batches of modified L1 media were prepared under a range of total Ni concentrations (0-300 nM) or Cd concentrations (0-3 nM) by performing serial additions of either nickel(II) sulfate hexahydrate ($NiSO_4 \times 6H_2O$) or cadmium(II) chloride ($CdCl_2$) into 100 mL of L1 media in culture flasks. Positive controls were prepared in L1 media with no added Cd or silicate (10 nM Ni, 0 nM Cd). Also one day prior to the start of the experiment, *C. polykrikoides* cells were centrifuged (300 RCF, 3 min), resuspended, and acclimated in either L1 media with no added Cd or silicate (for the Cd bioassay experiment) or L1 media with no added Cd, Ni, or silicate (for the Ni bioassay experiment). At the start of the experiment, aliquots of acclimated *C. polykrikoides* cells were transferred into three experimental replicates in each Cd and Ni treatment to yield initial cell concentrations of 9.8×10^3 cells L^{-1} in each flask. Cell concentrations were low to allow time for trace metal toxicity responses and to observe growth rates comparable to those in the CO_2/sediment incubation experiment.

Cultures were randomly positioned in the incubator, gently swirled at least once a day, and maintained at ambient CO_2 conditions over the course of the 29-day exposure. Chlorophyll *a* concentrations were obtained as described above and were linearly correlated with cell counts in pooled data from all experimental treatments ($R^2 = 0.933$; data not shown). Subcultures for cell counts were preserved as described above and counted using a compound microscope fitted with a 10× objective using a Sedgewick-Rafter counting slide. Growth rates were determined from exponential increases in chlorophyll *a* at the last four time points from 10 to 29 days, as described above ($R^2 > 0.992$; Table B.8 in the Appendix). Dose-response curves were generated (10-300 nM Ni and 0-3 nM Cd) and effective concentration values at 50% and 90% of the observed maximal growth effects (EC_{50} and EC_{90}, respectively) were calculated based on percent reductions in growth rate relative to the positive control (Table B.9 in the Appendix). Note that EC_{50} and EC_{90} values were

calculated using total added trace metal concentrations (e.g., Ebenezer and Ki, 2012) in media containing EDTA.

Photosynthesis-irradiance (PI) curves were generated during exponential growth after 21 days under a range of Ni concentrations (0-300 nM) or Cd concentrations (0-3 nM) using a bench-top Fluorescence Induction and Relaxation (FIRe) system (Gorbunov and Falkowski, 2004) as described by Gorbunov et al. (2001). PI curves were used as physiological assays for Ni and Cd since both trace metals have been shown to impact photosystem II (PSII; Boisvert et al., 2007; Perreault et al., 2011; Sunda, 1989). Relative rates of photosynthetic electron transport were calculated according to the following equation, as described by Suggett et al. (2011):

$$ETR = I \times a_{PSII} \times \phi_{PSII} \tag{3.1}$$

where ETR is the relative electron transport rate, I is the actinic light intensity, a_{PSII} is the absorption cross-section of PSII, and ϕ_{PSII} is the quantum efficiency of photochemistry under actinic light. Note that the rates of electron transport were relative measures of photosynthesis since values were not normalized to unit chlorophyll and rates were not measured in units of carbon fixation or oxygen production. The slope of the light-limited portion of the PI curve (alpha, α) was determined using a linear regression of the first five light levels ($R^2 > 0.972$; Table B.10 in the Appendix). Differences in maximum relative rates of electron transport (P_{max}; μmol electrons m^{-2} s^{-1}) were determined using Michaelis-Menten curve fitting over irradiances of 0-600 μmol quanta m^{-2} s^{-1} (Table B.10 in the Appendix; Ritchie, 2008).

Free metal ion concentrations of Cd and Ni were obtained using Visual MINTEQ software version 3.1. Input data included pH, temperature, ionic strength (0.701 M at salinity = 34; Pilson, 1998), partial pressure of CO_2, concentrations of major components of natural seawater at salinity = 34 (Table B.11 in the Appendix; calculated according to Pilson, 1998), concentrations of components of media in each treatment (e.g., Table B.12 in the Appendix), and mean measured dissolved trace metal concentrations (CO_2/sediment incubation experiment only).

3.3.5 Statistical analyses

Data were analyzed using Prism GraphPad software (version 7). Linear regressions were applied to pH, dissolved oxygen, and dissolved trace metal data to determine significant changes over time. Paired *t*-tests at 95% confidence were used to analyze macronutrient data to determine significant differences between the initial and final time points. One-way analysis of variance (ANOVA) with multiple comparisons and Fisher's LSD tests was applied to dissolved trace metal, macronutrient, growth rate, and α and P_{max} data to determine significant differences among treatments. Two-way ANOVA with multiple comparisons and Fisher's LSD tests was applied to pH and dissolved oxygen data to assess significant differences among treatments at all sampling time points.

3.4 Results

3.4.1 CO_2/sediment incubation experiment

The trace metal analysis of the size-fractionated sediment used in the incubation experiment indicated that the sediment from Oman contained 0.10 ± 0.01 ppm Cd and 454 ± 18 ppm Ni (mean ± SEM; Table B.1 in the Appendix). The sediment was strongly enriched in Ni and slightly enriched in Co compared to the upper continental crust, but not compared to Oman ophiolite (Table B.1 in the Appendix).

The measured pH remained constant in each treatment between 0 and 35 days (linear regression; Table B.2 in the Appendix). At all sampling time points, pH values were significantly different among treatments (two-way ANOVA, $p < 0.001$; Table B.2 in the Appendix). The measured pH_{NBS} values at 400, 800, and 1200 ppmv CO_2 were 8.13 ± 0.01, 7.89 ± 0.01, and 7.74 ± 0.01, respectively (mean ± SEM). Dissolved oxygen concentrations remained constant in each treatment between 0 and 35 days (linear regression; Table B.2 in the Appendix). Dissolved oxygen concentrations were not significantly different among treatments at all sampling time points (two-way ANOVA; Table B.2 in the Appendix).

Dissolved Fe concentrations significantly increased over time at 1200 ppmv CO_2 (linear regression, $p = 0.0017$; Table B.4 in the Appendix). After 35 days, concentrations were significantly elevated at 1200 ppmv CO_2 compared to 400 ppmv (one-way ANOVA, $p =$

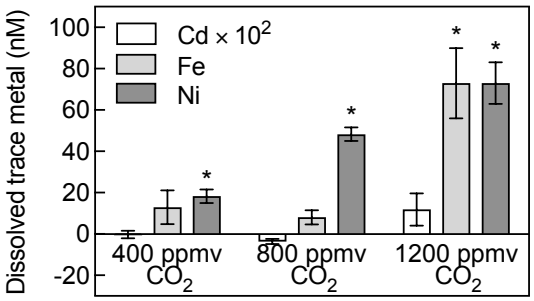

Figure 3.1: Concentrations of dissolved trace metals due to mobilization from sediment after 35 days in the *Cochlodinium polykrikoides* growth media at 400, 800, and 1200 ppmv CO_2 (mean ± SEM; n = 3 for all treatments), calculated from differences between total measured dissolved trace metals in experimental treatments and in background L1 media ($*$ indicates statistical significance compared to the other treatments based on pair-wise comparisons of one-way ANOVA, $p < 0.05$).

0.0086; Figure 3.1) and 800 ppmv CO_2 ($p = 0.0060$). Concentrations were significantly different from background media after 35 days at 1200 ppmv CO_2 (one-way ANOVA, $p = 0.0007$; Table B.3 in the Appendix). Dissolved Cd concentrations increased over time between 0 and 35 days at 1200 ppmv CO_2 relative to the other treatments, but the trend was not significant (linear regression; Table B.4 in the Appendix). Cd concentrations were not significantly different among CO_2 treatments after 35 days (one-way ANOVA; Figure 3.1). Concentrations of dissolved Cd were not significantly different from the background media (one-way ANOVA; Table B.3 in the Appendix). Dissolved Ni concentrations increased over time at 400 ppmv (linear regression, $p = 0.0014$; Table B.4 in the Appendix), 800 ppmv ($p < 0.001$), and 1200 ppmv CO_2 ($p = 0.0008$). After 35 days, Ni concentrations were significantly higher at 1200 ppmv CO_2 compared to 400 ppmv (one-way ANOVA, $p = 0.0009$; Figure 3.1) and 800 ppmv CO_2 ($p = 0.0334$). Concentrations were significantly different from background media after 22 days at all CO_2 treatments (one-way ANOVA, $p < 0.001$; Table B.3 in the Appendix) and after 35 days at all treatments ($p < 0.05$).

Dissolved Mn concentrations increased over time at 400 ppmv (linear regression, $p < 0.001$; Table B.4 in the Appendix), 800 ppmv ($p = 0.0040$), and 1200 ppmv CO_2 ($p < 0.001$).

However, Mn concentrations were not significantly different among treatments after 35 days (one-way ANOVA; Table B.3 in the Appendix). Mn concentrations were significantly different from background media after 35 days at all CO_2 treatments (one-way ANOVA, $p < 0.001$; Table B.3 in the Appendix). Dissolved Co concentrations did not increase over time (linear regression; Table B.4 in the Appendix). After 35 days, Co concentrations were significantly higher at 1200 ppmv CO_2 compared to 400 ppmv (one-way ANOVA, $p = 0.0419$; Table B.3 in the Appendix) and 800 ppmv CO_2 ($p = 0.0385$). Co concentrations were significantly different from background media after 35 days at 400 ppmv (one-way ANOVA, $p = 0.0064$; Table B.3 in the Appendix) and 800 ppmv ($p = 0.0059$) but not at 1200 ppmv CO_2. Dissolved Cu, Zn, and Pb concentrations did not increase over time (linear regression; Table B.4 in the Appendix) and were not significantly different among treatments after 35 days (one-way ANOVA; Table B.3 in the Appendix). Cu concentrations were significantly different from background media after 35 days at 800 ppmv CO_2 (one-way ANOVA, $p = 0.0362$; Table B.3 in the Appendix), but not at 400 or 1200 ppmv CO_2. Zn and Pb concentrations were not significantly different from background media after 35 days (one-way ANOVA; Table B.3 in the Appendix). Zn concentrations were especially high relative to those in surface seawater (Sunda, 1994).

Nitrate, nitrite, and silicate concentrations were not significantly different between the initial and final time points in all CO_2 treatments (paired t-test; Table B.5 in the Appendix). Ammonium concentrations increased over time at 400 and 800 ppmv CO_2 (linear regression, $p = 0.0025$ and $p = 0.0439$, respectively; Table B.5 in the Appendix), but not at 1200 ppmv CO_2. It is possible that ammonium concentrations increased in the culture flasks at 400 and 800 ppmv CO_2 as a result of metabolic waste production. Ammonium concentrations also increased in the media containing sediment without culture (data not shown), suggesting a possible abiotic effect from sediment. Phosphate concentrations decreased over time at 800 ppmv CO_2 (linear regression, $p = 0.0294$; Table B.5 in the Appendix), but not at 400 or 1200 ppmv CO_2. Phosphate, ammonium, nitrite, and silicate concentrations were not significantly different among treatments after 35 days (one-way ANOVA; Table B.5 in the Appendix). Nitrate concentrations were significantly different at 800 and 1200 ppmv CO_2

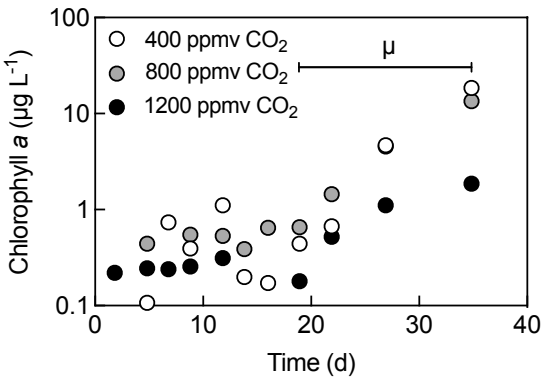

Figure 3.2: Representative *Cochlodinium polykrikoides* growth curves from one of the replicates in each treatment following sediment additions at 400, 800, and 1200 ppmv CO_2. The bar labeled "μ" indicates the time interval over which growth rates were calculated.

(one-way ANOVA, $p = 0.0452$; Table B.5 in the Appendix). Macronutrient concentrations were high enough to not be limiting during exponential growth.

Based on chlorophyll *a* concentrations in experimental replicates, cell biomass decreased at high suspended sediment concentrations at elevated CO_2 (Figure 3.2). Growth rates calculated from the exponential increases in chlorophyll *a* concentrations significantly decreased at 1200 ppmv CO_2 compared to 400 ppmv (one-way ANOVA, $p = 0.0048$; Figure 3.3) and 800 ppmv CO_2 ($p = 0.0207$). Growth rates in the reference flask in all treatments exceeded 0.2 d^{-1} over the same time period (Table B.7 in the Appendix). Confocal microscopy images obtained at the end of the incubation experiment indicated decreased cell size and autofluorescence of *C. polykrikoides* cells following sediment additions at 1200 ppmv compared to 800 ppmv CO_2 (Figure 3.4).

3.4.2 Toxicity bioassay experiment

C. polykrikoides growth rates in all Cd and Ni bioassay treatments were significantly decreased compared to the positive control (one-way ANOVA, $p < 0.05$; Figure 3.5a). Dose-response curves based on mean percent reductions in growth rate relative to the positive control indicated dose-dependent, sigmoidal responses of *C. polykrikoides* growth to both Cd and Ni (Figure 3.5b). Note that the toxicity responses represent the effects of added total

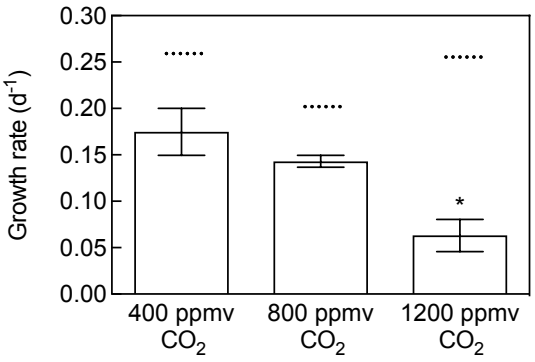

Figure 3.3: *Cochlodinium polykrikoides* growth rates in media with high suspended sediment concentrations at 400, 800, and 1200 ppmv CO_2 (mean ± SEM; n = 3 for all treatments), calculated from exponential increases in chlorophyll *a* between 19 and 35 days (∗ indicates statistical significance compared to the other treatments based on one-way ANOVA, $p < 0.05$). The dotted lines indicate the growth rate in the reference flask (culture without sediment) in each treatment.

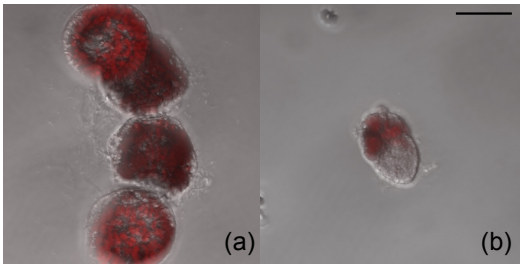

Figure 3.4: Confocal microscopy images of representative *Cochlodinium polykrikoides* cells after 37 days in media with high suspended sediment concentrations at (a) 800 ppmv CO_2 and (b) 1200 ppmv CO_2. Scale bar = 25 μm.

Table 3.1: Effective concentration values at 50% and 90% of the observed maximal growth (EC_{50} and EC_{90}; mean ± SEM; n = 3 for all treatments) derived from the Cd and Ni dose-response curves.

Trace metal	EC_{50} (nM)	EC_{90} (nM)
Cd	0.44 ± 0.01	1.53 ± 0.01
Ni	25.3 ± 1.1	44.6 ± 1.2

trace metals in the presence of EDTA to the base seawater media. Effective concentrations at 50% and 90% of the maximal growth response (EC_{50} and EC_{90}, respectively) were determined using the dose-response curves (Table 3.1).

PI curves obtained after 21 days during exponential growth were used to calculate relative differences in α and P_{max} parameters for Cd and Ni (Figure 3.6). In the Ni experiment, α parameters in all experimental treatments were not significantly different from those in the 0 nM Ni treatment, with the exception of 60 nM Ni (one-way ANOVA, $p = 0.0262$; Table B.10 in the Appendix). P_{max} parameters in all treatments were significantly different from those in the 0 nM Ni treatment (one-way ANOVA, $p < 0.01$; Table B.10 in the Appendix). In the Cd experiment, α and P_{max} parameters in all experimental treatments were significantly different from those in the 0 nM Cd treatment (one-way ANOVA, $p < 0.01$; Table B.10 in the Appendix). The PI curves for Cd and Ni indicated decreased overall photosynthetic capacity at high Cd and Ni concentrations.

Based on the comparison of mean free metal ion concentrations in the CO_2/sediment incubation experiment and the toxicity bioassay experiment (Table 3.2), the calculated Ni^{2+} concentrations were lower in the Ni bioassay experiment due to complexation with EDTA. The mean background-corrected Ni^{2+} concentration at 1200 ppm after 35 days of incubation in the CO_2/sediment experiment (54.8 nM; Table 3.2) was orders of magnitude higher than the mean Ni^{2+} concentration in the 300 nM Ni bioassay treatment (0.13 nM). The calculated Cd^{2+} concentrations in the CO_2/sediment incubation experiment were within the range of the concentrations tested in the Cd bioassay experiment (Table 3.2). The mean background-corrected Cd^{2+} concentration at 1200 ppm after 22 and 35 days in the

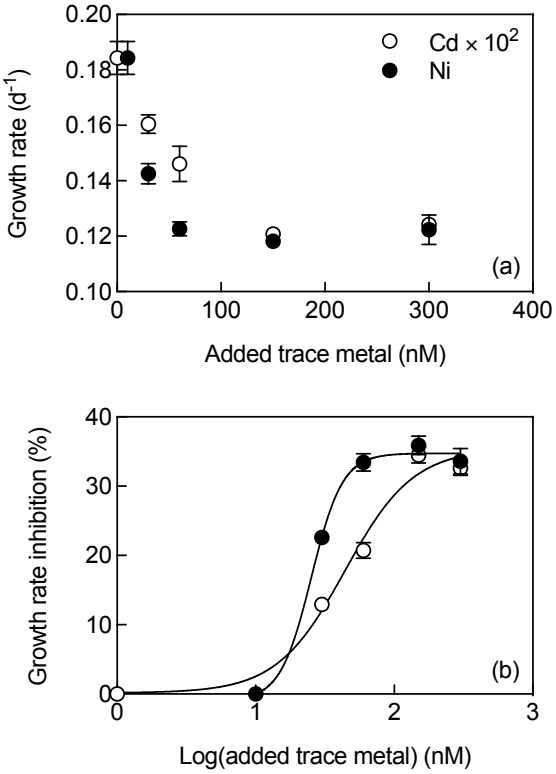

Figure 3.5: *Cochlodinium polykrikoides* growth response curves at ambient CO_2 under a range of total Cd or Ni concentrations (without sediment). (a) Growth rates as a function of added total trace metals (mean ± SEM; n = 3 for all treatments), based on exponential increases in chlorophyll *a* between 10 and 29 days. (b) Dose-response curves (mean ± SEM; n = 3 for all treatments), based on percent reductions in growth rate relative to the positive control.

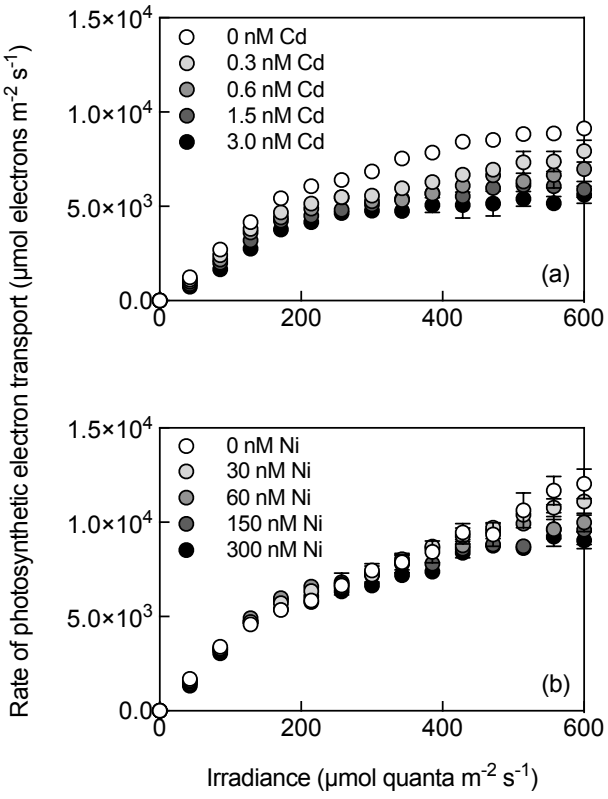

Figure 3.6: Photosynthesis-irradiance (PI) curves obtained after 21 days during exponential growth at ambient CO_2 under a range of total added (a) Cd or (b) Ni concentrations (without sediment; mean ± SEM; n = 3 for all treatments).

CO_2/sediment experiment (0.003 nM; Table 3.2) was similar to the mean added Cd^{2+} concentration in the 0.3 nM Cd bioassay treatment (0.005 nM).

3.5 Discussion

This is the first investigation of the toxic, synergistic effects of trace metals mobilized from suspended sediments and high CO_2 on phytoplankton growth rates and photosynthesis. This study fulfilled the objectives and addressed the research needs: (1) to elucidate the effects of specific components of mineral particles on individual phytoplankton species, consistent with recommendations from Paytan et al. (2009); (2) to examine the biological responses to multiple environmental factors including ocean acidification, consistent with recommendations from Doney et al. (2009) and Hoffmann et al. (2012); and (3) to determine the implications of ocean acidification on noncalcifying marine organisms, consistent with recommendations from Connell and Russell (2010).

Results of the CO_2/sediment incubation experiment support the first hypothesis outlined above that lithogenic trace metal concentrations would increase under increasing CO_2. In this study, high CO_2 (low pH) conditions increased the concentrations of dissolved Fe and Ni due to mobilization from sediments (Figure 3.1, Table B.3, Table B.4 in the Appendix). Increasing dissolved trace metal concentrations over time at 1200 ppmv CO_2 likely resulted from increased leaching from sediment, e.g., as a result of increased solubility (Millero et al., 2009) or increased total free metal concentrations (Millero et al., 2009; Xu et al., 2012). The increasing total dissolved Fe concentrations at high CO_2 may have been driven by increased free Fe(II) concentrations (Millero et al., 2009) combined with decreased Fe uptake due to growth inhibition or decreased bioavailability (Shi et al., 2010). It is important to note that adsorption of Fe on the walls of the culture bottles could have also affected the concentrations of dissolved Fe over the course of the incubation experiment (Fischer et al., 2007).

Dissolved Cd concentrations increased at high CO_2 (Figure 3.1, Table B.3, Table B.4 in the Appendix) but the trend was not significant, likely because most of the Cd signal

Table 3.2: Mean total Cd and Ni concentrations and calculated free Cd^{2+} and Ni^{2+} concentrations for all experimental treatments in the CO_2/sediment incubation experiment, calculated from differences between trace metals in experimental treatments and in background L1 media, and in the toxicity bioassay experiments under a range of Cd or Ni. Free metal ion concentrations (determined using Visual MINTEQ) in the CO_2/sediment experiment were calculated using measured dissolved trace metals (Table B.3 in the Appendix), while those in the toxicity bioassay experiments were calculated using the amounts of trace metals added. Ni^{2+} concentrations in the Cd toxicity bioassay were identical because total added Ni was constant (10 nM). Cd^{2+} values in the Ni toxicity bioassay were consistently low because no Cd was added.

Treatment	Cd (nM)	Cd^{2+} (nM)	Ni (nM)	Ni^{2+} (nM)
400 ppmv CO_2 (with sediment)				
0 days	0.0	-9.0×10^{-6}	0.2	-0.3
22 days	0.0	-9.0×10^{-6}	16.9	12.0
35 days	0.0	-9.0×10^{-6}	18.4	13.1
800 ppmv CO_2 (with sediment)				
0 days	0.0	4.0×10^{-6}	3.3	2.4
22 days	0.0	4.0×10^{-6}	37.7	28.0
35 days	0.0	4.0×10^{-6}	48.4	35.9
1200 ppmv CO_2 (with sediment)				
0 days	0.0	9.0×10^{-6}	7.3	5.6
22 days	0.1	3.4×10^{-3}	68.9	51.6
35 days	0.1	3.4×10^{-3}	73.2	54.8
Cd toxicity bioassay (without sediment)				
0 nM Cd	0.0	1.7×10^{-9}	10.0	3.4×10^{-3}
0.3 nM Cd	0.3	5.2×10^{-3}	10.0	3.4×10^{-3}
0.6 nM Cd	0.6	1.0×10^{-2}	10.0	3.4×10^{-3}
1.5 nM Cd	1.5	2.6×10^{-2}	10.0	3.4×10^{-3}
3.0 nM Cd	3.0	5.2×10^{-2}	10.0	3.4×10^{-3}
Ni toxicity bioassay (without sediment)				
0 nM Ni	0.0	1.7×10^{-9}	0.0	3.3×10^{-11}
10 nM Ni	0.0	1.7×10^{-9}	10.0	3.4×10^{-3}
30 nM Ni	0.0	1.7×10^{-9}	30.0	1.0×10^{-2}
60 nM Ni	0.0	1.8×10^{-9}	60.0	2.1×10^{-2}
150 nM Ni	0.0	1.8×10^{-9}	150.0	5.8×10^{-2}
300 nM Ni	0.0	1.9×10^{-9}	300.0	1.3×10^{-1}

originated from the seawater media base. Calculated free Cd^{2+} concentrations also increased with CO_2 (Table 3.2).

Increasing Ni concentrations at high CO_2 (Figure 3.1, Table B.3, Table B.4 in the Appendix) were likely caused by increased free metal concentrations leaching from the sediment, assuming that natural complexing agents were present in the L1 media (Millero et al., 2009; Xu et al., 2012). Calculated free Ni^{2+} concentrations increased both as a function of time and CO_2 concentration (Table 3.2). The sediment used in this study was highly enriched in Ni content relative to average crustal abundance (Table B.1 in the Appendix), so it is possible that this sediment had relatively high Ni solubility and/or bioavailability. However, the solubility and bioavailability of Ni from the Oman sediment are not known.

Although the sediment was also enriched in Co, dissolved Co concentrations did not increase over time in the incubation experiment (Table B.3 in the Appendix). It has been shown that dissolved Co is intensely complexed in seawater (Baars and Croot, 2015), but it is not known how or to what extent dissolved Co concentrations will change with ocean acidification.

Growth responses in this study indicated that *Cochlodinium polykrikoides* experienced increased lithogenic trace metal toxicity under increasing CO_2 conditions. Sediment inputs together with high CO_2 significantly decreased growth rates (Figure 3.3). Confocal microscopy images qualitatively illustrated the combined impacts of lithogenic trace metals and CO_2 on cell morphology (Figure 3.4). The inhibition of *C. polykrikoides* growth at high CO_2 was not the result of increased CO_2 (decreased pH) alone since the growth rate in the reference flask (culture, no sediment) at 1200 ppmv CO_2 was similar to that in the reference flasks at 400 and 800 ppmv CO_2 (all > 0.2 d^{-1}; Figure 3.3). The biological response was not caused by the sediment alone since *C. polykrikoides* growth rates were significantly higher following sediment additions at 400 and 800 ppmv compared to 1200 ppmv CO_2 (Figure 3.3). Decreased growth rates were not caused by changes in dissolved oxygen, pH, or macronutrient concentrations over the 35-day incubation period (Table B.2, Table B.5 in the Appendix). There were no significant reductions in individual nutrient concentrations

or changes in stoichiometric ratios in the *C. polykrikoides* culture media (Table B.5 in the Appendix).

Results of the toxicity bioassay experiment support the second hypothesis outlined above that increased concentrations of trace metals mobilized from sediments would negatively affect the growth of *C. polykrikoides*. Growth rates significantly decreased under increasing Cd or Ni concentrations (Figure 3.5a). In addition, the biological responses of *C. polykrikoides* to Cd and Ni were dose-dependent (Figure 3.5b). Based on the PI curves from this study (Figure 3.6), it is possible that high concentrations of both Cd and Ni impacted photosynthetic electron transport from PSII. Ni has been shown to cause conformational changes in the oxygen-evolving complex of PSII and inhibit electron transport activity (Boisvert et al., 2007). Cd has been shown to act on several inhibitory sites (on the donor and acceptor side of PSII) and also decrease rates of electron transport (Perreault et al., 2011). However, it is also possible that Cd and/or Ni inhibited growth and decreased photosynthetic electron transport rates via another toxicity mechanism (Sunda, 1994).

Determining the cause of the toxicity response in the CO_2/sediment incubation experiment is not straightforward. Many predictions of trace metal bioavailability assume that the concentration of the free metal ion drives uptake and toxicity (Domingos et al., 2015; Sunda and Huntsman, 1998). Therefore, free metal Cd and Ni concentrations were compared in the CO_2/sediment incubation experiment and the Cd and Ni toxicity bioassay experiments (Table 3.2). In the bioassay experiments, toxic effects were observed at very low Cd^{2+} and Ni^{2+} concentrations, indicating that *C. polykrikoides* was sensitive to both free Cd and Ni (Table 3.2). However, the concentrations of Ni^{2+} were lower in the bioassay compared to the CO_2/sediment experiment as a result of complexation (Table 3.2). It is therefore possible that: (1) total Ni rather than free Ni concentrations explained the toxic effect at high CO_2 or (2) there was an additive or synergistic effect of free Ni with another factor (e.g., free Cd, Zn, or Cu) at high CO_2.

Concentrations of total dissolved Zn and Cu were high relative to surface seawater (Table B.3 in the Appendix; Morel and Price, 2003; Sunda, 1994). The average concentrations of free Zn^{2+} and Cu^{2+} calculated at 1200 ppmv CO_2 after 35 days (141 nM and 3.6 nM, respectively; data not shown) were within the ranges shown to be toxic to marine phyto-

plankton (Brand et al., 1986; Miao et al., 2005; Sunda, 1994). Although Zn and Cu did not exhibit significant temporal or CO_2-dependent trends (Table B.4 in the Appendix), it is possible that either Zn or Cu contributed to the increasing toxicity of suspended sediments at high CO_2.

It is also possible that the calculated Ni^{2+} in the CO_2/sediment incubation experiment was overestimated due to complexation by a ligand or agent not represented in the Visual MINTEQ speciation calculation. The extent of complexation of trace metals to ligands (e.g., biotic ligands, inorganic species) or particles (e.g., humic substances, iron manganese oxides, clays) can significantly impact their bioavailability and toxicity (Domingos et al., 2015; Meyer et al., 1999; Sunda and Huntsman, 1998). Ligand composition was not measured in this study, but it is possible that the sediment or the organism itself altered the composition of metal-chelating agents in the media and caused free Ni to become complexed (Sunda and Huntsman, 1998; Sunda et al., 2005).

Several studies have shown that free metal ion concentrations do not always best predict toxicity responses in the presence of biotic ligands (e.g., De Schamphelaere et al., 2005; Meyer et al., 1999). For example, external cellular Cu (the concentration of Cu removed from algae by adding EDTA) better predicted the toxicity responses of freshwater green algae under a range of pH than free Cu^{2+} (De Schamphelaere et al., 2005). It is possible that the modeled free ion concentrations were not the best predictors of toxicity in the CO_2/sediment incubation experiment.

If, instead, total dissolved Cd and Ni concentrations adequately predicted the toxicity responses of *C. polykrikoides* in this study, total Cd likely did not cause the toxicity response in the CO_2/sediment incubation experiment since most of the Cd signal originated from the seawater media base. Dose-responses were, however, consistent with Ni toxicity in the CO_2/sediment incubation experiment. Although the toxicity of total Ni likely increased at high CO_2, there may have been some other factor(s) contributing to toxicity. It is possible that the presence of some other undetected trace metal(s) or chemical(s) present in the sediment and/or some additive or synergistic effect (e.g., from the relatively high dissolved Zn or Cu concentrations) could have contributed to the toxic response at high CO_2.

Additional experiments are required to better understand the combined effects of CO_2 and suspended sediments on the growth of phytoplankton. In particular, the interactive toxic effects of specific components of sediment (e.g., different free metals) need to be characterized. Additionally, the impacts of ocean acidification on metal complexing agents need to be examined (Millero et al., 2009; Xu et al., 2012). Finally, the combined effects of suspended sediments and ocean acidification in other regions of the world need to be assessed using other phytoplankton species and different sediment sources. Toxicity responses to trace metals dissolved from sediments likely vary significantly depending on phytoplankton species and sediment composition (Brand et al., 1986; Mackey et al., 2012; Paytan et al., 2009). Such studies would improve understanding of the complex impacts of ocean acidification on marine biogeochemical dynamics.

The experimental results presented here indicate that high suspended sediment concentrations could deliver potentially toxic concentrations of trace elements (e.g., total Ni) to coastal marine ecosystems such as the Persian Gulf over the course of this century. The results strongly suggest that beyond a certain threshold, a combination of increased CO_2 (decreased pH) together with elevated suspended sediment concentrations could significantly decrease growth rates and photosynthesis of marine phytoplankton, as shown in the case of *C. polykrikoides*. Under moderate CO_2 conditions, sediments may not be inhibitory to *C. polykrikoides* growth. Growth rates may decrease significantly at high CO_2 and high dissolved Ni concentrations, however some other factor(s) present in sediments could also contribute to the biological response. These results may help improve predictions of ecosystem-biogeochemical models over the course of this century.

3.6 Acknowledgements

The authors would like to thank Andrew Juhl and Hugh Ducklow for their thoughtful comments, insights, and advice; William Landing and Maxim Gorbunov for their logistical support; Tegan Gallina, Palita Tong, and Martin Fleisher for their laboratory assistance; Theresa Swayne and Cedric Espenel at the Herbert Irving Comprehensive Cancer Center at Columbia University for their assistance with confocal microscopy; and three anony-

mous reviewers for their constructive comments on the manuscript. This work was partly supported by NASA Headquarters under the NASA Earth and Space Science Fellowship Program grant 13-EARTH13F-0131 and 14-EARTH14R-0001. Funding at the National High Magnetic Field Laboratory was provided by the National Science Foundation Cooperative Agreement DMR-1157490, the State of Florida, and the U.S. Department of Energy. The authors declare no conflicts of interest.

Chapter 4

Influence of shell-associated bacteria on gastropod larvae and adult *Limacina helicina* pteropods under ocean acidification conditions

Note: A modified version of this chapter was originally published as Bausch, A. R., Gallego, M. A., Harianto, J., Thibodeau, P., Bednaršek, N., Havenhand, J. N., and T. Klinger (2018). Influence of bacteria on shell dissolution in dead gastropod larvae and adult *Limacina helicina* pteropods under ocean acidification conditions. *Marine Biology* 165(40):1–9. DOI: 10.1007/s00227-018-3293-3.

4.1 Abstract

Ocean acidification (OA) increases aragonite shell dissolution in calcifying marine organisms. It has been proposed that bacteria associated with molluscan shell surfaces *in situ* could damage the periostracum and reduce its protective function against shell dissolution. However, the influence of bacteria on shell dissolution under OA conditions is unknown. In this study, dissolution in dead shells from gastropod larvae and adult pteropods (*Limacina helicina*) was examined following a five-day incubation under a range of aragonite saturation states (Ω_{arag}; values ranging from 0.5 to 1.8) both with and without antibiotics.

Gastropod and pteropod specimens were collected from Puget Sound, Washington (48° 33′ 19″ N, 122° 59′ 49″ W and 47° 41′ 11″ N, 122° 25′ 23″ W, respectively), preserved, stored, and then treated in August 2015. Environmental scanning electron microscopy (ESEM) was used to determine the severity and extent of dissolution, which was scored as mild, severe, or summed (mild + severe) dissolution. Shell dissolution increased with decreasing Ω_{arag}. In gastropod larvae, there was a significant interaction between the effects of antibiotics and Ω_{arag} on severe dissolution, indicating that microbes could mediate certain types of dissolution among shells under low Ω_{arag}. In *L. helicina*, there were no significant interactions between the effects of antibiotics and Ω_{arag} on dissolution. These findings suggest that bacteria may differentially influence the response of some groups of shelled planktonic gastropods to OA conditions. This is the first assessment of the microbial-chemical coupling of dissolution in shells of either gastropod larvae or adult *L. helicina* under OA.

4.2 Introduction

The oceanic uptake of anthropogenic carbon dioxide (CO_2) significantly affects seawater carbon chemistry and causes decreases in pH and aragonite saturation state – a process known as ocean acidification (OA). OA represents a significant threat to calcifying marine organisms, particularly shelled molluscs (Gazeau et al., 2013), some of which serve important roles in pelagic food webs and the export of carbon to the deep ocean (Berner and Honjo, 1981; Hunt et al., 2008). Planktonic, highly motile gastropod larvae and adult thecosome pteropods may be especially sensitive to changes in ocean chemistry due to their thin shells and incomplete protection of the outer organic layer of their shells (periostracum), resulting in rapid dissolution of the aragonite shell matrix under low aragonite saturation state (Ω_{arag}; e.g., Bednaršek et al., 2012b, 2016; Gazeau et al., 2013). Pteropods in particular serve as one of the first bioindicators of OA in pelagic marine ecosystems (Bednaršek et al., 2012a, 2014b, 2016).

Extensive dissolution of the exterior of larval and adult pteropod shells has been demonstrated under OA in both field studies and laboratory experiments. In naturally undersaturated waters in the field, severe shell dissolution was observed among live juveniles of the

pteropod *Limacina helicina antarctica* (Bednaršek et al., 2012b). In laboratory incubation experiments, significant changes in shell size and degradation were also observed in the pteropod *Limacina helicina* under simulated OA (e.g., Busch et al., 2014; Lischka and Riebesell, 2012; Lischka et al., 2011), and complete shell loss was observed in larvae of the pteropod *Cavolinia inflexa* under OA conditions (Comeau et al., 2010). Based on similar shell structure and mineralogical composition, it is presumed that the pelagic larvae of benthic gastropods may also be particularly susceptible to dissolution under OA (Gazeau et al., 2013).

Aragonite dissolution in shelled molluscs such as *L. helicina* occurs over the surface of the entire shell rather than simply at the oldest, inner whorls or along the newest, growing edge (Bednaršek et al., 2012b). The periostracum, an outer organic layer of the shell, exists as a barrier between the mineral layers of the shell and ambient seawater (Harper, 2000; Peck et al., 2016) but does not provide sufficient protection against chemical dissolution under OA conditions (Bednaršek et al., 2016). Although shell dissolution can occur despite an intact periostracum, the local thinning or degradation of this protective veneer can further exacerbate dissolution damage at discrete sites on the shell surface (Bednaršek et al., 2016; Gazeau et al., 2013) – a process similar to that seen in nassariid gastropods (Garilli et al., 2015). It has been recognized for some time that bacteria living in association with mollusc shells could decrease the pH of the shell microenvironment via respiration, resulting in shell damage and potential loss of integrity of the organic matrix (Clark, 1999; Glover and Kidwell, 1993). However, a search of the literature found no information on the influence of bacteria on the extent of dissolution among gastropod shells, especially under OA.

In this study, we examined dissolution of dead shells from gastropod veliger larvae and adult thecosome pteropods resulting from a five-day exposure to a range of Ω_{arag} both with and without antibiotics. To examine the effects of bacteria on dissolution under simulated OA, the research objectives of this study were threefold: (1) to determine the influence of Ω_{arag} on shell dissolution; (2) to determine the influence of bacteria on shell dissolution under a range of Ω_{arag}; and (3) to examine the dissolution responses among gastropod larvae and adult *L. helicina* collected from Puget Sound, Washington, USA, where waters are seasonally subjected to corrosive conditions (Feely et al., 2008, 2010). We hypothesized

that: (1) shell dissolution would increase with decreasing Ω_{arag} and (2) shell dissolution would increase in the absence of antibiotic treatments (due to presumably higher numbers of shell-associated bacteria).

4.3 Materials and methods

4.3.1 Specimen collection and sorting

Gastropod veliger larvae and adult *Limacina helicina* pteropods were collected from Puget Sound, Washington, USA (Figure 4.1), preserved, stored, and later treated. We examined the effects of OA and antibiotics on shells of dead specimens for several reasons: (1) to describe the response of shell dissolution to bacteria in seawater; (2) to isolate the role of bacteria in shell dissolution under OA conditions, independent of the physiological effects of live molluscs (as in Manno et al., 2012); and (3) to avoid the logistical challenges of maintaining healthy specimens in culture (Manno et al., 2017), particularly under low Ω_{arag} conditions unsuitable for pteropod maintenance.

Live gastropod larvae were collected from San Juan Channel (48° 33′ 19″ N, 122° 59′ 49″ W) on August 6, 2015 by plankton tow (310 μm mesh) at a maximum depth of 50 m (T = 12.8 ± 0.2°C, S = 29.8, Ω_{arag} = 1.08 ± 0.03; mean ± SD). These were the planktonic larvae of benthic gastropod species. Specimens were sorted under a dissecting microscope, rinsed with filtered seawater (0.22 μm), and preserved by air-drying for 24 hours (as in Peck et al., 2016). Inspection showed that all gastropod veliger larval specimens had dextrally coiled shells and therefore were not opisthobranchs (the taxonomic group that includes Pteropoda). We could not classify the larval specimens any further solely based on morphological characteristics. These non-pteropod gastropod larvae are hereafter referred to as "gastropod larvae".

Limacina helicina specimens were collected from Puget Sound Station P28 of the Puget Sound Regional Synthesis Model monitoring program (47° 41′ 11″ N, 122° 25′ 23″ W) on October 30, 2014 using a Bongo net (335 μm mesh) at a maximum depth of 188 m (T = 12.2 ± 0.2°C, S = 30.4 ± 0.4, Ω_{arag} = 0.91 ± 0.05). Specimens were preserved in 95% ethanol

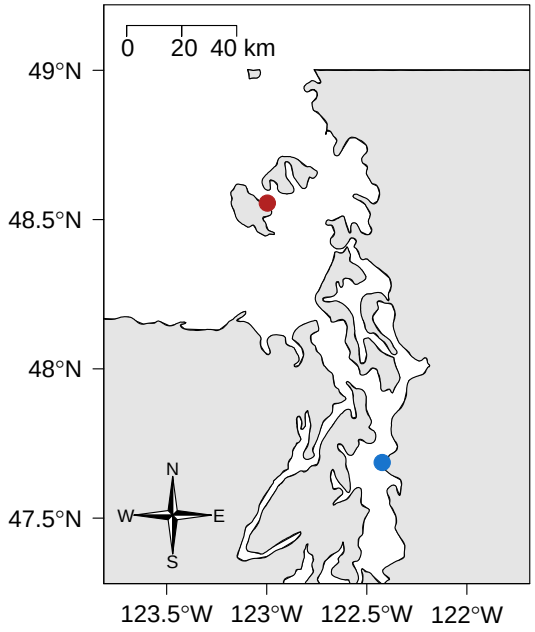

Figure 4.1: Locations of plankton tows to collect gastropod larvae (red) and adult *Limacina helicina* specimens (blue) in Puget Sound, Washington, USA.

for 11 months prior to analysis. This preservation protocol is consistent with numerous previous studies (e.g., Bednaršek et al., 2012a,b, 2016; Busch et al., 2014).

From these specimens, subsamples of five gastropod larvae and five pteropods were selected haphazardly as representative untreated specimens and examined using environmental scanning electron microscopy (ESEM) to assess the level and extent of shell dissolution prior to an incubation experiment.

4.3.2 Incubation experiment

Shells of gastropod larvae and *L. helicina* were each treated in a fully factorial orthogonal experiment at six pH levels (7.5, 7.6, 7.7, 7.8, 7.9, and 8.0) and two antibiotic levels (with and without antibiotics) in a total of 12 individual treatment combinations. We used one replicate per treatment combination, with up to five individuals (gastropod or pteropod shells) per treatment vessel (Table 4.1). This regression-based design not only allows for the detection of response norms but also is more powerful than a traditional replicated ANOVA design when the total number of available experimental units is low (Cottingham et al., 2005), as was the case in this study. Treatment pH levels were chosen to reflect environmentally relevant values at the sites of specimen collection (e.g., Murray et al., 2015). Experimental vessels were filled with filtered seawater (0.22 μm) obtained from separate 114 L reservoirs in the Ocean Acidification Environmental Laboratory at Friday Harbor Laboratories, Washington, USA. Although filtered, the seawater was not sterilized and therefore contained bacteria, the effects of which were investigated under various pH conditions with respect to gastropod and pteropod shell dissolution. Reservoirs were maintained at constant temperature and pH using a custom seawater-CO_2 blending system with Honeywell DuraFET process controllers. Antibiotic treatments were inoculated with 25 mg L^{-1} each of ampicillin and streptomycin, as implemented by Maas et al. (2015). The addition of antibiotics slightly decreased the seawater pH_T (pH on the total hydrogen scale) by 0.04 $\pm$ 0.02 pH units, which was insignificant compared to the differences in treatment conditions. We assumed that the antibacterial activity of the ampicillin and streptomycin was similar to that reported in Maas et al. (2015). Ampicillin and streptomycin are known to be synergistically bactericidal for some gram-positive and gram-negative bacteria by inhibiting cell

wall synthesis and protein synthesis (Brunton et al., 2011), however we did not count or otherwise assess bacterial number or density.

Shells of up to five gastropod larvae were selected haphazardly and placed together into each treatment in 960 mL borosilicate glass jars with CO_2-manipulated seawater. Shells of adult pteropods were treated in the same way. Vessels were closed, positioned randomly in an outdoor ambient water bath at *in situ* temperature (T = 14.4 ± 1.0°C), and gently swirled once a day over the course of the five-day incubation. In order to maintain target carbonate chemistry and antibiotic concentrations in the seawater while avoiding shell breakage due to handling, half the volume of seawater in each vessel was replaced carefully once every two days using a siphon with a filter (80 μm).

The pH_T was measured each day in all experimental treatments and reservoirs using a DuraFET pH electrode calibrated against spectrophotometric measurements of pH_T using *m*-cresol purple indicator (average standard uncertainty ± 0.07 pH units; SOP 6b; Dickson et al., 2007). Total alkalinity (A_T) was measured each day from a single reservoir using the potentiometric titration method (average standard uncertainty ± 11 μmol kg^{-1}; SOP 3b; Dickson et al., 2007). Carbonate chemistry parameters including Ω_{arag} (Table 4.1) were calculated for all experimental treatments with CO_2calc (Robbins et al., 2010) using the constants from Mehrbach et al. (1973), as refit by Dickson and Millero (1987). The average combined standard uncertainty in our estimate of Ω_{arag} was ± 0.02, based on methods to propagate uncertainty as recommended by Dickson (2010) using the sensitivity coefficients from Dickson and Riley (1978).

4.3.3 Examination of dissolution

Following the five-day incubation experiment, gastropod larvae and *L. helicina* specimens were recovered from the jars. Shells were cleaned and treated for ESEM analysis using a modified protocol of Bednaršek et al. (2012a, 2016). Briefly, specimens were transferred to 70% ethanol (3–5 minutes), followed by 50% ethanol (3–5 minutes), and distilled water (two consecutive rinses, 2.5 minutes each) to remove crystal deposits from the shells. Shells were then soaked in 6% H_2O_2 (20 minutes), distilled H_2O (two consecutive rinses, 2.5 minutes each), 1% KOH (1–2 hours depending on specimen size), and distilled H_2O

Table 4.1: Conditions during the incubation experiment with non-pteropod gastropod larvae or adult *Limacina helicina* pteropods in treatments with antibiotics (+ AB) and without antibiotics (– AB), including number of individual specimens per treatment (N), temperature (T), salinity (S), pH on the total scale (pH_T), total alkalinity (A_T), and aragonite saturation state (Ω_{arag}). Seawater carbonate chemistry parameters were measured once a day over the course of the five-day incubation (mean ± SD).

Treatment	N	T (°C)	S	pH_T	A_T (µmol kg^{-1})	Ω_{arag}
Gastropod larvae						
+ AB						
7.5	2	14.4 ± 1.0	30.3 ± 0.2	7.44 ± 0.03	2105.47 ± 3.32	0.56 ± 0.02
7.6	2	14.3 ± 1.1	30.3 ± 0.2	7.55 ± 0.07	2105.47 ± 3.32	0.73 ± 0.09
7.7	2	14.3 ± 1.1	30.4 ± 0.2	7.66 ± 0.05	2105.47 ± 3.32	0.90 ± 0.12
7.8	3	14.4 ± 1.2	30.3 ± 0.2	7.79 ± 0.08	2105.47 ± 3.32	1.21 ± 0.25
7.9	2	14.9 ± 1.2	30.4 ± 0.2	7.78 ± 0.03	2105.47 ± 3.32	1.25 ± 0.15
8.0	2	14.5 ± 1.2	30.4 ± 0.2	7.93 ± 0.05	2105.47 ± 3.32	1.60 ± 0.16
– AB						
7.5	1	14.5 ± 1.1	30.3 ± 0.2	7.44 ± 0.04	2105.47 ± 3.32	0.56 ± 0.03
7.6	2	14.5 ± 1.2	30.3 ± 0.2	7.61 ± 0.09	2105.47 ± 3.32	0.86 ± 0.12
7.7	2	14.2 ± 1.0	30.4 ± 0.2	7.72 ± 0.09	2105.47 ± 3.32	1.05 ± 0.25
7.8	1	14.3 ± 1.1	30.3 ± 0.2	7.83 ± 0.09	2105.47 ± 3.32	1.31 ± 0.29
7.9	1	14.3 ± 1.0	30.4 ± 0.2	7.82 ± 0.04	2105.47 ± 3.32	1.26 ± 0.09
8.0	2	14.3 ± 1.0	30.4 ± 0.2	7.99 ± 0.04	2105.47 ± 3.32	1.79 ± 0.15
Limacina helicina						
+ AB						
7.5	3	14.6 ± 1.1	30.3 ± 0.2	7.38 ± 0.03	2105.47 ± 3.32	0.50 ± 0.03
7.6	2	14.5 ± 1.2	30.3 ± 0.2	7.55 ± 0.08	2105.47 ± 3.32	0.72 ± 0.09
7.7	4	14.6 ± 1.2	30.4 ± 0.2	7.62 ± 0.12	2105.47 ± 3.32	0.87 ± 0.27
7.8	4	14.2 ± 0.9	30.3 ± 0.2	7.79 ± 0.08	2105.47 ± 3.32	1.20 ± 0.24
7.9	3	14.5 ± 1.1	30.4 ± 0.2	7.76 ± 0.04	2105.47 ± 3.32	1.13 ± 0.09
8.0	4	14.6 ± 1.1	30.4 ± 0.2	7.93 ± 0.04	2105.47 ± 3.32	1.60 ± 0.14
– AB						
7.5	3	14.3 ± 1.1	30.3 ± 0.2	7.45 ± 0.04	2105.47 ± 3.32	0.57 ± 0.05
7.6	2	14.2 ± 1.0	30.3 ± 0.2	7.59 ± 0.10	2105.47 ± 3.32	0.78 ± 0.13
7.7	4	14.6 ± 0.9	30.4 ± 0.2	7.69 ± 0.08	2105.47 ± 3.32	0.99 ± 0.20
7.8	5	14.7 ± 1.1	30.3 ± 0.2	7.80 ± 0.09	2105.47 ± 3.32	1.19 ± 0.14
7.9	3	14.5 ± 1.2	30.4 ± 0.2	7.77 ± 0.03	2105.47 ± 3.32	1.16 ± 0.10
8.0	3	14.5 ± 1.2	30.4 ± 0.2	7.97 ± 0.04	2105.47 ± 3.32	1.76 ± 0.16

(two consecutive rinses, 2.5 minutes each) to dissolve precipitated crystals and remove the periostracum. This method has been shown not to cause dissolution damage that could result in methodological artefacts (Bednaršek et al., 2012a). The periostracum was removed prior to ESEM analysis for two reasons (Bednaršek et al., 2012a): (1) the periostracum can obstruct visualization of microstructural changes in aragonite crystals and (2) organic remnants of the periostracum can become damaged during sputter-coating and can appear very similar to dissolution. Proper removal of the periostracum immediately prior to ESEM analysis is therefore necessary to accurately assess and quantify the state of dissolution in the aragonite crystals of the shell matrix over the entire shell. Dried shells were carefully mounted dorsal side up on aluminum ESEM stubs, sputter-coated with gold-palladium, and imaged using ESEM (JEOL JCM-5000). Shells with substantial mechanical damage caused by handling (as discussed by Bednaršek et al., 2012a) or shells that were mounted at a non-standard angle on the ESEM stub were excluded from analyses. Images from ESEM were scored blindly and randomly by a single observer using ImageJ Software to quantify the level and extent of shell dissolution. Whole gastropod shells were examined at an average magnification of 220× and whole pteropod shells were examined at an average magnification of 90× to calculate shell surface areas and assess dissolution. Shells were also examined at higher magnification (up to 2700×) to determine the extent of dissolution in different portions of the shells. Shell dissolution was examined visually and categorized according to severity as either: (1) mild dissolution (type I), characterized by partial dissolution of the prismatic layer or (2) severe dissolution (type II and type III), characterized by exposure or dissolution of the crossed-lamellar layer (Bednaršek et al., 2012a, 2014b). The percent areal extent of mild or severe dissolution was determined by manually tracing the area of dissolution using ImageJ. Summed dissolution over the entire shell was calculated as the sum of mild and severe dissolution.

4.3.4 Statistical analyses

Data were analyzed by analysis of covariance (ANCOVA) following arcsine-transformation of response variables to test the effects of the categorical factor (antibiotics) and covariate (Ω_{arag}) on the response variables (percent mild, severe, and summed dissolution). Data were

analyzed in the R statistical framework (version 3.2.4; R Development Core Team, 2016). In order to linearize the relationships between Ω_{arag} and the response variables, the natural logarithm of Ω_{arag} was used as the covariate in the ANCOVA analyses. Untransformed responses were plotted using Prism GraphPad Software (version 7).

4.4 Results

Freshly collected gastropod specimens and preserved *Limacina helicina* specimens not exposed to experimental treatments (i.e., untreated control specimens) showed no evidence of severe shell dissolution. The extent of mild shell dissolution in untreated gastropod larvae ($0.34 \pm 0.39\%$; mean $\pm$ SD) and *L. helicina* ($0.08 \pm 0.08\%$) was lower than that among treated specimens. Total dissolution in the untreated field samples was low despite the marginally-saturated Ω_{arag} conditions in Puget Sound where the gastropod larvae ($\Omega_{arag} = 1.08 \pm 0.03$) and adult pteropods ($\Omega_{arag} = 0.91 \pm 0.05$) were collected. We therefore used dissolution in the untreated samples as a baseline against which we compared dissolution in the treated specimens.

The shells of gastropod larvae from experimental treatments exhibited different degrees of dissolution under a range of Ω_{arag} conditions (ranging from 0.56 to 1.78; Figure 4.2). Overall, 86.4% of gastropod larval shells exhibited mild dissolution (Figure 4.2a) and 27.3% exhibited severe dissolution (Figure 4.2c). The percent areal extents of mild, severe, and summed shell dissolution increased with decreasing Ω_{arag} in treatments both with and without antibiotics (Figure 4.3). In treatments with antibiotics at low Ω_{arag}, the extent of mild shell dissolution was $\leq 3.1\%$ of shell area, severe dissolution was $\leq 7.6\%$, and summed dissolution was $\leq 10.1\%$. In treatments without antibiotics, mild, severe, and summed dissolution were $\leq 7.9\%$, 0.7%, and 8.6%, respectively. Under low Ω_{arag}, the extent of mild dissolution was clearly greater in the absence of antibiotics (Figure 4.3a), whereas the extent of severe dissolution was greater in the presence of antibiotics (Figure 4.3c). The stimulatory effect of antibiotics on severe dissolution was only seen at $\Omega_{arag} < 1.0$, resulting in a statistically significant interaction between antibiotics and Ω_{arag} in the gastropods (ANCOVA, $p < 0.05$; Table 4.2). This interaction indicates that severe dissolution increased

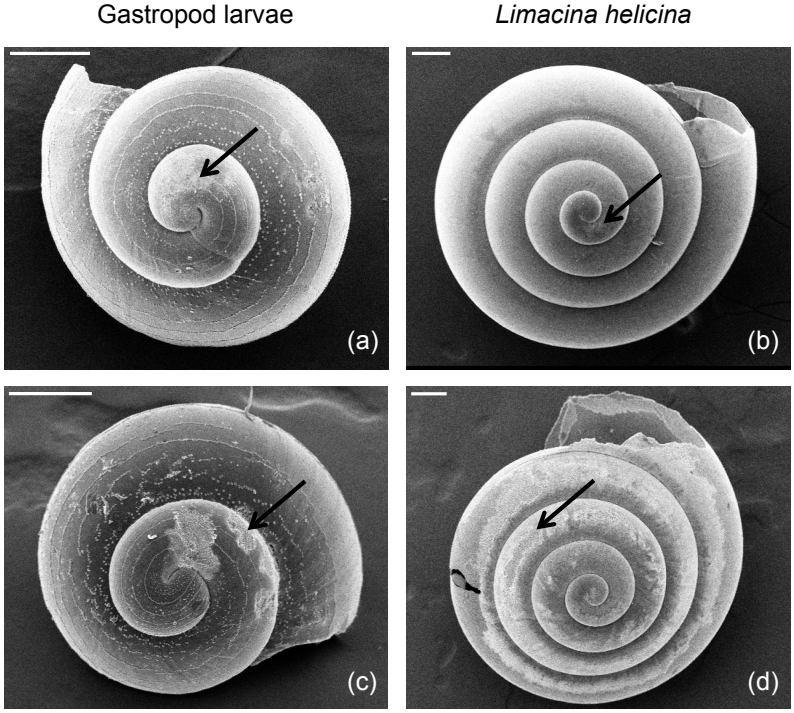

Figure 4.2: Mild (type I) dissolution (a, b) and severe (type II/III) shell dissolution (c, d) indicated by arrows in non-pteropod gastropod larvae and adult *Limacina helicina*, respectively. Scale bar = 100 μm. Environmental scanning electron microscopy (ESEM) images: AR Bausch, MA Gallego, J Harianto, P Thibodeau.

with antibiotics at low Ω_{arag} and, furthermore, the effects of Ω_{arag} depended on the addition of antibiotics. There were no other statistically significant interactions between the effects of antibiotics and Ω_{arag} on percent mild or summed dissolution, but there were highly significant effects of antibiotics (ANCOVA, $p < 0.001$) and Ω_{arag} (ANCOVA, $p < 0.001$; Table 4.2) on both categories of shell dissolution. These findings indicate that mild and summed dissolution increased as Ω_{arag} decreased, and that this response was independent of the addition of antibiotics (Figure 4.3).

The shells of *L. helicina* from experimental treatments also exhibited mild and severe dissolution under different Ω_{arag} conditions (ranging from 0.50 to 1.76; Figure 4.2). Of all pteropod specimens examined, 90.0% exhibited mild dissolution (Figure 4.2b) and 25.0% exhibited severe dissolution (Figure 4.2d). Percent mild, severe, and summed shell dissolu-

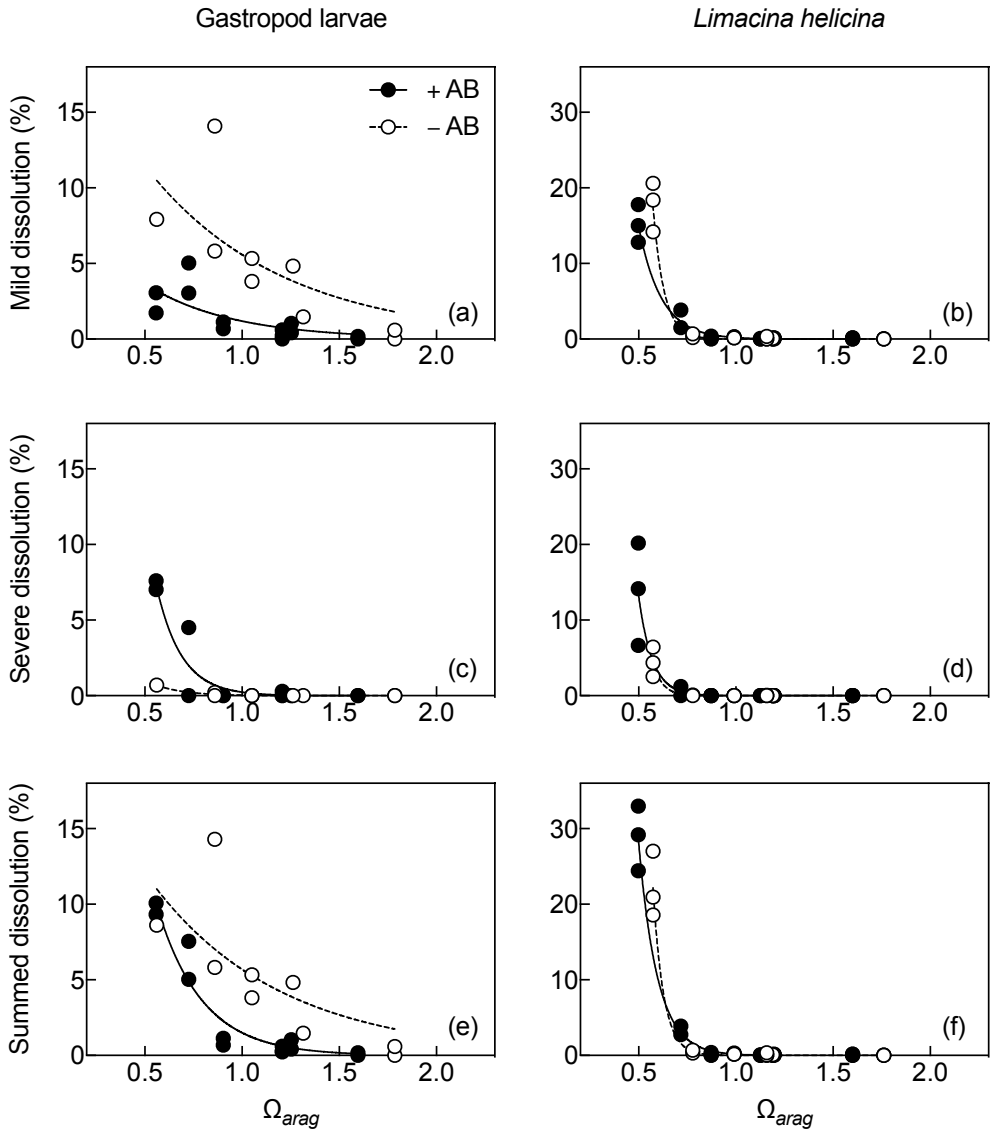

Figure 4.3: Percent mild (type I) dissolution (a, b), severe (type II/III) dissolution (c, d), and summed shell dissolution (e, f) in the five-day incubation with antibiotics (+ AB) and without antibiotics (– AB) as a function of aragonite saturation state (Ω_{arag}) in non-pteropod gastropod larvae and adult *Limacina helicina*, respectively. Exponential curves are included only to illustrate data trends. Each point represents a dissolution response from an individual shell.

Table 4.2: Effects of antibiotics (categorical factor: AB) and the natural logarithm of aragonite saturation state (covariate: Ω_{arag}) on the arcsine-transformed proportion of dissolution among non-pteropod gastropod larvae or adult *Limacina helicina* pteropods using analysis of covariance (ANCOVA).

	SS	*df*	*F*-value	*p*-value	
Gastropod larvae					
Mild dissolution					
AB	0.08186	1	28.1816	4.784×10^{-5}	***
$\ln(\Omega_{arag})$	0.07251	1	24.9648	9.355×10^{-5}	***
AB:$\ln(\Omega_{arag})$	0.00667	1	2.2976	0.1469	
Residuals	0.05228	18			
Severe dissolution					
AB	0.00862	1	2.5681	0.1264	
$\ln(\Omega_{arag})$	0.00420	1	1.2520	0.2779	
AB:$\ln(\Omega_{arag})$	0.02062	1	6.1406	0.0234	*
Residuals	0.06044	18			
Summed dissolution					
AB	0.04390	1	15.9912	8.419×10^{-4}	***
$\ln(\Omega_{arag})$	0.07738	1	28.1897	4.776×10^{-5}	***
AB:$\ln(\Omega_{arag})$	0.00041	1	0.1505	0.7026	
Residuals	0.04941	18			
Limacina helicina					
Mild dissolution					
AB	0.00211	1	0.3051	0.5841	
$\ln(\Omega_{arag})$	0.27727	1	40.0616	2.528×10^{-7}	***
AB:$\ln(\Omega_{arag})$	0.00322	1	0.4658	0.4993	
Residuals	0.24916	36			
Severe dissolution					
AB	0.00258	1	0.4859	0.4903	
$\ln(\Omega_{arag})$	0.06612	1	12.4559	0.0012	**
AB:$\ln(\Omega_{arag})$	0.01510	1	2.8449	0.1003	
Residuals	0.19111	36			
Summed dissolution					
AB	0.00002	1	0.0014	0.9700	
$\ln(\Omega_{arag})$	0.35312	1	31.0071	2.624×10^{-6}	***
AB:$\ln(\Omega_{arag})$	0.00106	1	0.0934	0.7617	
Residuals	0.40998	36			

* $p < 0.05$, ** $p < 0.01$, *** $p < 0.001$

tion in the pteropods all increased at decreasing Ω_{arag} in treatments both with and without antibiotics (Figure 4.3). In specimens treated with antibiotics at low Ω_{arag}, the extent of mild dissolution was $\leq$ 17.8% of shell area, severe dissolution was $\leq$ 20.2%, and summed dissolution was $\leq$ 33.0%. In treatments without antibiotics, mild dissolution was $\leq$ 20.6% of shell area, severe dissolution was $\leq$ 6.4%, and summed dissolution was $\leq$ 27.0%. In all cases, no substantive dissolution was seen at $\Omega_{arag} \geq 1.0$ (Figure 4.3). Among pteropods, there were no statistically significant interactions between the effects of antibiotics and Ω_{arag} on any category of shell dissolution. The main effects of Ω_{arag} on dissolution were, however, statistically significant: mild (ANCOVA, $p < 0.001$); severe (ANCOVA, $p < 0.01$); and summed dissolution (ANCOVA, $p < 0.001$; Table 4.2). These findings indicate that all types of dissolution increased at $\Omega_{arag} \leq 1.0$ but that this response was independent of the addition of antibiotics. For pteropods, there were no statistically significant effects of antibiotics on any category of shell dissolution, indicating that antibiotics did not have any significant impact on the severity of dissolution.

4.5 Discussion

The responses in dissolution to changes in Ω_{arag} in dead shells of both gastropod veliger larvae and the adult pteropod *Limacina helicina* from Puget Sound suggest that both are sensitive to OA. Our finding that all categories of shell dissolution increased significantly under decreasing Ω_{arag} supports our initial hypothesis for both gastropod larvae and adult pteropods that shell dissolution increases with decreasing Ω_{arag}. The dissolution responses among dead *L. helicina* specimens reported here (e.g., $\leq$ 33.0% summed dissolution in treatments with antibiotics at $\Omega_{arag} = 0.50$, $\leq$ 27.0% in treatments without antibiotics at $\Omega_{arag} = 0.57$) are comparable to earlier results of shell degradation among dead *L. helicina* specimens after seven days of incubation under OA conditions (33% total shell degradation at $\Omega_{arag} = 0.72$ in treatments at 2°C, 40% total shell degradation at $\Omega_{arag} = 0.96$ in treatments at 7°C) reported by Lischka and Riebesell (2012). Our results are also comparable to shell corrosion among dead *Limacina retroversa* specimens after eight days of incubation (50% corrosion at $\Omega_{arag} = 0.5$) reported by Manno et al. (2012), as well as

total shell loss among *Limacina helicina antarctica* specimens after 14 days of incubation (17.1% total shell loss at $\Omega_{arag} = 0.8$) reported by Bednaršek et al. (2014a). Our results for dead adult *L. helicina* shells may overestimate dissolution in live specimens, which have been shown to partially repair shell damage (Bednaršek et al., 2014a; Garilli et al., 2015). However, the difference between the rate of abiogenic dissolution and observed shell loss among dead and live juvenile pteropods has been shown to be small (Bednaršek et al., 2014a). Our dissolution results for adult specimens may also underestimate dissolution among *L. helicina* larvae because larval development stages of molluscs have been shown to be particularly sensitive to OA conditions (Gazeau et al., 2013).

The effects of antibiotics on the dissolution responses of gastropod larval shells suggest that bacteria colonizing the surface of the shells could mediate aragonite dissolution and influence the areal extent of shell dissolution under OA. Our finding that mild dissolution increased in the shells of gastropod larvae that were not treated with antibiotics supports our hypothesis that shell dissolution increases in the absence of antibiotic treatments (i.e., with presumably higher numbers of shell-associated bacteria). Interestingly, severe dissolution of gastropod larval shells did not show the same pattern. Percent severe dissolution increased significantly at low Ω_{arag} in treatments with antibiotics, but not without antibiotics (Figure 4.3; interaction term Table 4.2), suggesting that for severe dissolution in the gastropod larvae, the effects of Ω_{arag} depended on the addition of antibiotics. These findings are intriguing given that antibiotic additions decreased the pH_T of the seawater by 0.04 pH units on average, although this change was minimal compared to the relative differences in treatment conditions. We suggest that during the five-day incubation period, the bacteria on the shell surface of the gastropod larvae could have generated sufficiently acidic microenvironments to degrade the periostracum and subsequently enhance mild dissolution but not severe dissolution (Clark, 1999; Glover and Kidwell, 1993). It is also possible that bacteria increased the extent of mild dissolution through the following mechanisms: (1) the bacteria somehow prevented severe dissolution in the gastropod shells, although we suggest this is unlikely as this would require simultaneously decreasing the acidity (increasing the pH and Ω_{arag}) of the shell microenvironment; (2) severe dissolution (only) was largely driven by Ω_{arag}, which was slightly lower in the antibiotic treatments; or (3) the use of antibiotics de-

creased the overall number of bacteria but altered the bacterial community composition (Liu et al., 2010), which influenced the dissolution responses. For example, Witt et al. (2011) reported changes in the composition of the microbial community of a coral reef biofilm under OA conditions. Unfortunately, our data do not allow us to discriminate between these alternative explanations.

In contrast, the responses of the adult pteropod specimens do not suggest that bacteria mediate shell dissolution under OA conditions. Our finding that antibiotics did not significantly influence dissolution in *L. helicina* caused us to reject our hypothesis that shell dissolution increases in the absence of antibiotic treatments among the pteropod specimens. It is important to note that this study examined the extent to which newly colonizing bacteria from the filtered seawater affected dissolution in the non-living shells. The preserved pteropod specimens used in this study likely had no autochthonous bacteria associated with their shells when the experiment began, while the planktonic larvae of benthic gastropod specimens likely had few to none (assuming that most were killed in the washing and drying treatment prior to the incubation experiment). However, we recognize that preservation method represents a potential confounding factor in comparing the dissolution results between the gastropods and the pteropods. Any preservation technique can affect the periostracum to a certain extent. Even preservation in ethanol, which does not change shell characteristics in a way that would introduce methodological artefacts, may alter the primary and secondary – but not the tertiary – structure and ultimately harden the periostracum (Alan Kuzirian, personal communication). Preservation by air-drying may introduce small cracks in the periostracum (Alan Kuzirian, personal communication), but to our knowledge, the effect of air-drying at room temperature over 24 hours on the integrity of the periostracum has never been tested. However, our preservation techniques likely did not change the periostracum in a way that would cause misinterpretation of our results. It is important to note several other confounding factors that could have influenced the outcome of the experiment: (1) the life-stages of the specimens; (2) the location and timing of specimen collections; and (3) the amount of time the specimens were preserved prior to the experiment. Only by repeating this experiment, controlling for the effects of these factors, can their influence be determined.

The influence of microbes on dissolution responses of live and dead shelled zooplankton – and the potential changes in microbial associations themselves – under changing Ω_{arag} offer a fertile area of inquiry and experimentation. In particular, we find the possibility that low Ω_{arag} and the addition of antibiotics could change the composition of the microbial community associated with mollusc shells to be especially intriguing and worthy of additional study. Based on the results we present here, we suggest that such microbial shifts could have significant implications for different life-stages of shelled molluscs and could represent an impediment to shell development or physiology (e.g., by investing more energy into repair processes, building a thicker shell or a stronger periostracum). Additionally, we recommend further study to elucidate the effects of preservation technique on shell dissolution.

This is the first study to demonstrate microbial-chemical coupling of dissolution in gastropod shells under simulated OA conditions. The results suggest that newly colonized microbial communities on the shell surfaces of some planktonic molluscs may mediate certain types of dissolution at low Ω_{arag}. The potential for interactive effects of OA and bacteria on gastropod shell dissolution may be particularly important in surface waters and onshore shelf regions of Puget Sound over the next 50 years (Bednaršek et al., 2014b; Busch et al., 2014). These results may be useful in informing regional model predictions of dissolution responses among planktonic (or sinking, dead) larval and adult shelled molluscs.

4.6 Acknowledgements

The experimental portion of this study was conducted at the University of Washington's Friday Harbor Laboratories, Washington, USA during a graduate student summer course on ocean acidification. The authors would like to thank Andrew Dickson and Laura Newcomb for their advice and insights throughout the course; Jessamyn Johnson and Jan Newton for their advice and for providing the *Limacina helicina* specimens; Kristy Krull, Nicholas Ulacia, and Molly Roberts for their assistance in boat operations to collect the gastropod larvae specimens; Kathryn Van Alstyne and Victoria Foe for providing the antibiotics; Constance Sullivan and the Ocean Acidification Environmental Laboratory staff for their assistance with carbonate chemistry measurements; the Friday Harbor Laborato-

ries faculty and staff for providing funding, facilities, supplies, and logistic support; and two reviewers for providing constructive comments on the manuscript. The authors have no conflicts of interest to disclose. Gastropod and pteropod specimens were sampled and treated in accordance with the ethical standards of Friday Harbor Laboratories, University of Washington.

Part II

Dust and iron in the Indian Ocean

Chapter 5

Quantifying inputs of aerosol dust and lithogenic iron to the Indian Ocean using thorium isotopes

Note: A modified version of this chapter is in preparation as Bausch, A. R., Fleisher, M. Q., Juhl, A. R., Singh, S. K., and R. F. Anderson (in prep). Quantifying inputs of aerosol dust and lithogenic iron to the Indian Ocean using thorium isotopes.

5.1 Abstract

Aerosol dust can deliver essential, limiting micronutrients such as iron (Fe) to surface waters of the ocean. Since inputs of dust to marine ecosystems are difficult to quantify directly, particularly in the Indian Ocean, thorium isotopes (^{232}Th and ^{230}Th) can be used to quantify aerosol dust fluxes and lithogenic Fe supply. In this study, dust fluxes in the western Indian Ocean were quantified using both seawater and core-top sediment samples, which provide different integrated temporal perspectives. Measured dust fluxes generally decreased from north to south with increasing distance from dust source regions. Patterns of dust fluxes were internally consistent between the independent approaches and, furthermore, were in reasonable agreement with regional sediment trap measurements and model-derived fluxes. These dust fluxes may have implications for biological productivity along a north-south gradient in the western Indian Ocean. In addition, seawater measurements were used to estimate residence times of Fe integrated to a particular depth in the Indian Ocean.

Average residence times of dissolved Fe were on the order of 2.5 yr in the upper 1000 m and < 5 months in the upper 200 m. Therefore, Fe inventories integrated over the entire upper 1000 m may not be sensitive to seasonality but surface waters are likely affected by temporal variability of dust deposition in the region. Compared to other ocean basins, the combined biotic and abiotic removal of Fe in the Indian Ocean is slower than that in the North Atlantic but faster than that in the North Pacific. These trends may be driven by increased biological Fe retention in more Fe-limited surface waters and/or decreased abiotic scavenging in regions with lower dust fluxes. Results suggest that dissolved Th can be used as a proxy for both dust and Fe supply in the upper 1000 m of the Indian Ocean. Such findings significantly improve the current understanding of aeolian dust and Fe inputs in the Indian Ocean marine ecosystem.

5.2 Introduction

Inputs of lithogenic trace metals to marine ecosystems can cause profound effects on the growth of marine phytoplankton (e.g., Bausch et al., 2017; Falkowski, 1998; Martin, 1990). The primary source of the trace metal iron (Fe) in surface waters of the ocean is mineral dust deposition (Jickells et al., 2005; Morel and Price, 2003). Dissolved Fe delivered from aeolian dust can impact rates of photosynthesis, respiration, and nitrogen fixation (Falkowski, 1998; Moore et al., 2009; Srinivas and Sarin, 2013), as well as export production and CO_2 uptake (Jickells et al., 2005; Morel and Price, 2003; Tagliabue et al., 2014). Autotrophic organisms utilize Fe in a number of enzymes and electron transfer intermediates involved in photosynthetic growth (Morel and Price, 2003). However, the supply of Fe is so low that it limits phytoplankton growth over an estimated 30-50% of the ocean (Jickells et al., 2005; Moore, 2016; Moore et al., 2002). In addition, co-limitation of Fe and nitrogen is pervasive throughout the surface ocean (Browning et al., 2017). Despite the significant implications of aerosol Fe on ocean biogeochemistry, dust and Fe delivered from dust are not especially well quantified (Hayes et al., 2015b).

It is extremely challenging to directly measure mineral dust fluxes in the open ocean. Although dust concentrations can be measured directly or using tracers (e.g., aluminum;

Al), measurements must be extrapolated to determine fluxes (Jickells et al., 2005, 2016). Therefore, several indirect techniques have been implemented to examine dust deposition in marine ecosystems (Anderson et al., 2016): (1) measurement of lithogenic particles in sediment traps (e.g., Honjo et al., 1999), (2) model estimates (e.g., Mahowald et al., 2005), (3) satellite observations (e.g., Stegmann and Tindale, 1999), and (4) geochemical methods using dust proxies (e.g., Schüßler et al., 2005). One well-established geochemical method uses the thorium (Th) isotopes ^{230}Th and ^{232}Th measured in core-top sediments to calculate detrital fluxes (e.g., Kienast et al., 2016; Pourmand et al., 2004; Rowland et al., 2017). This method makes use of the known ^{230}Th mass budget in the ocean whereby dissolved ^{230}Th, produced at a uniform and known rate throughout the water column by the radioactive decay of dissolved ^{234}U, is scavenged to the sediments by sorption to sinking particles at a rate that is approximately equal to its rate of production. Conversely, ^{232}Th is supplied as a constituent of lithogenic material including aerosol dust (Anderson et al., 2016). Since ^{232}Th is enriched in continental relative to ocean crust (Kienast et al., 2016), ^{232}Th can be used as a tracer of lithogenic material to calculate ^{230}Th-normalized dust fluxes. This method relies on the assumption that ^{232}Th in sediments predominantly come from dust (Hayes et al., 2013; Rowland et al., 2017). Uncertainties for this technique include the concentration of detrital ^{232}Th in dust and the decay of ^{230}Th based on the sediment sample age.

A newer geochemical method to estimate dust fluxes uses dissolved ^{230}Th and ^{232}Th measurements in seawater samples. Since the scavenging rate of Th isotopes by adsorption to particles (yrs to decades; Bacon and Anderson, 1982) is faster than the rates of radioactive decay (^{230}Th half-life = 7.56×10^4 yr, ^{232}Th half-life = 1.41×10^{10} yr; Cheng et al., 2013; Hayes et al., 2015b), Th residence times can be determined using the radioactive disequilibrium of ^{234}U and ^{230}Th. These residence times can then be used to calculate fluxes of dissolved ^{232}Th and ultimately, fluxes of dust (integrated to a particular depth). This method relies on several assumptions: (1) scavenging rates of ^{230}Th and ^{232}Th are equivalent (Hayes et al., 2017); (2) continental material is supplied primarily by the deposition of aeolian mineral dust (Hayes et al., 2015b); and (3) conditions are steady-state for ^{232}Th (i.e., the rate of scavenging and the rate of partial dissolution of continental material are equivalent; Hayes et al., 2013; Huh and Bacon, 1985). Major uncertainties of dissolved

Th-derived dust fluxes include the depth of the water column over which Th inventories and residence times are integrated, as well as the Th solubility and concentration in dust. It is also important to note that this method does not account for any net lateral transport of dissolved Th by advection or diffusion (Anderson et al., 2016).

Since dissolved ^{232}Th cycling is primarily controlled by dust dissolution and scavenging (Hayes et al., 2015b), dissolved ^{232}Th fluxes can also be used as a proxy for aerosol-derived Fe. Dissolved ^{232}Th fluxes together with Fe inventories can be used to calculate Fe fluxes and residence times. This technique relies on the assumption that Fe is supplied primarily by dust deposition (Jickells et al., 2005). Note that loss processes of Fe are not considered in calculating Fe residence times and the assumption of steady-state requires that the total sinks of Fe must equal the total sources (Hayes et al., in revision). Major uncertainties in determining residence times of dissolved Fe include the concentrations and solubilities of Th and of Fe delivered by dust (Hayes et al., in revision). Despite these limitations, Th-derived Fe residence times are essential because current estimates of global Fe residence times are hugely variable, with modeled values ranging from ~5 yr to $>$ 550 yr (Tagliabue et al., 2016).

In this study, we estimated dust fluxes to the northwest Indian Ocean by measuring inventories of dissolved ^{230}Th and ^{232}Th in the water column and by measuring Th concentrations in core-top sediment samples (e.g., Deng et al., 2014; Hayes et al., 2015b; Hsieh et al., 2011). In addition, we estimated fluxes of dissolved Fe (Hayes et al., 2013, 2015b) and approximate Fe residence times (Hayes et al., in revision, 2013, 2015b) in the upper water column. Such information is critical to constrain current estimates of mineral dust fluxes, as well as the biogeochemical cycling of key micronutrients in the ocean. This study is the first to compare Th-derived dust fluxes from seawater and nearby core-top sediment samples in the Indian Ocean. It is also the first study to estimate Th-derived dissolved Fe residence times in the region.

5.3 Materials and methods

5.3.1 Study area

The Indian Ocean is a region of particular interest since it is likely Fe-limited, at least seasonally, according to previous direct measurements (Srinivas and Sarin, 2013), models (Wiggert et al., 2006), and small-scale Fe addition experiments (Moffett et al., 2015). In addition, the northwestern Indian Ocean is located near arid and semiarid climate regions, which are source regions of dust and aerosol Fe (Srinivas and Sarin, 2013; Tindale and Pease, 1999).

The northern Indian Ocean experiences a monsoon climate, driven by the thermal gradient between the Asian continent and the Arabian Sea (Pease et al., 1998; Tindale and Pease, 1999). Predominant surface winds reverse direction seasonally (Shankar et al., 2002; Tomczak and Godfrey, 2001). The summer (i.e., "southwest") monsoon during boreal summer (~May-September) carries moist air from the Arabian Sea toward India via southwesterly winds. Conversely, the winter ("northeast") monsoon during boreal winter (~November-February) is characterized by dry, northeasterly winds.

Predominant wind direction dictates dust transport and deposition in the Indian Ocean. The Arabian Sea region is semi-enclosed by arid and semiarid climates, with deserts in Oman, Saudi Arabia, Yemen, and Somalia to the west, Iran and Pakistan to the north, and India to the east (Pease et al., 1998; Srinivas and Sarin, 2013). Dust transport is highly seasonal: winter dust originates primarily from India, with minor sources from Pakistan, Iran, and Oman (Pease et al., 1998; Srinivas and Sarin, 2013; Tindale and Pease, 1999); summer dust likely originates predominately from Oman, with minor sources from Iran (Pease et al., 1998). Dust deposition in the northern Indian Ocean exhibits significant spatial and temporal variability (Sirocko and Sarnthein, 1989; Srinivas and Sarin, 2013), with particularly high year-round deposition in the northern Arabian Sea near the local source region in Oman (Mahowald et al., 2005; Tindale and Pease, 1999). Dust fluxes determined from Holocene sediments in the Arabian Sea (~100 $\times$ 10^6 t yr^{-1}; Sirocko and Sarnthein, 1989; Sirocko et al., 1991) agree reasonably well with those from modern satellite observations (115-215 $\times$ 10^6 t yr^{-1}; Sirocko and Sarnthein, 1989). Modern dust flux estimates

from models and direct measurements indicate similar dust fluxes in the Indian Ocean (since most of the dust in the Indian Ocean is deposited in the Arabian Sea; 29-154 $\times$ 10^6 t yr^{-1}; Mahowald et al., 2005). Modeled deposition of Fe associated with mineral dust has also been estimated in the Indian Ocean (~1.4 $\times$ 10^6 t yr^{-1}; Zhang et al., 2015). However, since the Fe content in dust is $>$ 1% by weight (Taylor and McLennan, 1995), one (or both) of these modeled estimates in the Indian Ocean may be incorrect.

The major input of continental material in the Arabian Sea includes dust from a variety of source regions (Pease et al., 1998; Srinivas and Sarin, 2013); other sources include river suspensions and sediments (Sirocko et al., 2000). In the western Arabian Sea, Fe inputs are likely aeolian, however in the eastern Arabian Sea off the coast of India, Fe sources include suspensions of river sediments (e.g., from the Indus River) and drainage from the Indian Deccan Traps (Sirocko et al., 2000). River influence is primarily a coastal phenomenon in the Arabian Sea (as shown from patterns of surface salinity; Han and McCreary, 2001; Hood et al., 2017) and likely does not impact the stations in this study.

Monsoon winds also influence the direction of several surface currents, particularly in the northern Indian Ocean (Schott and McCreary, 2001; Shankar et al., 2002; Tomczak and Godfrey, 2001). The Somali Current and the East Arabian Current flow northward (southward) during summer (winter) along the coasts of Somalia and Oman, respectively (Manyilizu et al., 2016; Tomczak and Godfrey, 2001). The West Indian Coastal Current flows southward (northward) along the west coast of India during the summer (winter) monsoon (Tomczak and Godfrey, 2001). These seasonally reversing coastal currents facilitate strong coastal upwelling in summer due to Ekman mass divergence (Tomczak and Godfrey, 2001), and therefore cause strong gradients in biological productivity in surface waters (Qasim, 1977). The Southwest (Northeast) Monsoon Current flows eastward (westward) between the Arabian Sea and the Bay of Bengal during summer (winter) monsoon (Shankar et al., 2002; Tomczak and Godfrey, 2001). During the northeast monsoon, the confluence of the southward-flowing Somali Current and the northward-flowing East African Coastal Current results in the eastward-flowing South Equatorial Counter Current (Manyilizu et al., 2016; Schott and McCreary, 2001). During the intermonsoon periods (April-May and October-November), the equatorial Indian Ocean experiences eastward-flowing surface

jets (Manyilizu et al., 2016; Tomczak and Godfrey, 2001). The circulation of the southern Indian Ocean is dominated by the westward-flowing South Equatorial Current and the counterclockwise subtropical gyre (Tomczak and Godfrey, 2001).

5.3.2 Seawater collection

Seawater samples were collected in the Indian Ocean during two cruises aboard the ORV *Sagar Kanya*: SK312 (May 2014) and SK324 (September-October 2015). Samples were obtained using a standard CTD rosette (Sea-Bird Scientific) with 10-L Niskin bottles (as described by Anand et al., 2018) from the near-surface to a maximum depth of 3700 m at a total of six stations (Figure 5.1). Note that the westernmost station (SK324-13) is near (< 100 km) shallow topography (< 1000 m). Also note that one station (SK312-13) is located near the Carlsberg Ridge and two other stations (SK312-9 and SK312-11) are located near the Central Indian Ridge. In the field, samples were filtered (0.45 μm), stored in acid-cleaned (10% HCl, trace metal grade) low-density polyethylene (LDPE) cubitainers (10 L) or bottles (4 L), and acidified to pH ~2 (6 M HCl, Optima grade).

5.3.3 Dissolved radionuclide analyses

Radionuclide analyses were performed at Lamont-Doherty Earth Observatory (Palisades, NY, USA) in January-May 2017 based on a modified protocol described by Anderson et al. (2012). Each batch of samples included 12-13 seawater samples, 1 intercalibrated working standard, 1 seawater standard, 2 procedural blanks, and 1-2 column blanks. All open samples were handled inside a high-efficiency particulate air (HEPA) laminar flow bench (Envirco 100 Plus). All Teflon tubes and vials were soaked in soap solution for at least 24 h, acid-soaked (8 M HNO_3) at 160°C for 2 d, and rinsed with ultra-pure water (Milli-Q). All reagents were Optima grade. Quality control was tested by intercomparison of the intercalibrated working standard measured over the past seven years. Concentrations measured in this study were within analytical uncertainty, defined by the data scatter (Figure C.1 in the Appendix).

Seawater samples (~4 kg) were transferred to acid-cleaned LDPE cubitainers (5 L; Hedwin Corporation). Samples were further acidified to pH 1.6-1.9 (6 M HCl). Weighed aliquots

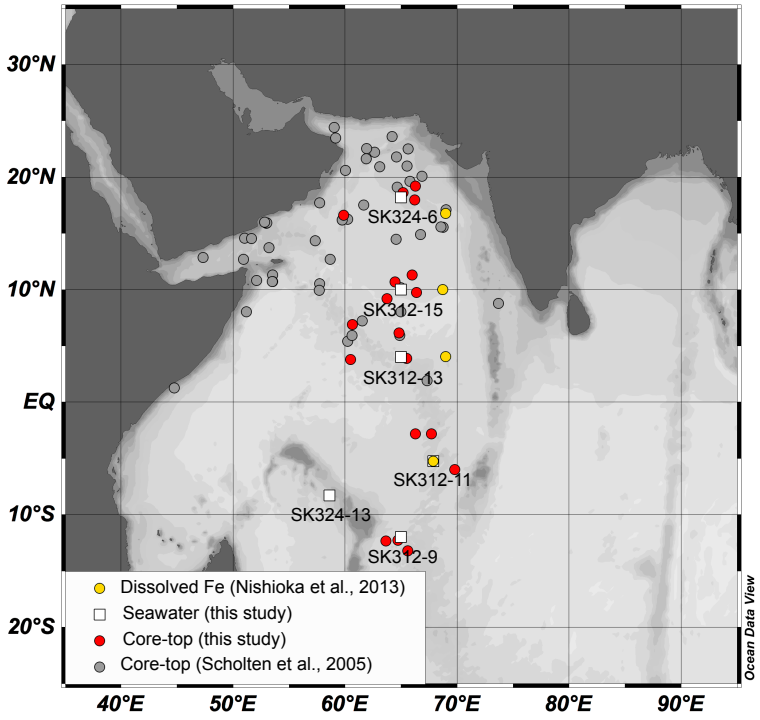

Figure 5.1: Bathymetric map of the study area with station locations of dissolved Fe measurements from Nishioka et al. (2013), seawater and core-top samples from this study, as well as core-top samples from Scholten et al. (2005). Seawater station IDs are included beneath each station location.

of a ^{229}Th spike (~1 pg; 2012-1) and a protactinium isotope (^{233}Pa) spike (100-300 fg; 2016-2b or 2017-1a) and/or a working standard solution of ^{230}Th, ^{232}Th, and ^{231}Pa (2010-1) as described by Anderson et al. (2012), were added to the samples, standards, and procedural blanks. Additionally, purified $FeNO_3$ carrier (30-50 mg mL^{-1} Fe) was added to the samples, standards, and blanks. After allowing the spikes to equilibrate for at least 24 h, concentrated NH_4OH was added to adjust the pH to 8.5-8.7 in order to precipitate $Fe(OH)_3$. Samples were swirled every few hours when possible and the precipitates were allowed to settle for 1-2 d.

After siphoning much of the overlying seawater in the cubitainers to waste, the settled Fe precipitates were transferred to polycarbonate centrifuge bottles (250 mL; Fisher Scientific) for centrifugation (IEC CL30, Thermo Scientific) at 3000 RPM for 27 min. Fe precipitates were then transferred to Teflon centrifuge tubes (50 mL; Savillex) for centrifugation at 3000 RPM for 12 min. All cubitainers and centrifuge bottles were rinsed with dilute NH_4OH to remove major seawater ions and Fe precipitates before transfer to the centrifuge tubes. The supernatant was decanted from the centrifuge tubes and pellets were qualitatively screened using NaI detection to check Pa gamma emission yields. The Fe pellets were then dissolved in concentrated HNO_3 (16 M) and transferred to Teflon vials (15 mL; Savillex). Centrifuge tubes were rinsed with concentrated HNO_3. Concentrated $HClO_4$ was added to the vials, which were heated overnight at 100°C to form a Si crust.

High-temperature digestion was performed in order to remove organic matter and amorphous Si from the precipitates. Samples were heated at 180-210°C to fume $HClO_4$. Concentrated HF was added 2-3 times at high temperature to dissolve the Si crust. Concentrated HNO_3 and $HClO_4$ were added to the vials and heated to fume $HClO_4$. Digested samples were taken up in dilute HCl and transferred back to the centrifuge tubes. Vials were rinsed with Milli-Q water. Concentrated NH_4OH was added to the centrifuge tubes in order to precipitate $Fe(OH)_3$ again. Precipitates were washed with Milli-Q water and centrifuged at 3000 RPM for 12 min. After decanting the supernatant, the Fe pellet was dissolved in concentrated HNO_3 and transferred back to the 15 mL vial. Centrifuge tubes were rinsed with concentrated HNO_3. The seawater standard and column blanks were prepared in con-

centrated HNO_3 in 15 mL vials. All samples (including the seawater standard and column blanks) were heated to dryness at 150-180°C.

Samples were then taken up in concentrated HCl. Polypropylene anion-exchange columns (Bio-Rad Econo-Column) containing 1 mL of Bio-Rad resin (AG1-X8, 100-200 mesh size) and porous polyethylene frits (45 μm) were prepared for initial column separation. Columns were drained and rinsed with a mixed solution of concentrated HCl and HF (0.14 M; to remove Th and Pa from the resin), Milli-Q water (to remove HF), and concentrated HCl (to precondition the columns). Samples were loaded onto the columns, rinsed with concentrated HCl, and drained to Teflon vials (7 mL; Savillex) to collect the unpurified Th fractions. Columns were then rinsed with a mixed solution of concentrated HCl and HF (0.14 M) and drained to new 7 mL vials to elute the unpurified Pa fractions. Vials were capped and analyzed using NaI detection to ensure that Pa did not contaminate the Th fractions. Columns were cleaned using dilute HCl (to remove Fe and U from the resin). Concentrated HNO_3 and $HClO_4$ were added to the vials containing the Th and Pa fractions to remove organic matter eluted from the resin. All vials were heated overnight at 100°C to dry down the Th and Pa column elutions to a drop of $HClO_4$.

The Th fractions were then taken up in HNO_3, while the Pa fractions were taken up in concentrated HCl. Anion-exchange columns were conditioned for the purified Th column by draining the columns filled with dilute HCl and rinsing with HNO_3 (8 M). The Th fractions were loaded onto the columns, and the vials and columns were rinsed with HNO_3 (8 M). After acid-cleaning the Th vials (8 M HNO_3), concentrated HCl was added to the columns to elute the purified Th fractions. Columns were cleaned and reconditioned for the purified Pa column by rinsing with Milli-Q water, a mixed solution of concentrated HCl and HF (0.14 M), Milli-Q water again, and concentrated HCl. The Pa fractions were loaded onto the columns and rinsed with concentrated HCl. After acid-cleaning the Pa vials (8 M HNO_3), a mixed solution of concentrated HCl and HF (0.14 M) was added to the columns to elute the purified Pa fractions. Concentrated HNO_3 and $HClO_4$ were added to the Th and Pa vials, which were heated overnight at 100°C. All samples were dried down to a drop of $HClO_4$ at ~180°C and taken up in run solution (0.16 M HNO_3, 0.028 M HF). Pa vials

were analyzed using NaI detection to determine qualitative recovery. Samples were then transferred to acid-cleaned microcentrifuge tubes and capped.

Concentrations of ^{230}Th, ^{232}Th, and ^{231}Pa were measured using isotope dilution with inductively coupled plasma mass spectrometry (ICP-MS). Note that ^{231}Pa results will be reported in a subsequent paper. Measurements were performed using a Thermo Scientific ELEMENT single collector magnetic-sector ICP-MS (resolving power ~400) fitted with an Aridus desolvating nebulizer (CETAC). Corrections for mass bias, instrument background, and tailing were performed using a natural uranium standard (80-100 pg mL^{-1} U), run solution, and external Th standards, respectively.

5.3.4 Fluxes and residence times from seawater samples

Dust fluxes and Fe residence times were determined using the equations described by Hayes et al. (2017). Briefly, concentrations of excess dissolved ^{230}Th produced by the decay of ^{234}U in seawater (d^{230}Th$_{xs}$) were calculated by correcting measured dissolved ^{230}Th for lithogenic ^{230}Th:

$$d^{230}Th_{xs} = d^{230}Th_{meas} - \frac{d^{232}Th_{meas}}{\left(\frac{^{232}Th}{^{230}Th}\right)_{litho}} \tag{5.1}$$

where the dissolved ^{230}Th$_{meas}$ is ingrowth-corrected using measured salinity (assuming a constant ^{234}U/salinity ratio, as in Owens et al., 2011) and the lithogenic ^{232}Th/^{230}Th atom ratio is 4.00×10^{-6} (Hayes et al., 2015b; Roy-Barman et al., 2009). Residence times of Th (τ_{Th}) were determined using dissolved ^{230}Th$_{xs}$ inventories and production rates of ^{230}Th from ^{234}U decay (β):

$$\tau_{Th} = \frac{\int_0^z d^{230}Th_{xs}\,\mathrm{dz}}{\int_0^z \beta\,\mathrm{dz}} \tag{5.2}$$

where z is the depth of integration and $\beta = 0.0265 \pm 0.0003$ dpm m^{-3} yr^{-1} (salinity = 35.1 ± 0.3; mean ± standard deviation). Dissolved ^{232}Th fluxes – F(d^{232}Th) – were calculated using ^{232}Th inventories and ^{230}Th-derived residence times of Th:

$$F(d^{232}Th) = \frac{\int_0^z d^{232}Th\,\mathrm{dz}}{\tau_{Th}} \tag{5.3}$$

assuming that ^{230}Th and ^{232}Th are scavenged at the same rate. Dust fluxes – F(dust) – were determined using calculated dissolved ^{232}Th fluxes, the fractional Th solubility in dust

(S_{Th}), and the Th concentration in dust:

$$F(dust) = \frac{F(d^{232}Th)}{S_{Th} \times Th_{dust}} \tag{5.4}$$

where the fractional Th solubility is assumed to be 0.1 (as in Hsieh et al., 2011) and the Th concentration in dust is assumed to be 10.7 ppm, the average value in upper continental crust (Taylor and McLennan, 1995). Fe fluxes – F(dFe) – were then calculated using dissolved ^{232}Th fluxes, the relative fractional solubility of Fe and Th, and the average molar Fe/Th ratio in dust:

$$F(dFe) = F(d^{232}Th) \times \left(\frac{S_{Fe}}{S_{Th}}\right) \times \left(\frac{Fe}{Th}\right)_{dust} \tag{5.5}$$

where the relative solubility of Fe and Th is assumed to be 1 (as in Hayes et al., 2015b) and the Fe/Th ratio in dust is assumed to be 1.36×10^4, the ratio in upper continental crust (Taylor and McLennan, 1995). Dissolved Fe concentrations were reported from four nearby stations during cruise ER09 (November-December 2009) aboard the RV *Hakuho-maru* (Figure 5.1; Nishioka et al., 2013). The Fe data from this cruise was also reported by Vu and Sohrin (2013). The detection limit of dissolved Fe was reported to be 0.015 nmol L^{-1}. Note that stations ER09-9 and SK312-11 overlap. Depths were calculated using pressure measurements according to the algorithm described by Saunders and Fofonoff (1976). Residence times of Fe (τ_{Fe}) were calculated using dissolved Fe inventories (determined via trapezoidal integration) and Fe fluxes:

$$\tau_{Fe} = \frac{\int_0^z dFe \, \mathrm{dz}}{F(dFe)} \tag{5.6}$$

where z is the depth over which the residence time is integrated.

5.3.5 Core-top sample collection

Sediment samples from trigger-weight cores were collected from a total of 18 sites occupied during several cruises aboard the RV *Vema* and the USNS *Robert D. Conrad*: VM14 (May 1958), VM19 (August 1963), VM29 (January 1972), VM34 (September-October 1977), RC12 (April 1969), RC17 (May 1974), and RC27 (June 1986; Figure 5.1). The core-top samples were stored at 5°C in the Lamont-Doherty Core Repository (Palisades, NY, USA). All core sediments were assumed to be from the late Holocene (~1000 yr BP). Cores were selected based on proximity to the seawater stations.

5.3.6 Core-top radionuclide analyses

Aliquots of sediments were taken from the upper 4 cm of each core and homogenized using a mortar and pestle. Radionuclide analyses were performed at Lamont-Doherty Earth Observatory in September 2017 based on modified methods detailed in Fleisher and Anderson (2003) and Rowland et al. (2017). Each batch of samples included 18 samples, 1 sediment standard, and 1 procedural blank. All reagents were trace metal grade.

Weighed aliquots of a mixed ^{229}Th-^{236}U spike (150 pg ^{229}Th, 250 pg ^{236}U; 2006-2) and a ^{233}Pa spike (100-300 fg; 2017-2a) were added to homogenized sediment samples (95-100 mg) in 50 mL Teflon beakers. Purified $FeNO_3$ carrier (20-50 mg) and concentrated HNO_3 were added to the beakers and samples were heated at 150°C until almost dry. Concentrated $HClO_4$ was then added and samples were heated at 210°C. Concentrated HF was added two times and samples were heated to fume $HClO_4$. Then, concentrated HNO_3 was added to the beakers and samples were heated again to complete the digestion.

Digested samples were taken up in dilute HCl and transferred to 15 mL centrifuge tubes and centrifuged at ~2000 RPM for 10 min. After decanting the supernatant back into the original 50 mL beakers, the centrifuge tubes were rinsed with Milli-Q water and the solids were discarded. Samples were transferred back to the centrifuge tubes and concentrated NH_4OH was added to precipitate $Fe(OH)_3$ as described above for the seawater samples. Samples were centrifuged two more times for 10 min each and the supernatant was discarded. The Fe pellet was dissolved in concentrated HNO_3 and transferred back to the 50 mL beaker. Centrifuge tubes were rinsed with concentrated HNO_3. Samples were heated to near dryness at 150°C.

Samples were then taken up in concentrated HCl and loaded onto conditioned anion-exchange columns, as described above for the seawater samples. Beakers were rinsed with concentrated HCl. Eluent was drained into 15 mL Teflon vials (Savillex) to collect the unpurified Th fractions. As described for the seawater samples, columns were rinsed with a mixed solution of concentrated HCl and HF (0.14 M) and drained to new 7 mL Teflon vials (Savillex) to elute the unpurified Pa fractions. Dilute HCl (0.12 M) was then added to the columns to collect the U and Fe fractions in the same vials as the unpurified Th fractions.

Samples were analyzed using NaI detection to check for Pa contamination. Concentrated $HClO_4$ was added to the Pa fractions and all samples were dried down overnight at 100°C.

As described above for the seawater samples, the Th fractions were taken up in HNO_3, while the Pa fractions were taken up in concentrated HCl. Columns were conditioned for the purified Th/U column by draining and rinsing with HNO_3 (8 M). The Th/U fractions were loaded onto the columns, and the vials and columns were rinsed with HNO_3 (8 M). After acid-cleaning the 15 mL vials (8 M HNO_3), a mixed solution of HNO_3 and HF (0.16 M HNO_3, 0.028 M HF) was added to the columns to elute Th and U together. Columns were cleaned and reconditioned as described for the seawater samples. The Pa fractions were loaded onto the columns and rinsed with concentrated HCl. The Pa vials and the columns were then cleaned (8 M HNO_3). Purified Pa fractions were eluted with a mixed solution of concentrated HCl and HF (0.14 M). Concentrated $HClO_4$ was added to the Th and Pa vials. Samples were heated overnight at 100°C. All samples were dried down to a drop of $HClO_4$ at ~180°C and taken up in run solution. Concentrations of ^{230}Th, ^{232}Th, ^{234}U, ^{238}U, and ^{231}Pa were measured using ICP-MS as described by Fleisher and Anderson (2003). Note that ^{231}Pa results will be reported in a subsequent paper.

5.3.7 Detrital fluxes

Sediment-derived dust fluxes were determined using the equations detailed in Pourmand et al. (2004) and Rowland et al. (2017). Briefly, concentrations of excess scavenged ^{230}Th ($^{230}Th_{xs}$) were calculated by correcting the measured ^{230}Th for lithogenic ^{230}Th and ^{230}Th produced by the decay of authigenic ^{238}U in sediments:

$$\begin{aligned} {}^{230}Th_{xs} = {}^{230}Th_{meas} - \left({}^{232}Th_{meas} \times \left(\frac{^{238}U}{^{232}Th} \right)_{detritus} \right) - \\ {}^{230}Th_{ingrowth} \times \left({}^{238}U_{meas} - \left({}^{232}Th_{meas} \times \left(\frac{^{238}U}{^{232}Th} \right)_{detritus} \right) \right) \end{aligned} \tag{5.7}$$

where the detrital ^{238}U:^{232}Th activity ratio is 0.7 and the ingrowth of ^{230}Th is 0.01 (calculated assuming a sediment age of 1000 yr, as in Henderson and Anderson, 2003). Initial concentrations of $^{230}Th_{xs}$ in the sediments at the time of deposition ($^{230}Th_{xs,0}$; Pourmand et al., 2004) were calculated:

$$^{230}Th_{xs,0} = {}^{230}Th_{xs} \times e^{(\lambda_{230} \times t)} \tag{5.8}$$

where $\lambda_{230} = 9.15 \times 10^{-6}$ yr^{-1} and t is the approximate sample age (1000 yr). Detrital fluxes – F(detritus) – were calculated using the concentrations of $^{230}\mathrm{Th}_{xs,0}$ and ^{232}Th, as well as the concentration of detrital ^{232}Th:

$$F(detritus) = \left(\frac{\beta \times z}{^{230}Th_{xs,0}}\right) \times \left(\frac{^{232}Th_{meas}}{^{232}Th_{detritus}}\right) \tag{5.9}$$

where z is the depth of the water column, the production flux of ^{230}Th in the overlying water column (β) is assumed to be constant at 0.0263 dpm m^{-3} yr^{-1} (calculated using a seawater ^{234}U concentration of 2868 dpm m^{-3} rather than 2910 dpm m^{-3} as in Francois et al., 2004), and the concentration of ^{232}Th in detritus is 10.7 ppm (the average value in upper continental crust; Taylor and McLennan, 1995).

5.3.8 Other data sources

Several additional data sources were examined to compare various methods to estimate dust fluxes. Dissolved Th-derived dust fluxes from the Atlantic Ocean and Pacific Ocean were calculated using published data for dissolved ^{230}Th and ^{232}Th concentrations assuming a detrital Th concentration of 10.7 ppm and an integration depth of 1000 m. In the Atlantic Ocean, fluxes were determined at a total of 18 stations from cruises KN199-4, KN204-1 (Hayes et al., 2015a), and AE1410 (Hayes et al., 2017). Note that the fluxes from cruise AE1410 in the Caribbean were only integrated to a depth of 500 m. In the Pacific Ocean, dust fluxes were determined at a total of 12 stations from cruises HOT57 (Roy-Barman et al., 1996), KN195-8 (Anderson et al., 2012), SO202-INOPEX (Hayes et al., 2013), KM12-15, KM13-09, and KM13-16 (Hayes et al., 2015b). Detrital fluxes from 51 sites in the Arabian Sea (Figure 5.1; Scholten et al., 2005) and 157 ThoroMap sites in the global ocean (Kienast et al., 2016) were calculated using a constant detrital Th content of 10.7 ppm. Dust fluxes from a state-of-the-art global atmospheric model (Mahowald et al., 2005), as well as from sediment traps in the Indian Ocean (Clemens, 1998; Haake et al., 1993; Honjo et al., 1999) were also examined.

5.3.9 Data analyses

All maps were made using Ocean Data View software (version 4.7.10; Schlitzer, 2015). Depth profiles and scatter plots were made using Prism GraphPad software (version 7). Model data (Mahowald et al., 2005) were analyzed using the R statistical framework (version 3.2.4).

5.4 Results

5.4.1 Seawater samples

Measured dissolved ^{230}Th concentrations increased approximately linearly with depth to an inflection point (~2000 m), and then remained relatively constant with greater depth (Figure 5.2). The percent of the measured total ^{230}Th that was calculated to be of detrital origin was 17.1 ± 11.4 % in the upper 100 m (mean ± standard deviation; values ranging from 4.0 to 48.2 %) and 1.1 ± 0.4 % at depths > 2000 m (values ranging from 0.6 to 2.2 %). Residence times of dissolved Th, calculated using Equation 5.2, increased nearly linearly with integration depth (Figure C.2 in the Appendix).

Dissolved ^{232}Th concentrations were generally constant with depth despite some scatter near the surface (Figure 5.3), with average values of 0.12 ± 0.04 pmol kg^{-1} (mean ± standard deviation; values ranging from 0.04 to 0.3 pmol kg^{-1}). Cumulative dissolved ^{232}Th fluxes increased rapidly with depth from the surface to an inflection point (500-1000 m), then either remained constant or increased more slowly at greater depth (Figure 5.4). Fluxes generally decreased from north to south, with the exception of station SK324-13 (located near shallow bathymetry). At 1000 m, dissolved ^{232}Th fluxes ranged from 13.4 nmol m^{-2} yr^{-1} at the southernmost station (SK312-9) to 46.6 nmol m^{-2} yr^{-1} at the northernmost station (SK324-6).

Dissolved Th-derived dust fluxes calculated using Equation 5.4 and integrated to 1000 m generally decreased from north to south, with the exception of station SK324-13 (Figure 5.5, Table 5.1). Values ranged from 2.9 g m^{-2} yr^{-1} at the southernmost station (SK312-9) to 10.1 g m^{-2} yr^{-1} at the northernmost station (SK324-6). This dust gradient corresponded to a 3-fold change.

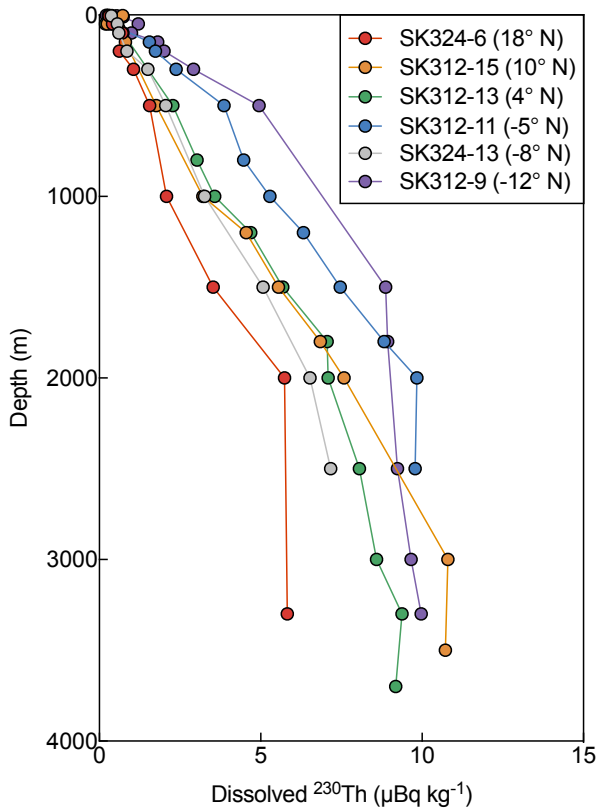

Figure 5.2: Depth profiles of measured dissolved ^{230}Th concentrations (μBq kg^{-1}) in the Indian Ocean. Stations are listed from north to south. Note that the station in grey is located near shallow topography.

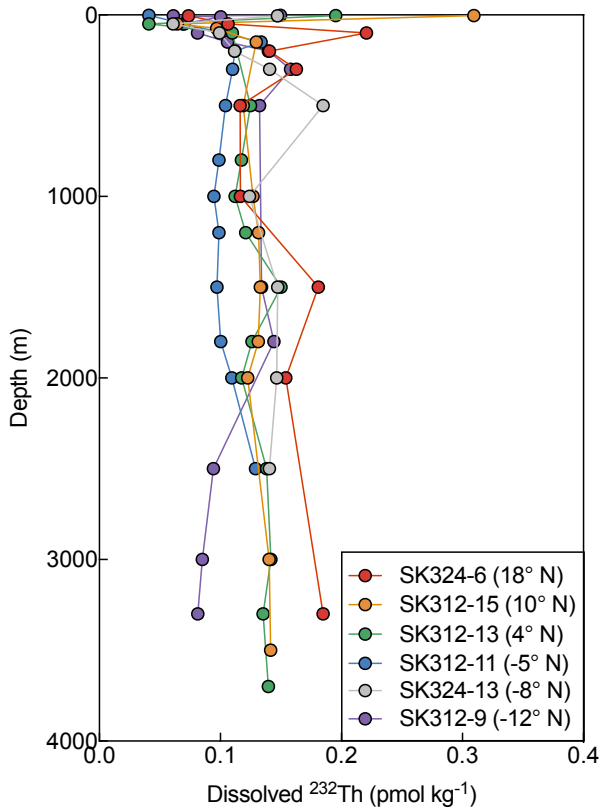

Figure 5.3: Depth profiles of measured dissolved ^{232}Th concentrations (pmol kg^{-1}) in the Indian Ocean. Stations are listed from north to south. Note that the station in grey is located near shallow topography.

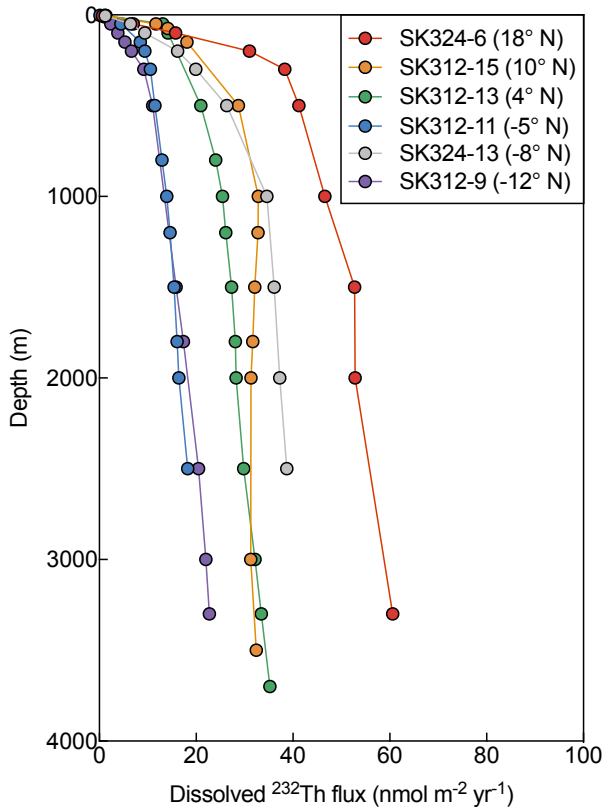

Figure 5.4: Depth profiles of cumulative dissolved ^{232}Th fluxes (nmol m^{-2} yr^{-1}) in the Indian Ocean. Fluxes were calculated using Equation 5.3. Stations are listed from north to south. Note that the station in grey is located near shallow topography.

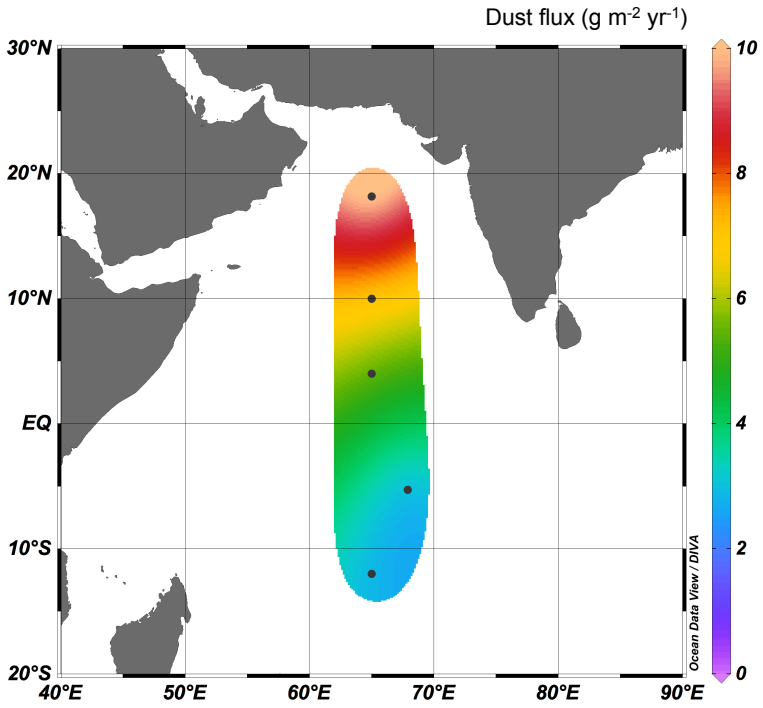

Figure 5.5: Dissolved Th-derived dust fluxes (g m^{-2} yr^{-1}) integrated to 1000 m in the Indian Ocean, assuming 10.7 ppm Th in dust and a solubility of Th in dust of 10%. Note that station SK324-13 is not included here since it is located near shallow topography.

Table 5.1: Dissolved ^{232}Th fluxes (calculated using Equation 5.3), dissolved Fe fluxes (Equation 5.5), dust fluxes (Equation 5.4), and estimated Fe residence times (Equation 5.6) integrated to 1000 m, assuming 10.7 ppm Th in dust. Stations are listed from north to south.

Cruise	Latitude	Longitude	Bottom depth (m)	d^{232}Th flux (nmol m^{-2} yr^{-1})	dFe flux (µmol m^{-2} yr^{-1})	Dust flux (g m^{-2} yr^{-1})	Fe residence time (yr)
SK324-6	18.17	65.00	3400	46.58	633.07	10.10	1.89
SK312-15	10.00	65.00	4543	32.81	445.91	7.11	2.80
SK312-13	4.00	65.00	3800	25.42	345.53	5.51	2.51
SK312-11	-5.27	67.90	3000	13.94	189.50	3.02	2.69
SK324-13*	-8.30	58.63	2650	34.61	470.42	7.51	–
SK312-9	-12.00	65.00	3449	13.42	182.45	2.91	–

* Located near shallow topography

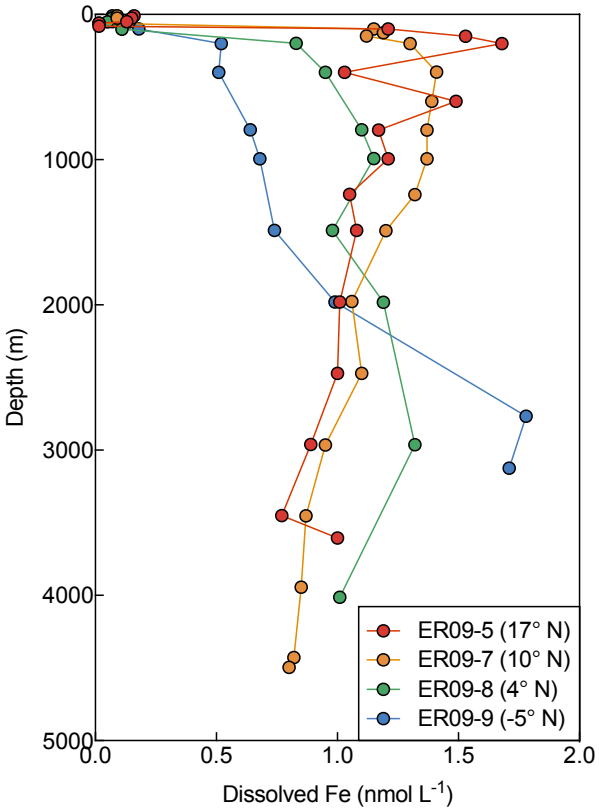

Figure 5.6: Depth profiles of dissolved Fe concentrations (nmol L^{-1}) in the Indian Ocean from Nishioka et al. (2013). Stations are listed from north to south.

Dissolved Fe concentrations (Nishioka et al. 2013) were low near the surface, increased rapidly at ~100 m, and then remained relatively constant with depth (Figure 5.6). One exception was the southernmost station (ER09-9), where Fe concentrations increased with depth below 1000 m. In the upper 1000 m, concentrations generally decreased from north to south. Dissolved Fe fluxes integrated to 1000 m also generally decreased from north to south (Table 5.1). Values ranged from 182 μmol m^{-2} yr^{-1} at the southernmost station (SK312-9) to 633 μmol m^{-2} yr^{-1} at the northernmost station (SK324-6; the station nearest ER09-5). Estimated Fe residence times integrated to 1000 m ranged from 1.9 to 2.8 yr (Table 5.1), with average values of 2.5 $\pm$ 0.4 yr (mean $\pm$ standard deviation). Residence times of dissolved Fe increased approximately linearly with integration depth (Figure C.3 in the Appendix).

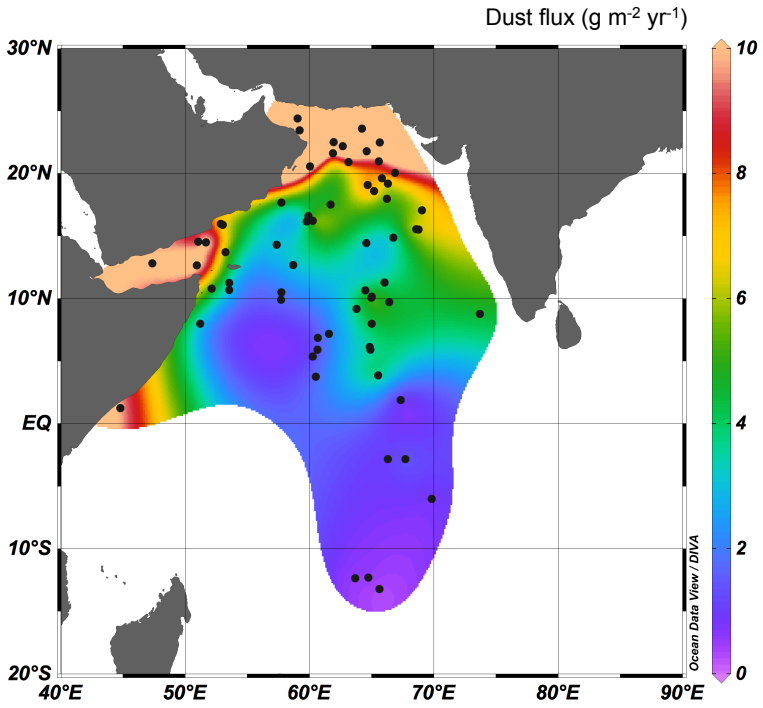

Figure 5.7: Detrital fluxes (g m^{-2} yr^{-1}) from Indian Ocean core-tops from this study combined with those from Scholten et al. (2005), assuming 10.7 ppm Th in dust.

5.4.2 Core-top samples

Detrital fluxes derived from core-top Th examined in this study increased from south to north. Values ranged from 0.3 to 7.9 g m^{-2} yr^{-1}, corresponding to a 28-fold change. Additional detrital fluxes from Scholten et al. (2005) generally decreased from coastal waters to the open ocean. Values ranged from 0.7 to 41.1 g m^{-2} yr^{-1}, but it is important to note that many of these cores were obtained at or near the continental slope. Combined detrital fluxes from this study and detrital fluxes from Scholten et al. (2005) generally decreased from north to south in waters offshore (Figure 5.7).

5.4.3 Model output

Modeled dust fluxes from Mahowald et al. (2005) decreased from north to south with increasing distance from source regions (Figure 5.8) and ranged from 0.2 to 14.7 g m^{-2} yr^{-1}. This dust gradient corresponded to a 98-fold change over the span of our samples.

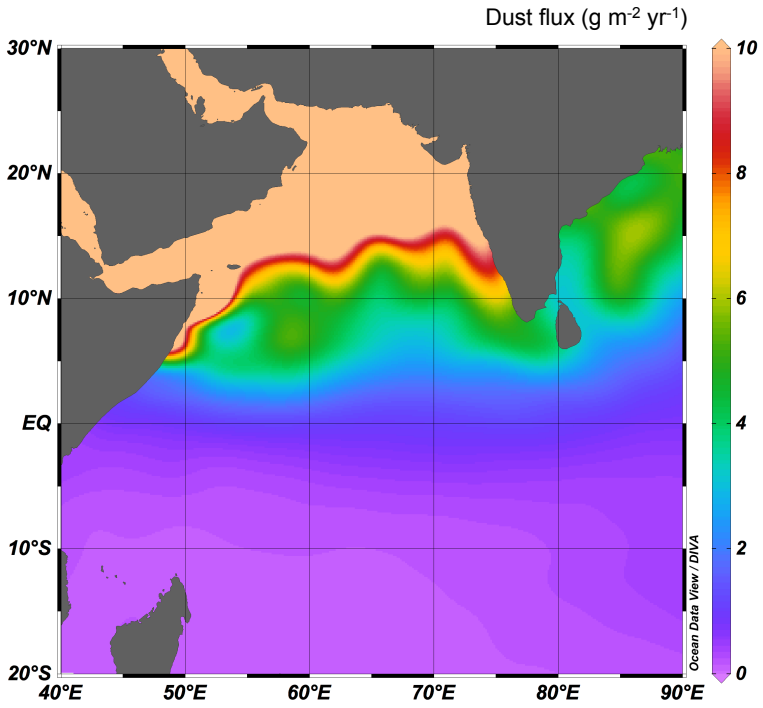

Figure 5.8: Modeled dust deposition (g m^{-2} yr^{-1}) from Mahowald et al. (2005). Note that the color bar scale is the same as that used for measured fluxes to facilitate intercomparison.

The revised version of this model shows the same spatial patterns (Zhang et al., 2015), but these trends were not analyzed here. Modeled dust fluxes were linearly correlated with dissolved Th-derived dust fluxes from this study (R^2 = 0.612, n = 6), core-top derived detrital fluxes from this study (R^2 = 0.691, n = 18), and to a lesser extent, detrital fluxes from Scholten et al. (2005), where many samples were located in shallow sites at or near the continental slope (R^2 = 0.327, n = 51; Figure 5.9, Table C.1, Table C.2, Table C.3 in the Appendix).

5.5 Discussion

5.5.1 Depth profiles of Th

In a theoretical, spatially homogeneous ocean, scavenged nuclides (e.g., Th) undergo continuous, steady-state adsorption and desorption to sinking particles – a process known

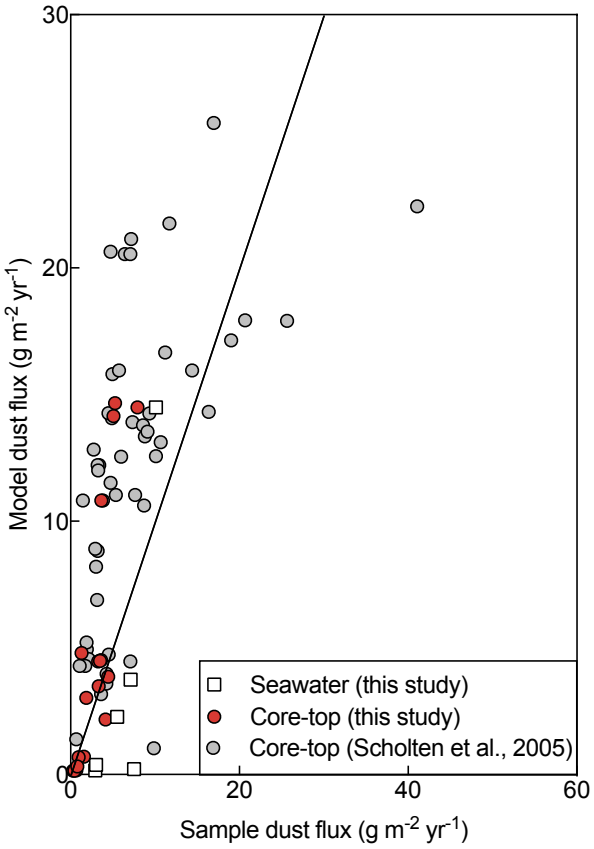

Figure 5.9: Dust fluxes (g m^{-2} yr^{-1}) derived from seawater and core-top samples as a function of model-derived dust fluxes from Mahowald et al. (2005) at the nearest grid boxes.

as reversible scavenging (Bacon and Anderson, 1982). Therefore, profiles of dissolved ^{230}Th and ^{232}Th concentrations are expected to be linear as a function of depth:

$$\frac{\mathrm{d}C}{\mathrm{dz}} = \frac{\beta}{S \times K} \tag{5.10}$$

where $\frac{\mathrm{d}C}{\mathrm{dz}}$ is the slope of the Th concentration as a function of depth, β is the production of ^{230}Th by decay of ^{234}U, S is the particle settling velocity, and K is the partition coefficient for the exchange of Th between solution and solids. The value of K depends on the concentration and composition of settling particles. The product (S $\times$ K) can be thought of as the local scavenging intensity. Thus, according to the principle of reversible scavenging, ^{230}Th concentrations are expected to increase linearly and ^{232}Th concentrations are expected to be uniform with depth since the only source of dissolved ^{232}Th is the dissolution of dust in surface waters and $\beta = 0$ at greater depths (Equation 5.10).

In this study, concentrations of ^{230}Th increased linearly with depth in the upper 1500 m (Figure 5.2), as predicted by reversible scavenging. The slopes of the depth profiles ($R^2 >$ 0.957 for all profiles) varied spatially among stations in a manner consistent with boundary scavenging – the dispersive flux of scavenged nuclides from the ocean interior to continental margins due to enhanced scavenging removal at ocean margins (Bacon, 1988; Hayes et al., 2015a; Roy-Barman, 2009). Concentrations of dissolved ^{230}Th generally decreased near the continental margin, regardless of depth (with the exception of station SK324-13). Spatial gradients in the slope of ^{230}Th suggest enhanced scavenging intensity (S $\times$ K) in the northern Indian Ocean (Equation 5.10), consistent with expectations. Greater biological productivity in the north (e.g., Wiggert et al., 2006) and greater fluxes of lithogenic particles near land (Figure 5.8) would both contribute to greater abundance of particles settling through the water column and, therefore, to greater scavenging intensity. Concentrations of ^{230}Th at station SK324-13 may depart from the overall trend because sediments resuspended from the local topographic high enhance scavenging throughout the nearby water column.

Below 1500 m, concentrations of ^{230}Th deviated from the linearity expected from the simple model of reversible scavenging (Figure 5.2). Possible causes for deviations from linearity include: (1) enhanced scavenging and removal of dissolved ^{230}Th by particles generated from hydrothermal plumes (Hayes et al., 2015a; Pavia et al., in press); (2) nepheloid layers – increased concentrations of particles resuspended from the seafloor, which have

been shown to enhance bottom scavenging (Hayes et al., 2015a); or (3) lateral fluxes via deep circulation of a water mass with lower preformed dissolved ^{230}Th concentrations. If advection of deep water were the primary cause, as has been suggested for the Atlantic Ocean (Luo et al., 2010), deviations from linearity would be expected to occur at the same depth at all stations (assuming water masses occur at approximately the same depths). However, the depth of the onset of nonlinearity observed here ranged from 1500 to 3000 m among our stations. Therefore, circulation is likely less important than hydrothermal plumes or nepheloid layers in determining deep ^{230}Th concentrations in the Indian Ocean.

Concentrations of dissolved ^{232}Th were nearly uniform with depth (Figure 5.3), which is consistent with reversible scavenging (Bacon and Anderson, 1982). It is possible that subsurface ^{232}Th minima (~50 m) coincided with the deep chlorophyll maximum (DCM; 40-90 m; e.g., Breves et al., 2003). Dissolved Fe, characterized by strong scavenging to sinking particles (Moore, 2016), also exhibited minima around the same depth (50-80 m; Nishioka et al., 2013). There does not seem to be a north-south spatial trend in the dissolved ^{232}Th concentrations in the Indian Ocean.

5.5.2 Depth profiles of dissolved Fe

Dissolved Fe concentrations (Nishioka et al., 2013) demonstrated nutrient-like depth profiles with low concentrations in surface waters and minima at depths that likely correspond to the DCM (Figure 5.6). The anomalous increase in dissolved Fe with depth below 2000 m at station ER09-9 may correspond to hydrothermal vent activity on the Central Indian Ridge (Nishioka et al., 2013). The southward decreases in surface Fe concentrations and Fe fluxes are consistent with decreasing proximity to dust source regions.

The slight decrease of dissolved Fe with depth through deep waters at stations ER09-5 and ER09-7 suggests a component of irreversible scavenging of dissolved Fe from deep water. If dissolved Fe were supplied only by dissolution of dust in surface water and completely removed by reversible scavenging, then concentration profiles would be uniform with depth, as observed for dissolved ^{232}Th (Figure 5.3). Given the short residence times for dissolved Fe estimated here (Table 5.1), the advection of deep water masses with lower preformed Fe concentrations into our study area is unlikely to be important, although it cannot be ruled

out entirely. A more likely explanation is that a portion of the dissolved Fe is removed by irreversible scavenging at these stations, for example by formation of oxide coatings on other particles (Frank Pavia, personal communication).

5.5.3 Biotic retention and abiotic scavenging

The finding that dissolved ^{232}Th and Fe exhibited minima around the depth of the DCM may suggest a connection between primary productivity and the removal of these scavenged elements (e.g., export in sinking fecal pellets). However, the processes responsible for removing trace elements and radionuclides at the DCM are not currently understood. Minima in colloidal Fe have been observed at the DCM in the North Atlantic, likely driven by loss of colloids from biological uptake and retention and/or scavenging (Fitzsimmons et al., 2015). Dissolved lithogenic trace elements Al and Ti have been shown to exhibit minima at the DCM in the Atlantic Ocean (Dammshäuser et al., 2013); however, this trend is not caused by removal of colloidal forms of Al and Ti because colloids do not contribute significantly to operationally defined dissolved Al and Ti (Dammshäuser et al., 2013). Minima in ^{232}Th have also been observed at the DCM in the North Pacific (Hayes et al., 2015b).

5.5.4 Fluxes of Th

^{230}Th-normalized dissolved ^{232}Th fluxes (calculated using Equation 5.3) increased dramatically with integration depth (Figure 5.4). This phenomenon of increasing ^{232}Th flux with integration depth is commonly observed but not well understood (Anderson et al., 2016; Hayes et al., 2013; Rowland et al., 2017). Possible explanations include delivery of dissolved ^{230}Th to surface waters by vertical mixing (Hayes et al., 2013), continued dissolution of lithogenic particles as they settle through the thermocline (Anderson et al., 2016), or generation of dissolved ^{232}Th in colloidal form (Hayes et al., 2013).

Spatial patterns of ^{232}Th fluxes (Figure 5.4) indicate a north-south gradient (with the exception of station SK324-13, located near shallow bathymetry). The southward decrease in ^{232}Th flux in the Indian Ocean is likely explained by increasing distance from dust source regions.

5.5.5 Assumptions and uncertainties in dust fluxes

In calculating Th residence times using ^{230}Th concentrations, our assumption that continental material is derived primarily from aeolian dust is likely valid. Schüßler et al. (2005) found that the major source of Al in the Arabian Sea came from atmospheric dust deposition. Other minor sources of ^{232}Th in the Indian Ocean include dissolution of margin sediments, hydrothermal vents, and/or preformed water masses (Hayes et al., in revision). However, inputs of ^{232}Th from hydrothermal vents and performed water masses are likely very minor since hydrothermal activity represents more of a sink than a source of ^{232}Th (e.g., Hayes et al., 2015a) and the residence time of dissolved Th is too short for the advection of preformed Th to be significant. In addition, the hydrothermal vents in the Indian Ocean are much deeper than the integration depth used here.

The decision to integrate ^{230}Th-normalized ^{232}Th fluxes to 1000 m is novel. Some laboratory groups estimate dust fluxes by integrating dissolved Th inventories and residence times to the mixed layer depth (25-250 m; Deng et al., 2014; Hsieh et al., 2011), while others derive fluxes by integrating to 500 m, the depth of maximum subsurface ^{232}Th flux (Hayes et al., 2013, 2015b). We chose to calculate dust fluxes in a manner similar to Hayes et al. (2013, 2015b) by integrating to the point of relatively constant ^{232}Th flux (i.e., where $\frac{\mathrm{d}F(d^{232}Th)}{\mathrm{dz}}$ decreases most rapidly), corresponding to a depth of ~1000 m at our stations. Although this integration depth is deeper than previous studies, it is consistent with the dissolved ^{230}Th and ^{232}Th trends from the Indian Ocean region. In addition, this integration depth accounts for the spatial and temporal variability of mixed layer depths, as well as the dissolution of dust below the mixed layer (Hayes et al., 2013).

In calculating dust fluxes from both seawater and core-top samples, we used an aerosol Th content of 10.7 ppm, the average value in upper continental crust (Taylor and McLennan, 1995), as in Pourmand (2005) and Pourmand et al. (2004, 2007). Dust over the Arabian Sea contains substantial amounts of carbonate (Sirocko et al., 1991), and therefore likely has a lower Th content than the 14 ppm recommended by McGee et al. (2016). However, carbonate would dilute Th and Fe in lithogenic phases to an equal extent, so our methods for estimating fluxes and residence times of dissolved Fe are insensitive to varying carbonate content of dust. Since Th content can change with grain size (McGee et al., 2016), it is

possible that there is a north-south gradient in aerosol Th content in the Arabian Sea due to decreasing average particle size with increasing distance from the source regions (Sirocko and Sarnthein, 1989). However, without grain size data, we had to assume constant Th content.

We also used a fractional Th solubility of 10% as in Hsieh et al. (2011). Previous estimates of dust Th solubility range from 1% to > 30% (e.g., Anderson et al., 2016; Hayes et al., 2013, 2017). We acknowledge the relatively high uncertainty for this estimate (Anderson et al., 2014; Hsieh et al., 2011).

Based on the calculated dissolved Th-derived dust fluxes, it seems logical to either: (1) integrate to 1000 m (the depth of constant ^{232}Th flux, as in Hayes et al., 2013, 2015b) and use a Th solubility of 10% or (2) integrate to 50 m (the mixed layer depth, as in Deng et al., 2014; Hsieh et al., 2011) and use a solubility of 1%. It is possible that both options are valid (i.e., the solubility of Th is 1% at the surface and greater at depth). However, calculated values from seawater samples in this study (using 1000 m depth and 10% solubility) are internally consistent with those from detrital fluxes based on analysis of core-top sediments and modeled fluxes (Figure 5.9, Figure 5.10). Decreasing the integration depth to 50 m would significantly underestimate the calculated dust fluxes; conversely, decreasing the solubility to 1% would increase dust fluxes 10-fold. By both integrating to 50 m depth and assuming 1% solubility, dust fluxes range from 5.1 to 28.4 g m^{-2} yr^{-1} in the study area. However, peak fluxes no longer occur immediately downwind of dust source regions but rather at station SK312-13. It is possible that integrating to 50 m underestimates dust fluxes near continental margins, perhaps due to rapid removal of colloidal ^{232}Th. Alternatively, dust fluxes in the upper 50 m at station SK312-13 may be particularly affected by lateral Th transport in surface waters. The results using 1000 m integration depth with 10% Th solubility yield dust fluxes in better agreement with areal-averaged fluxes from core-top samples and the corresponding fluxes from the model (Figure 5.10).

The internal consistency between our two independent techniques suggests that our approach (i.e., using 1000 m integration depth) and our assumptions (i.e., assuming 10% Th solubility) yield reasonably reliable dust fluxes for seawater samples in the Indian Ocean region. Furthermore, the agreement among dust fluxes using the seawater and core-top

samples, the global atmospheric dust model, and numerous regional observations builds confidence in all methodological approaches. Since it is so difficult to measure dust fluxes directly in marine ecosystems, we must rely on comparisons between independent methods to determine the accuracy of dust flux measurements.

5.5.6 Comparison between seawater and core-top dust fluxes

Both dissolved and core-top Th-derived dust fluxes (calculated using Equation 5.4 and Equation 5.9, respectively) indicated maximum dust deposition in the north, immediately downwind of dust sources (Figure 5.5, Figure 5.7). However, the ~30-fold north-south gradient in the detrital flux estimated from core-top samples (Figure 5.7) was greater than the 3-fold change in the dissolved Th-derived dust flux (Figure 5.5), indicating that mixing of surface waters may homogenize the dust flux signal in the seawater samples (Anderson et al., 2016). Despite the differences in spatial gradients, the two methods yielded dust fluxes in relatively good agreement. Areal averages of detrital fluxes were calculated in 5-degree latitude bands using combined core-tops from this study and core-tops deeper than 2500 m from Scholten et al. (2005). These areal averages ($n \geq 3$) were compared to seawater-derived dust fluxes at stations SK324-6, SK312-15, SK312-13, and SK312-9 (Figure 5.10a). The internal consistency between these independent methods supports the validity of our approaches.

5.5.7 Comparison to modeled dust fluxes

The north-south gradient in modeled dust flux (Mahowald et al., 2005) was nearly 100-fold over the span of our stations (Figure 5.8), far greater than that for the core-top detrital flux or the dissolved Th-derived dust flux from this study. There was strong agreement between the model and our seawater measurements with the exception of one outlier (SK324-13) near shallow bathymetry (Figure 5.9). When we excluded this outlier, the correlation between the model and our seawater measurements improved ($R^2 = 0.8645$, $n = 5$). In general, the dust fluxes integrated to 1000 m agreed with the model at the northern stations but overestimated deposition at the southern stations (Table C.1 in the Appendix). Areal averages of modeled dust fluxes in 5-degree latitude bands at the core-top

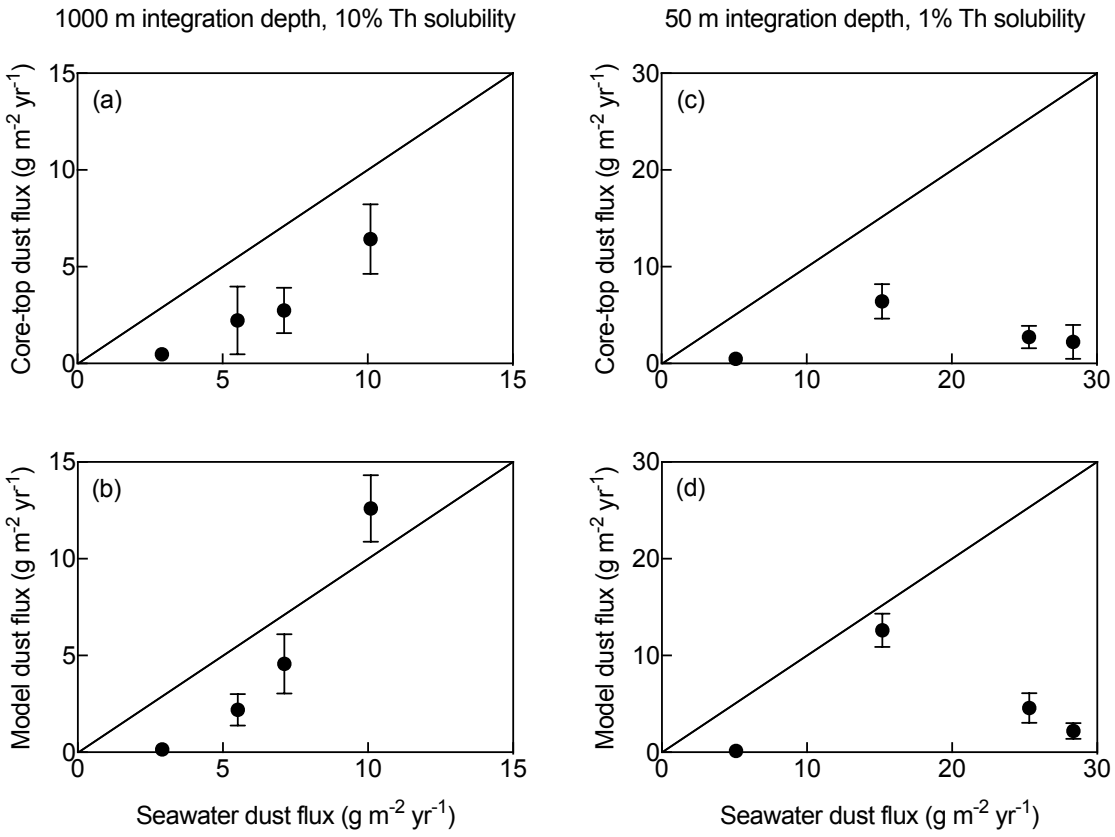

Figure 5.10: Seawater-derived dust fluxes (g m^{-2} yr^{-1}) using 1000 m integration depth and 10% Th solubility compared to areal averages of dust fluxes over 5-degree latitude bands using (a) combined core-tops from this study and core-tops deeper than 2500 m from Scholten et al. (2005) and (b) the model at the nearest grid boxes to the core-top locations (Mahowald et al., 2005). Corresponding fluxes using 50 m integration depth and 1% Th solubility (c and d).

locations in Figure 5.10a show the same trend (Figure 5.10b). These differences may be caused by advective smearing, which has been shown to underestimate dust fluxes in regions of high dust inputs and overestimate fluxes in regions of low deposition (Anderson et al., 2016). However, it is important to note that the uncertainty in modeled dust deposition is greater than a factor of 10 in some regions (Mahowald et al., 2005), so the disagreement in the south between the model and our estimated dust fluxes may reflect uncertainty in the model as well as processes that affect the distribution of dissolved Th.

It is also possible that advective, lateral transport from seasonally reversing surface currents may influence dissolved Th-derived dust fluxes at certain stations. In particular, station SK312-11 in the southern portion of the study area (Figure 5.1) is likely subject to the eastward-flowing South Equatorial Counter Current and surface jets during the northeast monsoon. These currents may carry dissolved ^{232}Th from Africa during winter. Since samples at station SK312-11 were collected during the intermonsoon in May 2014, currents were flowing eastward during the months prior to sampling. Considering the distance between the station and the confluence of the Somali Current and the East African Coastal Current (~2700 km) and the typical velocity of the South Equatorial Counter Current in winter (~0.5 m s^{-1}; Manyilizu et al., 2016), the current could theoretically transport dissolved Th from Africa in ~2 months, far less time than the residence time of Th in the upper 100 m (~1 yr; Figure C.2 in the Appendix). Therefore, dust fluxes calculated from seawater samples at this location may be influenced by the (1) seasonal currents in the study area, (2) timing of sample collection, and (3) current speed, as well as the more generally distributed mixing of dissolved Th from regions of high dust supply to regions of low dust deposition.

There was also a strong correlation between the model and our core-top sediment measurements from this study (Figure 5.9, Table C.2 in the Appendix), as expected for the well-established method to calculate dust fluxes using core-top samples (Kienast et al., 2016). There was a weaker agreement between the model and the core-top samples from Scholten et al. (2005), likely because many of the core sites were located on the continental slope (Figure 5.9, Table C.3 in the Appendix). In regions near the continental slope, ^{230}Th-normalized fluxes of lithogenic material are overestimated due to additional inputs of continental material from rivers and coastal erosion (e.g., McGee et al., 2013). The correla-

tion was particularly poor when fluxes derived from core-top sediments were high (> 10 g m^{-2} yr^{-1}; Figure 5.9), but many of these values corresponded to core-top depths shallower than 2500 m (n = 16). In general, the sediment detrital fluxes underestimated the model at the northern stations and overestimated deposition at the southern stations, but based on the uncertainty of the model, these values were in reasonable agreement (Table C.2, Table C.3 in the Appendix).

5.5.8 Comparison to sediment traps and aerosol samples

Dust fluxes measured here (2.9 to 10.1 g m^{-2} yr^{-1} using seawater samples, 0.3 to 7.9 g m^{-2} yr^{-1} using core-top samples from this study) were generally consistent with sediment trap data in the Arabian Sea region (1.5 to 12.4 g m^{-2} yr^{-1}; Figure 5.11; Clemens, 1998; Haake et al., 1993; Honjo et al., 1999). Spatial patterns of lithogenic fluxes from the sediment traps were also consistent with our findings. Fluxes generally exhibited a north-south gradient, with values that decreased with increasing distance to the coast (i.e., away from dust source regions; Figure 5.11).

In addition, dust fluxes from this study were similar to dust deposition rates in the Arabian Sea based on measurements of Al in the air (0.04-21.9 g m^{-2} yr^{-1}, assuming a settling rate of 1000 m d^{-1}; Tindale and Pease, 1999) or in surface seawater (5.4-16.7 g m^{-2} yr^{-1}; Schüßler et al., 2005). Such comparisons support the validity of our techniques.

5.5.9 Comparison to other ocean basins

Dissolved Th-derived dust fluxes measured in this study were compared to those measured in other parts of the global ocean (Figure 5.12). Compiled global dust fluxes calculated using published dissolved Th data (Anderson et al., 2012; Hayes et al., 2013, 2015a,b, 2017; Roy-Barman et al., 1996) ranged from 1.1 g m^{-2} yr^{-1} in the North Pacific (22.8° N, 158.0° W) to 16.6 g m^{-2} yr^{-1} in the North Atlantic (17.4° N, 18.3° W).

Dust fluxes derived from core-top sediments measured in this study were also compared to those measured in other regions of the world ocean (Figure 5.13). Compiled global ThoroMap dust fluxes from marine sediment cores (Kienast et al., 2016) ranged from 0.1 g m^{-2} yr^{-1} in the equatorial Pacific (1.3° N, 157.3° W) to 14.4 g m^{-2} yr^{-1} in the North

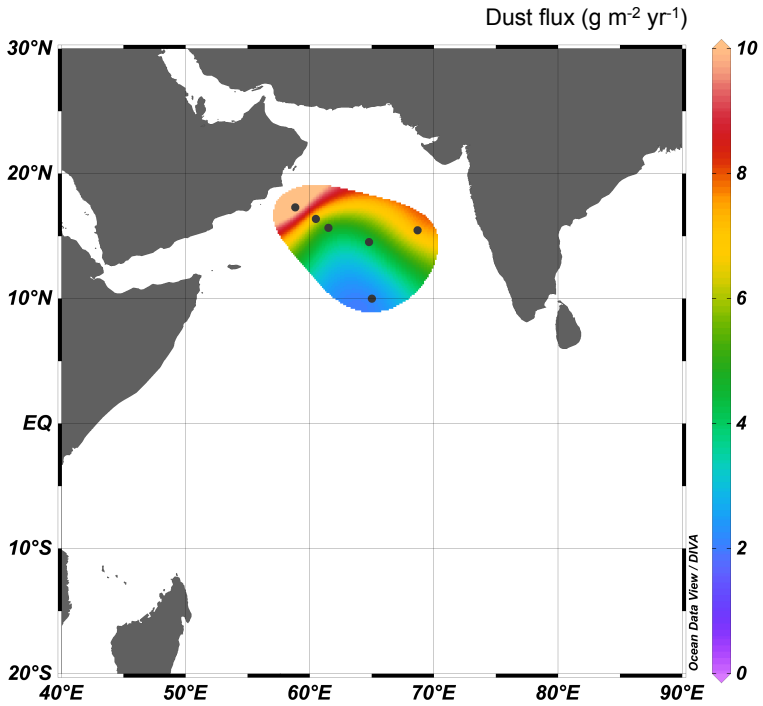

Figure 5.11: Lithogenic fluxes (g m^{-2} yr^{-1}) from Indian Ocean sediment traps from Haake et al. (1993), Clemens (1998), and Honjo et al. (1999). Note that the color bar scale is the same as that used for measured fluxes to facilitate intercomparison.

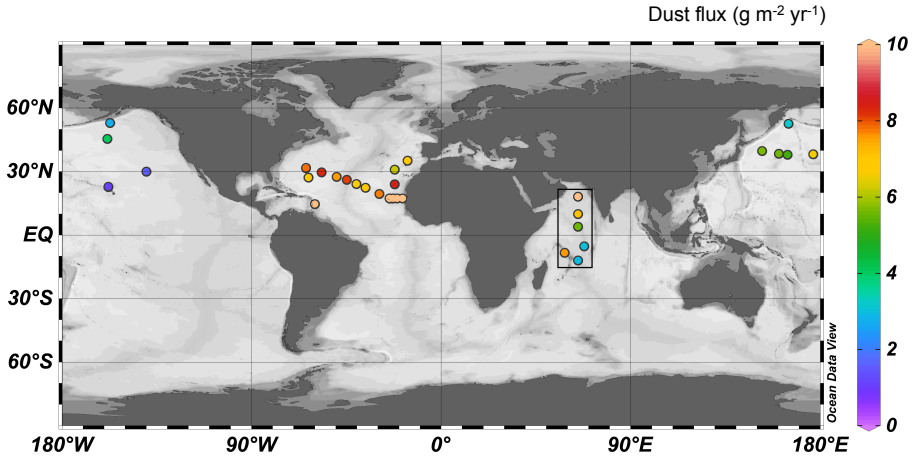

Figure 5.12: Compilation of dissolved Th-derived dust fluxes (g m^{-2} yr^{-1}) from Roy-Barman et al. (1996), Anderson et al. (2012), Hayes et al. (2013, 2015a,b, 2017), and this study, assuming 10.7 ppm Th in dust. All stations are integrated to 1000 m except the Caribbean stations (Hayes et al., 2017), which are only integrated to 500 m. Note that the color bar scale is the same as that used for measured fluxes to facilitate intercomparison. The box indicates the samples measured in this study.

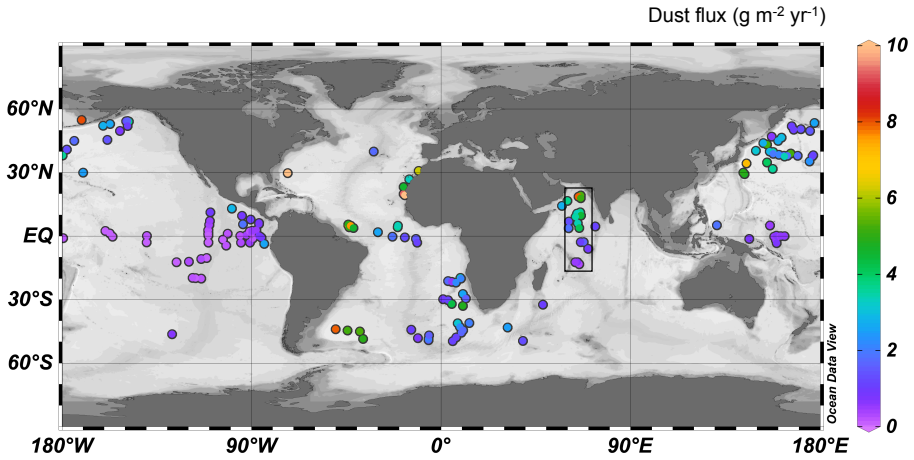

Figure 5.13: Compilation of ThoroMap detrital fluxes (g m^{-2} yr^{-1}) in the late Holocene from Kienast et al. (2016) and from this study, assuming 10.7 ppm Th in dust. Note that the color bar scale is the same as that used for measured fluxes to facilitate intercomparison. The box indicates the samples measured in this study.

Atlantic (19.4° N, 17.3° W). In the western Arabian Sea, the ThoroMap dust flux (2.7 g m^{-2} yr^{-1} at 14.3° N, 57.4° E) was comparable to those measured at the nearest core-tops from this study (3.6 g m^{-2} yr^{-1} at 16.6° N, 59.9° E) and from Scholten et al. (2005; 3.3 g m^{-2} yr^{-1} at 14.3° N, 57.3° E). In the eastern Arabian Sea (4.6° N, 73.2° E), the ThoroMap dust flux was 1.1 g m^{-2} yr^{-1}. However, this site was not near any core-top samples from this study.

In high dust flux regions such as the Atlantic downwind of the Sahara, dissolved Th-derived dust fluxes range from 8.4 to 16.6 g m^{-2} yr^{-1} (Hayes et al., 2015a), with corresponding modeled deposition values ranging from 6.4 to 18.4 g m^{-2} yr^{-1} (Mahowald et al., 2005). In addition, dissolved Th-based dust fluxes from the tropical North Atlantic range from ~1 to 30 g m^{-2} yr^{-1} (acetate leach, 500 m; Anderson et al., 2016). Similarly, core-top sediment-derived dust fluxes in the North Atlantic range from 4.6 to 14.4 g m^{-2} yr^{-1} (Kienast et al., 2016), with modeled dust deposition values ranging from 17.8 to 20.7 g m^{-2} yr^{-1} (Mahowald et al., 2005). In the North Pacific downwind of the Asian deserts, peak sediment-derived dust fluxes range from 4.9 to 7.2 g m^{-2} yr^{-1} (Kienast et al., 2016), with corresponding model outputs that range from 1.0 to 1.5 g m^{-2} yr^{-1} (Mahowald et al., 2005).

However, it is important to note that dust fluxes in the North Pacific exhibit significant spatial variability and uncertainty (Serno et al., 2014).

Indian Ocean dust fluxes measured in this study are far greater than those measured in low dust flux regions of the ocean. In the North Pacific at Station ALOHA, dissolved Th-derived dust fluxes range from 1.1 to 1.6 g m^{-2} yr^{-1} (Anderson et al., 2012; Hayes et al., 2015b; Roy-Barman et al., 1996), with corresponding model outputs of ~0.6 g m^{-2} yr^{-1} (Mahowald et al., 2005). In the equatorial Pacific, detrital fluxes estimated from core-top sediments range from 0.1 to 0.2 g m^{-2} yr^{-1} (Kienast et al., 2016), with modeled deposition values of ~0.1 g m^{-2} yr^{-1} (Mahowald et al., 2005). Other analyses of sediment cores in the equatorial Pacific indicate Holocene dust fluxes of ~0.1 g m^{-2} yr^{-1} (Anderson et al., 2006; Costa et al., 2016; Winckler et al., 2016) up to 0.4 g m^{-2} yr^{-1} (Anderson et al., 2006).

5.5.10 Implications of dust fluxes for biological productivity

The spatial range of dust flux in the modern Indian Ocean measured in this study (2.9-10.1 g m^{-2} yr^{-1} using seawater samples, 0.3-7.9 g m^{-2} yr^{-1} using core-tops) is also comparable to the range of glacial to interglacial dust flux in the Subantarctic South Atlantic downwind of Patagonian dust sources (1-7 g m^{-2} yr^{-1}; Anderson et al., 2014). It is important to note that a smaller range of glacial-interglacial ^{230}Th-derived mass accumulation rates has been measured in the southwest Indian Ocean (Marcantonio et al., 2001). Nonetheless, the range of dust fluxes in the Subantarctic Ocean corresponded to large changes in biological nitrate utilization (Martínez-García et al., 2014). Similarly, enhanced nitrate utilization has been demonstrated in the Subarctic North Pacific during the Last Glacial Maximum (Ren et al., 2015). Although the dust Fe solubility and the biological responses to dust may differ between the Indian Ocean and the Subantarctic South Atlantic Ocean, we speculate that the dust flux gradient in the Indian Ocean could impose a significant source of Fe availability in the northern Indian Ocean and Fe stress in the region south of the equator. In this study, dust fluxes at stations SK324-6, SK312-15, and SK324-13 were all $>$ 7 g m^{-2} yr^{-1}; fluxes at stations SK312-11 and SK312-9 were ~3 g m^{-2} yr^{-1} but nearby core-top samples recorded dust fluxes of $<$ 1 g m^{-2} yr^{-1}. Therefore,

it is possible that stations SK312-11 and SK312-9 do not receive sufficient Fe for complete nitrate utilization.

Although most of the Indian Ocean is thought to be N-limited (Moore, 2016), some regions within the Indian Ocean have been shown to be Fe-limited using natural Fe fertilization studies (Boyd et al., 2007; Moffett et al., 2015). There is also some evidence that parts of the Indian Ocean experience co-limitation of Fe and nitrate (Browning et al., 2017; Takeda et al., 1995). However, to our knowledge, meridional Fe addition experiments in the western Indian Ocean have not been performed to quantify a north-south gradient of Fe-limitation. That said, the ratio of nitrate:Fe has been estimated to be higher in the Indian Ocean south of the equator compared to that north of the equator (Fung et al., 2000), which is consistent with more Fe-replete conditions in the north and more Fe-limited conditions in the south. Dissolved Fe, combined nitrate and nitrite, and phosphate data from Nishioka et al. (2013) indicate some spatial trends in N:Fe and P:Fe ratios in the Indian Ocean. Although these estimated ratios are highly variable in surface waters, values increase from north to south in water depths ranging from 100 to 1000 m (data not shown), suggesting southward increases in Fe stress. These patterns may be consistent with increasing Fe-limitation with increasing distance from dust source regions but additional assessments are required. It is also important to note that the strong oxygen minimum zone (OMZ) in the Arabian Sea impacts both nitrogen and Fe since it is a major sink for nitrate (Moffett et al., 2015) and it affects Fe speciation, Fe-binding ligands, and ultimately, the availability of Fe to phytoplankton (Witter et al., 2000).

5.5.11 Assumptions in residence times of Fe

In calculating dissolved Fe fluxes, we used a Fe/Th ratio of 1.36×10^4 mol/mol, the average Fe/Th content in upper continental crust (Taylor and McLennan, 1995), and a relative fractional solubility of 1:1 since Fe and Th are similarly insoluble in seawater (as in Hayes et al., 2015b). If either of these estimates is too high, the calculated Fe residence times would be underestimated (Hayes et al., in revision). However, the calculation to determine dissolved Fe flux avoids the major difficulty in estimating dust solubilities, since it uses solubility ratios rather than absolute solubilities. By combining Equation 5.3 and

Equation 5.5, it becomes apparent that fluxes of dissolved Fe do not rely on the absolute solubility of either Th or Fe:

$$F(dFe) = \frac{\int_0^z d^{232}Th\,\mathrm{dz}}{\tau_{Th}} \times \left(\frac{S_{Fe}}{S_{Th}}\right) \times \left(\frac{Fe}{Th}\right)_{dust} \tag{5.11}$$

In calculating Fe residence times, we assumed that dust deposition is the major source of Fe. However, if there were other significant sources of Fe (e.g., from anthropogenic aerosols, sediments, or hydrothermal vents), our estimated Fe residence times would be overestimated (Hayes et al., in revision).

5.5.12 Residence times of Fe

The dissolved Fe residence times integrated to 1000 m measured here ranged from 1.9 to 2.8 yr (2.5 ± 0.4 yr; mean ± standard deviation; Table 5.1, Figure C.3 in the Appendix). It is important to note that these Fe residence times reflect the Fe inventory in the entire upper 1000 m; significant uptake and regeneration of Fe occur above this integration depth. Also note that Fe residence times increase with depth due to remineralization and lateral transport of Fe (Hayes et al., 2015b), but also simply due to the increase of dissolved Fe inventory with depth. The residence times measured here are within the range of other similarly calculated values using the Th supply-based approach at 1000 m integration depth. In the North Pacific at Station ALOHA, residence times in the upper 1000 m have been shown to be ~6-7 yr (Hayes et al., 2015b). In the subtropical North Atlantic, residence times have been determined to be ~0.7-1.5 yr in the upper 1000 m (Hayes et al., in revision).

These findings indicate that the removal of Fe in the upper 1000 m of the Indian Ocean is faster than that in the North Pacific and slightly slower than that in the North Atlantic. Mechanisms impacting Fe residence times include (1) biological recycling of Fe (i.e., increased retention of Fe in ligands and living cells) and/or (2) abiotic scavenging. It is possible that biological Fe recycling is enhanced in the Pacific, where surface waters are Fe-limited, compared to the Atlantic. It has been demonstrated that Fe is retained more efficiently in the equatorial Pacific compared to a California coastal upwelling region (Hutchins et al., 1993). In addition, in the equatorial Pacific Ocean, Fe is recycled and presumably retained in surface waters more efficiently than nitrogen (Rafter et al., 2017). Interestingly,

microbes may be capable of producing stronger Fe-binding ligands in Fe-deficient waters compared to Fe-replete coastal waters (Boiteau et al., 2016). Therefore, it is possible that ligands and/or living microorganisms in surface waters of the Indian Ocean may retain Fe more strongly than those in the North Atlantic. There is some evidence of relatively high total ligand concentrations in the Arabian Sea (Witter et al., 2000). It is also possible, however, that abiotic processes remove Fe faster in the Atlantic and the Indian Ocean, where high dust fluxes increase scavenging intensity, and slower in the Pacific. Intermediate residence times in the Indian Ocean are consistent with both intermediate dust inputs relative to the North Pacific and North Atlantic (Figure 5.12, Figure 5.13) and seasonal Fe-limitation (e.g., Wiggert et al., 2006). Additional studies are required to disentangle the influence of biotic and abiotic factors (e.g., by comparing P:Fe ratios in living cells and in sinking particles from the thermocline and quantifying abiotic removal of Fe).

In surface waters, residence times of dissolved Fe in the upper 200 m in our study area ranged from 3.0 to 6.7 months (4.7 ± 1.5 months; mean ± standard deviation; Figure C.3 in the Appendix). Such short residence times indicate that dissolved Fe concentrations are likely sensitive to seasonal dust inputs (Hayes et al., 2015b). These residence times are comparable to similarly calculated values in other regions of the world ocean. Using the Th-based approach in the North Pacific, Fe residence times have been shown to be ~6-12 months in the upper 250 m (Hayes et al., 2015b). Using the same approach in the North Atlantic, Fe residence times have been calculated to be ~0.5 months in the upper 50-200 m near the Caribbean (Hayes et al., 2017) and ~1-2 months in the upper 300 m of the subtropical North Atlantic. These comparisons are consistent with either increased biotic Fe retention in the Indian Ocean compared to the North Atlantic (especially in light of strong biological Fe uptake in the DCM compared to relatively weaker Th drawdown at approximately the same depths in this study; Figure 5.3, Figure 5.6) and/or decreased abiotic Fe scavenging in the Indian Ocean compared to the Atlantic Ocean.

5.5.13 Conclusions

This study used Th isotopes measured in seawater and nearby core-top sediment samples to quantify inputs of dust and residence times of dust-supplied dissolved Fe in the Indian

Ocean. The Th-derived dust fluxes from seawater and corresponding core-top sediment samples measured here suggest that Th can be used as a proxy for dust in the Indian Ocean. Both the seawater and core-top methods generally recorded a dust signal of decreasing lithogenic input from north to south with increasing distance from dust source regions. The degree of agreement among the two methods, a global atmospheric model (Mahowald et al., 2005), and sediment trap measurements (Clemens, 1998; Haake et al., 1993; Honjo et al., 1999) is encouraging, especially considering the vastly different timescales for the seawater and core-top techniques (i.e., several yr in the water column, 1000 yr in the sediments; Hayes et al., 2013). Findings lend confidence to the dissolved Th-based approach to calculate dust fluxes using an integration depth of 1000 m and a Th solubility of 10%. Increased numbers of field measurements in the Indian Ocean are crucial to improve the current understanding of aeolian dust in the region (Mahowald et al., 2005; Stegmann and Tindale, 1999). In particular, measurements of dust fluxes, as well as Th and Fe solubilities and concentrations in the Indian Ocean are essential to reduce the uncertainties of the techniques used in this study. Residence times of dissolved Fe of ~4.7 months in the upper 200 m indicate that temporal variability in surface Fe concentrations may follow the seasonal pattern of dust deposition in the region. Dissolved Fe residence times of ~2.5 yr integrated in the upper 1000 m suggest that combined rates of biological removal and abiotic scavenging of Fe in the Indian Ocean fall between those in the North Pacific and the North Atlantic where similar methods have been applied. These findings significantly improve estimates of the supply of lithogenic trace elements in highly productive waters of the Indian Ocean, including the seasonally-limiting micronutrient Fe, and may be used to better predict regional models of dust and aerosol Fe supply. In addition, these research findings may help inform thresholds of Fe-limited biological productivity.

5.6 Acknowledgements

The authors would like to thank the captain and crew aboard the ORV *Sagar Kanya* for collecting the seawater samples; Nichole Anest and Clara Chang for their assistance in the Lamont Core Repository; Jan Scholten for sending a digital copy of his data; and Sebastian

Vivancos and Frank Pavia for their guidance in analyzing data. This work was supported by in part by the NSF-OCE (grant 1233688) and the Columbia University Department of Earth and Environmental Sciences. The authors declare no conflicts of interest.

Part III

Concluding material

Chapter 6

Dissertation summary

This dissertation used multiple, diverse approaches to examine coupled chemical and biological responses to environmental change. Controlled incubation experiments using plankton from culture collections and from the field, as well as trace metal clean laboratory assessments were used to answer two simple but fundamental questions: (1) how do marine planktonic organisms respond to ocean acidification in combination with other co-occurring stressors associated with climate change such as intensified hypoxia, increased lithogenic trace metal inputs, and changing bacterial activity and (2) what are the spatial patterns of potentially interacting drivers such as aerosol iron delivered from dust?

In Part I of this dissertation, Chapter 2 assessed the impacts of simulated hypoxia and acidification on the growth of the harmful dinoflagellate *Amphidinium carterae* both individually and in combination. Major research questions were twofold: (1) is there a synergetic interaction between high CO_2 and low O_2 on the growth and physiology of *A. carterae* and (2) if so, what is the mechanism driving the synergy? Results included (1) an unexpected, strong synergistic interaction between CO_2 and O_2, indicating *in vitro* RuBisCO specificity may not always predict *in vivo* organismal responses to CO_2 and O_2 conditions and (2) the photosynthetic imbalance in *A. carterae* cells under combined acidification and hypoxia conditions is consistent with a photosynthetic impedance mismatch under nonphotorespiratory conditions. This is the first study to simulate hypoxia, ocean acidification, and coastal acidification to examine synergistic effects on the growth, metabolism, and photophysiology of

a phytoplankton species. The findings from this study significantly improve understanding of the effects of multi-stressors including acidification and hypoxia in coastal ecosystems.

Chapter 3 examined the combined effects of ocean acidification conditions and high suspended sediment loads on the growth of another harmful dinoflagellate, *Cochlodinium polykrikoides*. The scientific questions addressed here were threefold: (1) how do dissolved trace metal concentrations delivered from sediments change under high CO_2; (2) what is the physiological response of *C. polykrikoides* to high suspended sediments under elevated CO_2; and (3) what are the toxicity responses of *C. polykrikoides* to cadmium and nickel? Major research findings included (1) increased dissolved iron and nickel concentrations from suspended sediments at high CO_2; (2) decreased *C. polykrikoides* growth rates following sediment additions at high CO_2, likely predominantly driven by nickel toxicity; and (3) dose-dependent toxicity responses of *C. polykrikoides* to both cadmium and nickel. This is the first study to examine the combined effects of high CO_2 concentrations and high trace metal concentrations mobilized from sediments on the growth of marine phytoplankton. Such information is required to better understand the biogeochemical changes associated with synergistic anthropogenic ocean acidification and trace metal inputs in coastal marine ecosystems.

Chapter 4 examined the combined influence of bacteria and ocean acidification on the severity and extent of dissolution in the shells of larval gastropods and the adult pteropod *Limacina helicina*. The scientific questions discussed here were as follows: (1) how does aragonite saturation state (Ω_{arag}) influence shell dissolution among gastropod larvae and adult *L. helicina* and (2) how do bacteria influence shell dissolution under a range of Ω_{arag}? Major findings included (1) increased shell dissolution with decreasing Ω_{arag} among both gastropod larvae and adult pteropods and (2) microbial mediation of certain types of dissolution among larval gastropods under low Ω_{arag}. This is the first study to examine the role of bacteria in shell dissolution in either larval gastropods or adult *L. helicina* pteropods. This information is essential to better predict the threats of anthropogenic OA on sensitive bioindicators such as marine molluscs.

In Part II of this dissertation, Chapter 5 used Th isotopes in seawater and core-top sediment samples to quantify aerosol dust and dissolved Fe supplied from dust in the Indian

Ocean. Research questions were twofold: (1) what are the spatial patterns of dust fluxes in the northwest Indian Ocean and (2) what are the residence times of Fe in the upper 1000 m? Major results included (1) estimates for thresholds of Fe-limitation as a result of aeolian dust deposition and (2) residence times averaged over the upper 1000 m on the order of 2.5 years, indicating intermediate rates of Fe biological retention and abiotic scavenging compared to those in the North Pacific and the North Atlantic. This study is the first to quantify Th-derived dust fluxes from both seawater and sediment samples and Th-based Fe residence times in the Indian Ocean. Such information is required to better constrain the supply of lithogenic Fe and the impacts of this driver on biological productivity in the region.

These studies together significantly improve our fundamental, mechanistic understanding of co-occurring stressors associated with climate change. Ultimately, the findings from this dissertation may inform model predictions of anthropogenic impacts in ecologically and economically important marine food webs and provide crucial insights to decision-makers.

Bibliography

Al Azri, A. R. et al. (2014). Mesoscale and nutrient conditions associated with the massive 2008 *Cochlodinium polykrikoides* bloom in the Sea of Oman/Arabian Gulf. *Estuaries and Coasts* 37(2):325–338. DOI: 10.1007/s12237-013-9693-1.

Al Gheilani, H. M. et al. (2011). Fish kill incidents and harmful algal blooms in Omani waters. *Agricultural and Marine Sciences* 16:23–33. DOI: 10.24200/jams.vol16iss0pp23-33.

Al Yamani, F. (2008). Importance of the freshwater influx from the Shatt al-Arab River on the Gulf marine environment. In: *Protecting the Gulf's Marine Ecosystems from Pollution*. Ed. by A. H. Abuzinada et al. Basel: Birkhäuser Verlag, pp. 207–222.

Anand, S. S. et al. (2018). POC export fluxes in the Arabian Sea and the Bay of Bengal: A simultaneous ^{234}Th/^{238}U and ^{210}Po/^{210}Pb study. *Marine Chemistry* 198:70–87. DOI: 10.1016/j.marchem.2017.11.005.

Anderson, R. F. et al. (2006). Glacial-interglacial variability in the delivery of dust to the central equatorial Pacific Ocean. *Earth and Planetary Science Letters* 242(3-4):406–414. DOI: 10.1016/j.epsl.2005.11.061.

Anderson, R. F. et al. (2012). GEOTRACES intercalibration of ^{230}Th, ^{232}Th, ^{231}Pa, and prospects for ^{10}Be. *Limnology and Oceanography: Methods* 10(4):179–213. DOI: 10.4319/lom.2012.10.179.

Anderson, R. F. et al. (2014). Biological response to millennial variability of dust and nutrient supply in the Subantarctic South Atlantic Ocean. *Philosophical Transactions of the Royal Society A: Mathematical, Physical and Engineering Sciences* 372(2019):1–17. DOI: 10.1098/rsta.2013.0054.

Anderson, R. F. et al. (2016). How well can we quantify dust deposition to the ocean? *Philosophical Transactions of the Royal Society A: Mathematical, Physical and Engineering Sciences* 374(2081):1–26. DOI: 10.1098/rsta.2015.0285.

Atkinson, C. A. et al. (2007). Effect of overlying water pH, dissolved oxygen, salinity and sediment disturbances on metal release and sequestration from metal contaminated marine sediments. *Chemosphere* 69(9):1428–1437. DOI: 10.1016/j.chemosphere.2007.04.068.

Azcón-Bieto, J. et al. (1994). Acclimation of respiratory O_2 uptake in green tissues of field-grown native species after long-term exposure to elevated atmospheric CO_2. *Plant Physiology* 106(3):1163–1168. DOI: 10.1104/pp.106.3.1163.

Baars, O. and P. L. Croot (2015). Dissolved cobalt speciation and reactivity in the eastern tropical North Atlantic. *Marine Chemistry* 173:310–319. DOI: 10.1016/j.marchem.2014.10.006.

Bacon, M. P. (1988). Tracers of chemical scavenging in the ocean: Boundary effects and large-scale chemical fractionation. *Philosophical Transactions of the Royal Society A: Mathematical, Physical and Engineering Sciences* 325(1583):147–160. DOI: 10.1098/rsta.1988.0048.

Bacon, M. P. and R. F. Anderson (1982). Distribution of thorium isotopes between dissolved and particulate forms in the deep sea. *Journal of Geophysical Research* 87(C3):2045=2056. DOI: 10.1029/JC087iC03p02045.

Badger, M. R. et al. (1998). The diversity and coevolution of RuBisCO, plastids, pyrenoids, and chloroplast-based CO_2-concentrating mechanisms in algae. *Canadian Journal of Botany* 76(6):1052–1071. DOI: 10.1139/cjb-76-6-1052.

Bagby, S. C. and S. W. Chisholm (2015). Response of *Prochlorococcus* to varying CO_2:O_2 ratios. *ISME Journal* 9(10):2232–2245. DOI: 10.1038/ismej.2015.36.

Baumann, H. (2016). Combined effects of ocean acidification, warming, and hypoxia on marine organisms. *Limnology and Oceanography e-Lectures* 6(1):1–43. DOI: 10.1002/loe2.10002.

Bausch, A. R. et al. (2017). Elevated toxic effect of sediments on growth of the harmful dinoflagellate *Cochlodinium polykrikoides* under high CO_2. *Aquatic Microbial Ecology* 80(2):139–152. DOI: 10.3354/ame01848.

Bauwe, H. et al. (2010). Photorespiration: Players, partners and origin. *Trends in Plant Science* 15(6):330–336. DOI: 10.1016/j.tplants.2010.03.006.

Bauwe, H. et al. (2012). Photorespiration has a dual origin and manifold links to central metabolism. *Current Opinion in Plant Biology* 15(3):269–275. DOI: 10.1016/j.pbi.2012.01.008.

Bednaršek, N. et al. (2012a). Description and quantification of pteropod shell dissolution: A sensitive bioindicator of ocean acidification. *Global Change Biology* 18(7):2378–2388. DOI: 10.1111/j.1365-2486.2012.02668.x.

Bednaršek, N. et al. (2012b). Extensive dissolution of live pteropods in the Southern Ocean. *Nature Geoscience* 5(12):881–885. DOI: 10.1038/ngeo1635.

Bednaršek, N. et al. (2014a). Dissolution dominating calcification process in polar pteropods close to the point of aragonite undersaturation. *PLoS ONE* 9(10):1–14. DOI: 10.1371/journal.pone.0109183.

Bednaršek, N. et al. (2014b). *Limacina helicina* shell dissolution as an indicator of declining habitat suitability owing to ocean acidification in the California Current Ecosystem. *Proceedings of the Royal Society B: Biological Sciences* 281(1785):1–8. DOI: 10.1098/rspb.2014.0123.

Bednaršek, N. et al. (2016). Comment on Peck et al. Vulnerability of pteropod (*Limacina helicina*) to ocean acidification: Shell dissolution occurs despite an intact organic layer. *Deep Sea Research Part II: Topical Studies in Oceanography* 127:53–56. DOI: 10.1016/j.dsr2.2016.03.006.

Berner, R. A. and S. Honjo (1981). Pelagic sedimentation of aragonite: Its geochemical significance. *Science* 211(4485):940–942. DOI: 10.1126/science.211.4485.940.

Biller, D. V. and K. W. Bruland (2012). Analysis of Mn, Fe, Co, Ni, Cu, Zn, Cd, and Pb in seawater using the Nobias-chelate PA1 resin and magnetic sector inductively coupled plasma mass spectrometry (ICP-MS). *Marine Chemistry* 130-131:12–20. DOI: 10.1016/j.marchem.2011.12.001.

Birmingham, B. C. et al. (1982). Measurement of photorespiration in algae. *Plant Physiology* 69(1):259–262. DOI: 10.1104/pp.69.1.259.

Biswas, H. et al. (2015). Response of a natural phytoplankton community from the Qingdao coast (Yellow Sea, China) to variable CO_2 levels over a short-term incubation experiment. *Current Science* 108(10):1901–1909.

Boisvert, S. et al. (2007). Inhibition of the oxygen-evolving complex of photosystem II and depletion of extrinsic polypeptides by nickel. *Biometals* 20(6):879–889. DOI: 10.1007/s10534-007-9081-z.

Boiteau, R. M. et al. (2016). Siderophore-based microbial adaptations to iron scarcity across the eastern Pacific Ocean. *Proceedings of the National Academy of Sciences* 113(50):14237–14242. DOI: 10.1073/pnas.1608594113.

Bowes, G. et al. (1971). Phosphoglycolate production catalyzed by ribulose diphosphate carboxylase. *Biochemical and Biophysical Research Communications* 45(3):716–722. DOI: 10.1016/0006-291X(71)90475-X.

Boyd, P. W. and D. A. Hutchins (2012). Understanding the responses of ocean biota to a complex matrix of cumulative anthropogenic change. *Marine Ecology Progress Series* 470:125–135. DOI: 10.3354/meps10121.

Boyd, P. W. et al. (2007). Mesoscale iron enrichment experiments 1993-2005: Synthesis and future directions. *Science* 315(5812):612–617. DOI: 10.1126/science.1131669.

Brand, L. E. et al. (1986). Reduction of marine phytoplankton reproduction rates by copper and cadmium. *Journal of Experimental Marine Biology and Ecology* 96(3):225–250. DOI: 10.1016/0022-0981(86)90205-4.

Breitberg, D. et al. (2015). And on top of all that... Coping with ocean acidification in the midst of many stressors. *Oceanography* 25(2):48–61. DOI: 10.5670/oceanog.2015.31.

Breitburg, D. et al. (2018). Declining oxygen in the global ocean and coastal waters. *Science* 359(6371):1–11. DOI: 10.1126/science.aam7240.

Breves, W. et al. (2003). Fluorophores in the Arabian Sea and their relationship to hydrographic conditions. *Ocean Dynamics* 53(2):73–85. DOI: 10.1007/s10236-003-0025-z.

Brooks, M. D. and K. K. Niyogi (2011). Use of a pulse-amplitude modulated chlorophyll fluorometer to study the efficiency of photosynthesis in *Arabidopsis* plants. In: *Chloroplast Research in Arabidopsis: Methods and Protocols*. Ed. by R. P. Jarvis. New York: Springer, pp. 299–310.

Browning, T. J. et al. (2017). Nutrient co-limitation at the boundary of an oceanic gyre. *Nature* 551(7679):242–246. DOI: 10.1038/nature24063.

Brunton, L. L. et al. (2011). *Goodman and Gilman's The Pharmacological Basis of Therapeutics*. 12th ed. New York: McGraw-Hill.

Bunt, J. S. (1971). Levels of dissolved oxygen and carbon fixation by marine microalgae. *Limnology and Oceanography* 16(3):564–566. DOI: 10.4319/lo.1971.16.3.0564.

Burns, B. D. and J. Beardall (1987). Utilization of inorganic carbon by marine microalgae. *Journal of Experimental Marine Biology and Ecology* 107(1):75–86. DOI: 10.1016/0022-0981(87)90125-0.

Busch, D. S. et al. (2014). Shell condition and survival of Puget Sound pteropods are impaired by ocean acidification conditions. *PLoS ONE* 9(8):1–12. DOI: 10.1371/journal.pone.0105884.

Cai, W.-J. et al. (2011). Acidification of subsurface coastal waters enhanced by eutrophication. *Nature Geoscience* 4(11):766–770. DOI: 10.1038/ngeo1297.

Caldeira, K. and M. E. Wickett (2003). Anthropogenic carbon and ocean pH. *Nature* 425(6956):365. DOI: 10.1038/425365a.

Caldeira, K. and M. E. Wickett (2005). Ocean model predictions of chemistry changes from carbon dioxide emissions to the atmosphere and ocean. *Journal of Geophysical Research* 110:1–12. DOI: 10.1029/2004JC002671.

Cao, C. et al. (2011). Effects of manganese on the growth, photosystem II and SOD activity of the dinoflagellate *Amphidinium* sp. *Journal of Applied Phycology* 23(6):1039–1043. DOI: 10.1007/s10811-010-9637-0.

Cheng, H. et al. (2013). Improvements in ^{230}Th dating, ^{230}Th and ^{234}U half-life values, and U-Th isotopic measurements by multi-collector inductively coupled plasma mass spectrometry. *Earth and Planetary Science Letters* 371-372:82–91. DOI: 10.1016/j.epsl.2013.04.006.

Clark, G. R. II (1999). Organic matrix taphonomy in some molluscan shell microstructures. *Palaeogeography, Palaeoclimatology, Palaeoecology* 149(1-4):305–312. DOI: 10.1016/S0031-0182(98)00208-9.

Clemens, S. C. (1998). Dust response to seasonal atmospheric forcing: Proxy evaluation and calibration. *Paleoceanography* 13(5):471–490. DOI: 10.1029/98PA02131.

Comeau, S. et al. (2010). Larvae of the pteropod *Cavolinia inflexa* exposed to aragonite undersaturation are viable but shell-less. *Marine Biology* 157(10):2341–2345. DOI: 10.1007/s00227-010-1493-6.

Connell, S. D. and B. D. Russell (2010). The direct effects of increasing CO_2 and temperature on non-calcifying organisms: Increasing the potential for phase shifts in kelp forests. *Proceedings of the Royal Society B: Biological Sciences* 277(1686):1409–1415. DOI: 10.1098/rspb.2009.2069.

Cornwall, C. E. and C. L. Hurd (2016). Experimental design in ocean acidification research: Problems and solutions. *ICES Journal of Marine Science* 73(3):572–581. DOI: 10.1093/icesjms/fsv118.

Costa, K. M. et al. (2016). No iron fertilization in the equatorial Pacific Ocean during the last ice age. *Nature* 529(7587):519–522. DOI: 10.1038/nature16453.

Cottingham, K. L. et al. (2005). Knowing when to draw the line: Designing more informative ecological experiments. *Frontiers in Ecology and the Environment* 3(3):145–152. DOI: 10.2307/3868542.

Crafts-Brandner, S. J. and M. E. Salvucci (2000). RuBisCO activase constrains the photosynthetic potential of leaves at high temperature and CO_2. *Proceedings of the National Academy of Sciences* 97(24):13430–13435. DOI: 10.1073pnas.230451497.

Crawley, A. et al. (2010). The effect of ocean acidification on symbiont photorespiration and productivity in *Acropora formosa*. *Global Change Biology* 16(2):851–863. DOI: 10.1111/j.1365-2486.2009.01943.x.

Dammshäuser, A. et al. (2013). Particulate and dissolved aluminum and titanium in the upper water column of the Atlantic Ocean. *Deep Sea Research Part I: Oceanographic Research Papers* 73:127–139. DOI: 10.1016/j.dsr.2012.12.002.

Dason, J. S. et al. (2004). Source of inorganic carbon for photosynthesis in two marine dinoflagellates. *Journal of Phycology* 40(2):285–292. DOI: 10.1111/j.1529-8817.2004.03123.x.

De Schamphelaere, K. A. C. et al. (2005). Toward a biotic ligand model for freshwater green algae: Surface-bound and internal copper are better predictors of toxicity than free Cu^{2+}-ion activity when pH is varied. *Environmental Science and Technology* 39(7):2067–2072. DOI: 10.1021/es049256l.

Deng, F. et al. (2014). Controls on seawater ^{231}Pa, ^{230}Th and ^{232}Th concentrations along the flow paths of deep waters in the Southwest Atlantic. *Earth and Planetary Science Letters* 390:93–102. DOI: 10.1016/j.epsl.2013.12.038.

DePasquale, E. et al. (2015). Vulnerability of early life stage Northwest Atlantic forage fish to ocean acidification and low oxygen. *Marine Ecology Progress Series* 523:145–156. DOI: 10.3354/meps11142.

Devos, N. et al. (1998). RuBisCO adaptation to low temperatures: A comparative study in psychrophilic and mesophilic unicellular algae. *Journal of Phycology* 34(4):655–660. DOI: 10.1046/j.1529-8817.1998.340655.x.

Diaz, R. J. and R. Rosenberg (2008). Spreading dead zones and consequences for marine ecosystems. *Science* 321(5891):926–929. DOI: 10.1126/science.1156401.

Dickson, A. G. (2010). The carbon dioxide system in seawater: Equilibrium chemistry and measurements. In: *Guide to Best Practices for Ocean Acidification Research and Data Reporting*. Ed. by U. Riebesell et al. Luxembourg: Publications Office of the European Union, pp. 17–40.

Dickson, A. G. and F. J. Millero (1987). A comparison of the equilibrium constants for the dissociation of carbonic acid in seawater media. *Deep Sea Research Part A, Oceanographic Research Papers* 34(10):1733–1743. DOI: 10.1016/0198-0149(87)90021-5.

Dickson, A. G. and J. P. Riley (1978). The effect of analytical error on the evaluation of the components of the aquatic carbon-dioxide system. *Marine Chemistry* 6(1):77–85. DOI: 10.1016/0304-4203(78)90008-7.

Dickson, A. G. et al. (2007). Guide to best practices for ocean CO_2 measurements. *PICES Special Publication 3* 3(8):191. DOI: 10.1159/000331784.

Dixon, G. K. and P. J. Syrett (1988). The growth of dinoflagellates in laboratory cultures. *New Phytologist* 109(3):297–302. DOI: 10.1111/j.1469-8137.1988.tb04198.x.

Domingos, R.F. et al. (2015). Metals in the aquatic environment – Interactions and implications for the speciation and bioavailability: A critical overview. *Aquatic Geochemistry* 21(2-4):231–257. DOI: 10.1007/s10498-014-9251-x.

Doney, S. C. et al. (2009). Ocean acidification: The other CO_2 problem. *Annual Review of Marine Science* 1(1):169–192. DOI: 10.1146/annurev.marine.010908.163834.

Doney, S. C. et al. (2012). Climate change impacts on marine ecosystems. *Annual Review of Marine Science* 4(1):11–37. DOI: 10.1146/annurev-marine-041911-111611.

Duce, R. A. and N. W. Tindale (1991). Atmospheric transport of iron and its deposition in the ocean. *Limnology and Oceanography* 36(8):1715–1726. DOI: 10.4319/lo.1991.36.8.1715.

Dutkiewicz, S. et al. (2013). Winners and losers: Ecological and biogeochemical changes in a warming ocean. *Global Biogeochemical Cycles* 27(2):463–477. DOI: 10.1002/gbc.20042.

Ebenezer, V. and J.-S. Ki (2012). Evaluation of the sub-lethal toxicity of Cu, Pb, bisphenol A and polychlorinated biphenyl to the marine dinoflagellate *Cochlodinium polykrikoides*. *Algae* 27(1):63–70. DOI: 10.4490/algae.2012.27.1.063.

Eberlein, T. et al. (2014). Differential effects of ocean acidification on carbon acquisition in two bloom-forming dinoflagellate species. *Physiologia Plantarum* 151(4):468–479. DOI: 10.1111/ppl.12137.

Echeveste, P. et al. (2012). Toxic thresholds of cadmium and lead to oceanic phytoplankton: Cell size and ocean basin-dependent effects. *Environmental Toxicology and Chemistry* 31(8):1887–1894. DOI: 10.1002/etc.1893.

Echigoya, R. et al. (2005). The structures of five new antifungal and hemolytic amphidinol analogs from *Amphidinium carterae* collected in New Zealand. *Harmful Algae* 4(2):383–389. DOI: 10.1016/j.hal.2004.07.004.

Eggleton, J. and K. V. Thomas (2004). A review of factors affecting the release and bioavailability of contaminants during sediment disturbance events. *Environment International* 30(7):973–980. DOI: 10.1016/j.envint.2004.03.001.

Ellis, R. J. (1979). The most abundant protein in the world. *Trends in Biochemical Sciences* 4(11):241–244. DOI: 10.1016/0968-0004(79)90212-3.

Emery, K. O. (1956). Sediments and water of Persian Gulf. *Bulletin of the American Association of Petroleum Geologists* 40(10):2354–2383.

Falkowski, P. G (1998). Biogeochemical controls and feedbacks on ocean primary production. *Science* 281(5374):200–206. DOI: 10.1126/science.281.5374.200.

Falkowski, P. G. (2012). The power of plankton. *Nature* 483(7387):17–20. DOI: 10.1038/483S17a.

Feely, R. A. et al. (2008). Evidence for upwelling of corrosive "acidified" water onto the continental shelf. *Science* 320(5882):1490–1492. DOI: 10.1126/science.1155676.

Feely, R. A. et al. (2010). The combined effects of ocean acidification, mixing, and respiration on pH and carbonate saturation in an urbanized estuary. *Estuarine, Coastal and Shelf Science* 88(4):442–449. DOI: 10.1016/j.ecss.2010.05.004.

Fischer, A. C. et al. (2007). On the relevance of iron adsorption to container materials in small-volume experiments on iron marine chemistry: ^{55}Fe-aided assessment of capacity, affinity and kinetics. *Marine Chemistry* 107(4):533–546. DOI: 10.1016/j.marchem.2007.08.004.

Fitzsimmons, J. N. et al. (2015). Partitioning of dissolved iron and iron isotopes into soluble and colloidal phases along the GA03 GEOTRACES North Atlantic Transect. *Deep Sea Research Part II: Topical Studies in Oceanography* 116:130–151. DOI: 10.1016/j.dsr2.2014.11.014.

Fleisher, M. Q. and R. F. Anderson (2003). Assessing the collection efficiency of Ross Sea sediment traps using ^{230}Th and ^{231}Pa. *Deep Sea Research Part II: Topical Studies in Oceanography* 50(3-4):693–712. DOI: 10.1016/S0967-0645(02)00591-X.

Foyer, C. H. and G. Noctor (2000). Tansley Review No. 112. Oxygen processing in photosynthesis: Regulation and signaling. *New Phytologist* 146(3):359–388. DOI: 10.1046/j.1469-8137.2000.00667.x.

Francois, R. et al. (2004). ^{230}Th normalization: An essential tool for interpreting sedimentary fluxes during the late Quaternary. *Paleoceanography* 19:1–16. DOI: 10.1029/2003PA000939.

Fu, F. X. et al. (2008). A comparison of future increased CO_2 and temperature effects on sympatric *Heterosigma akashiwo* and *Prorocentrum minimum*. *Harmful Algae* 7(1):76–90. DOI: 10.1016/j.hal.2007.05.006.

Fu, F. X. et al. (2012). Global change and the future of harmful algal blooms in the ocean. *Marine Ecology Progress Series* 470:207–233. DOI: 10.3354/meps10047.

Fung, I. Y. et al. (2000). Iron supply and demand in the upper ocean. *Global Biogeochemical Cycles* 14(1):281–295. DOI: 10.1029/1999GB900059.

Gaillardet, J. et al. (1999). Global silicate weathering and CO_2 consumption rates deduced from the chemistry of large rivers. *Chemical Geology* 159(1-4):3–30. DOI: 10.1016/S0009-2541(99)00031-5.

Garilli, V. et al. (2015). Physiological advantages of dwarfing in surviving extinctions in high-CO_2 oceans. *Nature Climate Change* 5(7):678–682. DOI: 10.1038/nclimate2616.

Gazeau, F. et al. (2013). Impacts of ocean acidification on marine shelled molluscs. *Marine Biology* 160(8):2207–2245. DOI: 10.1007/s00227-013-2219-3.

Geyer, W. R. et al. (2004). The transport, transformation and dispersal of sediment by buoyant coastal flows. *Continental Shelf Research* 24(7-8):927–949. DOI: 10.1016/j.csr.2004.02.006.

Glover, C. P. and S. M. Kidwell (1993). Influence of organic matrix on the post-mortem destruction of molluscan shells. *The Journal of Geology* 101(6):729–747. DOI: 10.1086/648271.

Gobler, C. J. and H. Baumann (2016). Hypoxia and acidification in ocean ecosystems: Coupled dynamics and effects on marine life. *Biology Letters* 12(5):20150976. DOI: 10.1098/rsbl.2015.0976.

Gobler, C. J. et al. (2008). Characterization, dynamics, and ecological impacts of harmful *Cochlodinium polykrikoides* blooms on eastern Long Island, NY, USA. *Harmful Algae* 7(3):293–307. DOI: 10.1016/j.hal.2007.12.006.

Gobler, C. J. et al. (2014). Hypoxia and acidification have additive and synergistic negative effects on the growth, survival, and metamorphosis of early life stage bivalves. *PLoS ONE* 9(1):1–10. DOI: 10.1371/journal.pone.0083648.

Godaux, D. et al. (2015). Induction of photosynthetic carbon fixation in anoxia relies on hydrogenase activity and proton-gradient regulation-like-mediated cyclic electron flow in *Chlamydomonas reinhardtii*. *Plant Physiology* 168(2):648–658. DOI: 10.1104/pp.15.00105.

Goldman, J. A. L. et al. (2017). The effects of pH and pCO_2 on photosynthesis and respiration in the diatom *Thalassiosira weissflogii*. *Photosynthesis Research* 132(1):83–93. DOI: 10.1007/s11120-016-0330-2.

Gómez, F. et al. (2017). Molecular characterization and morphology of *Cochlodinium strangulatum*, the type species of *Cochlodinium*, and *Margalefidinium* gen. nov. for *C. polykrikoides* and allied species (Gymnodiniales, Dinophyceae). *Harmful Algae* 63:32–44. DOI: 10.1016/j.hal.2017.01.008.

Gonzàlez-Meler, M. A. et al. (1996). Direct inhibition of plant mitochondrial respiration by elevated CO_2. *Plant Physiology* 112(3):1349–1355. DOI: 10.1104/pp.112.3.1349.

Gorbunov, M. Y. and P. G. Falkowski (2004). Fluorescence Induction and Relaxation (FIRe) technique and instrumentation for monitoring photosynthetic processes and primary production in aquatic ecosystems. In: *Photosynthesis: Fundamental Aspects to Global Perspectives*. Ed. by A. van der Est and D. Bruce. Montreal: Allen Press, pp. 1029–1031.

Gorbunov, M. Y. et al. (2001). Photosynthesis and photoprotection in symbiotic corals. *Limnology and Oceanography* 46(1):75–85. DOI: 10.4319/lo.2001.46.1.0075.

Gruber, N. (2011). Warming up, turning sour, losing breath: Ocean biogeochemistry under global change. *Philosophical Transactions of the Royal Society A: Mathematical, Physical and Engineering Sciences* 369:1980–1996. DOI: 10.1098/rsta.2011.0003.

Gruber, R. K. et al. (2017). Metabolism of a tide-dominated reef platform subject to extreme diel temperature and oxygen variations. *Limnology and Oceanography* 62(4):1701–1717. DOI: 10.1002/lno.10527.

Guillard, R. R. L. and P. E. Hargraves (1993). *Stichochrysis immobilis* is a diatom, not a chrysophyte. *Phycologia* 32(3):234–236. DOI: 10.2216/i0031-8884-32-3-234.1.

Guinotte, J. M. and V. J. Fabry (2008). Ocean acidification and its potential effects on marine ecosystems. *Annals of the New York Academy of Sciences* 1134(1):320–342. DOI: 10.1196/annals.1439.013.

Haake, B. et al. (1993). Seasonality and interannual variability of particle fluxes to the deep Arabian sea. *Deep Sea Research Part I: Oceanographic Research Papers* 40(7):1323–1344. DOI: 10.1016/0967-0637(93)90114-I.

Hackenberg, C. et al. (2009). Photorespiratory 2-phosphoglycolate metabolism and photoreduction of O_2 cooperate in high-light acclimation of *Synechocystis* sp. strain PCC 6803. *Planta* 230(4):625–637. DOI: 10.1007/s00425-009-0972-9.

Halpern, B. S. et al. (2008). A global map of human impact on marine ecosystems. *Science* 319(5865):948–952. DOI: 10.1126/science.1149345.

Han, W. and J. P. McCreary (2001). Modeling salinity distributions in the Indian Ocean. *Journal of Geophysical Research* 106(C1):859–877. DOI: 10.1029/2000JC000316.

Hanghøj, K. et al. (2010). Composition and genesis of depleted mantle peridotites from the Wadi Tayin massif, Oman ophiolite; major and trace element geochemistry, and Os isotope and PGE systematics. *Journal of Petrology* 51(1-2):201–227. DOI: 10.1093/petrology/egp077.

Hargraves, P. E. and L. Maranda (2002). Potentially toxic or harmful microalgae from the northeast coast. *Northeastern Naturalist* 9(1):81–120. DOI: 10.2307/3858576.

Harper, E. M. (2000). Are calcitic layers an effective adaptation against shell dissolution in the Bivalvia? *Journal of Zoology* 251(2):179–186. DOI: 10.1111/j.1469-7998.2000.tb00602.x.

Hattenrath-Lehmann, T. K. et al. (2015). The effects of elevated CO_2 on the growth and toxicity of field populations and cultures of the saxitoxin-producing dinoflagellate *Alexandrium fundyense*. *Limnology and Oceanography* 60(1):198–214. DOI: 10.1002/lno.10012.

Hayes, C. T. et al. (in revision). Oceanic residence times of a spectrum of elements based on thorium supply.

Hayes, C. T. et al. (2013). Quantifying lithogenic inputs to the North Pacific Ocean using the long-lived thorium isotopes. *Earth and Planetary Science Letters* 383:16–25. DOI: 10.1016/j.epsl.2013.09.025.

Hayes, C. T. et al. (2015a). ^{230}Th and ^{231}Pa on GEOTRACES GA03, the U.S. GEOTRACES North Atlantic transect, and implications for modern and paleoceanographic

chemical fluxes. *Deep Sea Research Part II: Topical Studies in Oceanography* 116:29–41. DOI: 10.1016/j.dsr2.2014.07.007.

Hayes, C. T. et al. (2015b). Thorium isotopes tracing the iron cycle at the Hawaii Ocean Time-series Station ALOHA. *Geochimica et Cosmochimica Acta* 169:1–16. DOI: 10.1016/j.gca.2015.07.019.

Hayes, C. T. et al. (2017). Thorium distributions in high- and low-dust regions and the significance for iron supply. *Global Biogeochemical Cycles* 31:328–347. DOI: 10.1002/2016GB005511.

Hays, G. C. et al. (2005). Climate change and marine plankton. *Trends in Ecology and Evolution* 20(6):337–344. DOI: 10.1016/j.tree.2005.03.004.

Henderson, G. M. and R. F. Anderson (2003). The U-series toolbox for paleoceanography. *Reviews in Mineralogy and Geochemistry* 52(1):493–531. DOI: 10.2113/0520493.

Hennon, G. M. M. et al. (2017). Diverse CO_2-induced responses in physiology and gene expression among eukaryotic phytoplankton. *Frontiers in Microbiology* 8:1–14. DOI: 10.3389/fmicb.2017.02547.

Herzi, F. H. et al. (2013). Copper and cadmium effects on growth and extracellular exudation of the marine toxic dinoflagellate *Alexandrium catenella*: 3D-fluorescence spectroscopy approach. *Chemosphere* 93(6):1230–1239. DOI: 10.1016/j.chemosphere.2013.06.084.

Ho, T.-Y. (2013). Nickel limitation of nitrogen fixation in *Trichodesmium*. *Limnology and Oceanography* 58(1):112–120. DOI: 10.4319/lo.2013.58.1.0112.

Ho, T.-Y. et al. (2013). Interrelated influence of light and Ni on *Trichodesmium* growth. *Frontiers in Microbiology* 4:1–6. DOI: 10.3389/fmicb.2013.00139.

Hoffmann, L. J. et al. (2012). Influence of ocean warming and acidification on trace metal biogeochemistry. *Marine Ecology Progress Series* 470:191–205. DOI: 10.3354/meps10082.

Hoins, M. et al. (2016). CO_2-dependent carbon isotope fractionation in dinoflagellates relates to their inorganic carbon fluxes. *Journal of Experimental Marine Biology and Ecology* 481:9–14. DOI: 10.1016/j.jembe.2016.04.001.

Honjo, S. et al. (1999). Monsoon-controlled export fluxes to the interior of the Arabian Sea. *Deep Sea Research Part II: Topical Studies in Oceanography* 46(8-9):1859–1902. DOI: 10.1016/S0967-0645(99)00047-8.

Hood, R. R. et al. (2017). Biogeochemical and ecological impacts of boundary currents in the Indian Ocean. *Progress in Oceanography* 156:290–325. DOI: 10.1016/j.pocean.2017.04.011.

Hsieh, Y.-T. et al. (2011). Combining seawater ^{232}Th and ^{230}Th concentrations to determine dust fluxes to the surface ocean. *Earth and Planetary Science Letters* 312(3-4):280–290. DOI: 10.1016/j.epsl.2011.10.022.

Huang, S.-J. et al. (2009). Carteraol E, a potent polyhydroxyl ichthyotoxin from the dinoflagellate *Amphidinium carterae*. *Tetrahedron Letters* 50(21):2512–2515. DOI: 10.1016/j.tetlet.2009.03.065.

Huh, C.-A. and M. P. Bacon (1985). Thorium-232 in the eastern Caribbean Sea. *Nature* 316(6030):718–721. DOI: 10.1038/316718a0.

Hulburt, E. M. (1957). The taxonomy of unarmored Dinophyceae of shallow embayments on Cape Cod, Massachusetts. *The Biological Bulletin* 112(2):196–219. DOI: 10.2307/1539198.

Hunt, B. P. V. et al. (2008). Pteropods in Southern Ocean ecosystems. *Progress in Oceanography* 78(3):193–221. DOI: 10.1016/j.pocean.2008.06.001.

Huot, Y. and M. Babin (2011). Overview of fluorescence protocols: Theory, basic concepts, and practice. In: *Chlorophyll a Fluorescence in Aquatic Sciences: Methods and Applications*. Ed. by D. J. Suggett et al. Dordrecht: Springer Netherlands, pp. 31–74. DOI: 10.1007/978-90-481-9268-7.

Hutchins, D. A. et al. (1993). Iron and regenerated production: Evidence for biological iron recycling in two marine environments. *Limnology and Oceanography* 38(6):1242–1255. DOI: 10.4319/lo.1993.38.6.1242.

IPCC (2013). Long-term climate change: Projections, commitments and irreversibility. In: *Climate Change 2013: The Physical Science Basis. Contribution of Working Group I to the Fifth Assessment Report of the Intergovernmental Panel on Climate Change*. Ed. by T. F. Stocker et al. Cambridge, pp. 1029–1136.

Ito, A. (2007). Simulated impacts of climate and land-cover change on soil erosion and implication for the carbon cycle, 1901 to 2100. *Geophysical Research Letters* 34(9):1–5. DOI: 10.1029/2007GL029342.

Iwataki, M. et al. (2008). Phylogenetic relationships in the harmful dinoflagellate *Cochlodinium polykrikoides* (Gymnodiniales, Dinophyceae) inferred from LSU rDNA sequences. *Harmful Algae* 7(3):271–277. DOI: 10.1016/j.hal.2007.12.003.

Jenks, A. and S. P. Gibbs (2000). Immunolocalization and distribution of Form II RuBisCO in the pyrenoid and chloroplast stroma of *Amphidinium carterae* and Form I RuBisCO in the symbiont-derived plastics of *Peridinium foliaceum* (Dinophyceae). *Journal of Phycology* 36(1):127–138. DOI: 10.1046/j.1529-8817.2000.99114.x.

Jensen, R. G. (2000). Activation of RuBisCO regulates photosynthesis at high temperature and CO_2. *Proceedings of the National Academy of Sciences* 97(24):12937–12938. DOI: 10.1073/pnas.97.24.12937.

JGOFS (1996). Measurement of chlorophyll *a* and phaeopigments by fluorometric analysis. In: *Protocols for the Joint Global Ocean Flux studies (JGOFS) Core Measurements*. Ed. by A. Knap et al. 19. Bergen: UNESCO, pp. 119–122.

Jickells, T. D. et al. (2005). Global iron connections between desert dust, ocean biogeochemistry, and climate. *Science* 308(5718):67–71. DOI: 10.1126/science.1105959.

Jickells, T. D. et al. (2016). Atmospheric transport of trace elements and nutrients to the oceans. *Philosophical Transactions of the Royal Society A: Mathematical, Physical and Engineering Sciences* 2081(374):1–19. DOI: 10.1098/rsta.2015.0286.

Jordi, A. et al. (2012). Copper aerosols inhibit phytoplankton growth in the Mediterranean Sea. *Proceedings of the National Academy of Sciences* 109(52):21246–21249. DOI: 10.1073/pnas.1207567110.

Juhl, A. R. and M. I. Latz (2002). Mechanisms of fluid shear-induced inhibition of population growth in a red-tide dinoflagellate. *Journal of Phycology* 38(4):683–694. DOI: 10.1046/j.1529-8817.2002.00165.x.

Keeling, R. F. et al. (2010). Ocean deoxygenation in a warming world. *Annual Review of Marine Science* 2(1):199–229. DOI: 10.1146/annurev.marine.010908.163855.

Kienast, S. S. et al. (2016). Tracing dust input to the global ocean using thorium isotopes in marine sediments: ThoroMap. *Global Biogeochemical Cycles* 30(10):1526–1541. DOI: 10.1002/2016GB005408.

Kitaya, Y. et al. (2008). Effects of temperature, photosynthetic photon flux density, photoperiod and O_2 and CO_2 concentrations on growth rates of the symbiotic dinoflagellate, *Amphidinium* sp. *Journal of Applied Phycology* 20(5):737–742. DOI: 10.1007/s10811-008-9331-7.

Klinger, T. et al. (2017). Using integrated, ecosystem-level management to address intensifying ocean acidification and hypoxia in the California Current large marine ecosystem. *Elemental Science of the Anthropocene* 5(16):1–12. DOI: 10.1525/elementa.198.

Kroeker, K. J. et al. (2013). Impacts of ocean acidification on marine organisms: Quantifying sensitivities and interaction with warming. *Global Change Biology* 19(6):1884–1896. DOI: 10.1111/gcb.12179.

Laws, E. A. et al. (1997). Effect of growth rate and CO_2 concentration on carbon isotopic fractionation by the marine diatom *Phaeodactylum tricornutum*. *Limnology and Oceanography* 42(7):1552–1560. DOI: 10.4319/lo.1997.42.7.1552.

Lemeille, S. and J.-D. Rochaix (2010). State transitions at the crossroad of thylakoid signalling pathways. *Photosynthesis Research* 106(1-2):33–46. DOI: 10.1007/s11120-010-9538-8.

Li, G. and D. A. Campbell (2017). Interactive effects of nitrogen and light on growth rates and RuBisCO content of small and large centric diatoms. *Photosynthesis Research* 131(1):93–103. DOI: 10.1007/s11120-016-0301-7.

Li, M. et al. (2016). Phosphorus deficiency inhibits cell division but not growth in the dinoflagellate *Amphidinium carterae*. *Frontiers in Microbiology* 7:1–11. DOI: 10.3389/fmicb.2016.00826.

Lischka, S. and U. Riebesell (2012). Synergistic effects of ocean acidification and warming on overwintering pteropods in the Arctic. *Global Change Biology* 18(12):3517–3528. DOI: 10.1111/gcb.12020.

Lischka, S. et al. (2011). Impact of ocean acidification and elevated temperature on early juveniles of the polar shelled pteropod *Limacina helicina*: Mortality, shell degradation, and shell growth. *Biogeosciences* 8(4):919–932. DOI: 10.5194/bg-8-919-2011.

Liu, J. et al. (2010). Effect of ocean acidification on microbial diversity and on microbe-driven biogeochemistry and ecosystem functioning. *Aquatic Microbial Ecology* 61(3):291–305. DOI: 10.3354/ame01446.

Liu, N. et al. (2017). Elevated CO_2 and associated seawater chemistry do not benefit a model diatom grown with increased availability of light. *Aquatic Microbial Ecology* 79(2):137–147. DOI: 10.3354/ame01820.

Losh, J. L. et al. (2013). RuBisCO is a small fraction of total protein in marine phytoplankton. *New Phytologist* 198(1):52–58. DOI: 10.1111/nph.12143.

Luo, Y. et al. (2010). Sediment $^{231}Pa/^{230}Th$ as a recorder of the rate of the Atlantic meridional overturning circulation: Insights from a 2-D model. *Ocean Science Discussions* 6:381–400. DOI: 10.5194/osd-6-2755-2009.

Maas, A. E. et al. (2015). Transcriptome-wide analysis of the response of the thecosome pteropod *Clio pyramidata* to short-term CO_2 exposure. *Comparative Biochemistry and Physiology Part D: Genomics and Proteomics* 16:1–9. DOI: 10.1016/j.cbd.2015.06.002.

Maas, E. W. et al. (2013). Effect of ocean acidification on bacterial abundance, activity and diversity in the Ross Sea, Antarctica. *Aquatic Microbial Ecology* 70(1):1–15. DOI: 10.3354/ame01633.

Mackey, K. R. M. et al. (2010). Influence of atmospheric nutrients on primary productivity in a coastal upwelling region. *Global Biogeochemical Cycles* 24(4):1–19. DOI: 10.1029/2009GB003737.

Mackey, K. R. M. et al. (2012). Phytoplankton responses to atmospheric metal deposition in the coastal and open-ocean Sargasso Sea. *Frontiers in Microbiology* 3:1–15. DOI: 10.3389/fmicb.2012.00359.

Mackey, K. R. M. et al. (2015). Rapid and gradual modes of aerosol trace metal dissolution in seawater. *Frontiers in Microbiology* 5:1–11. DOI: 10.3389/fmicb.2014.00794.

Mahowald, N. M. et al. (2005). Atmospheric global dust cycle and iron inputs to the ocean. *Global Biogeochemical Cycles* 19(4):1–15. DOI: 10.1029/2004GB002402.

Mahowald, N. M. et al. (2009). Atmospheric iron deposition: Global distribution, variability, and human perturbations. *Annual Review of Marine Science* 1(1):245–278. DOI: 10.1146/annurev.marine.010908.163727.

Mahowald, N. M. et al. (2010). Observed 20th century desert dust variability: Impact on climate and biogeochemistry. *Atmospheric Chemistry and Physics* 10(22):10875–10893. DOI: 10.5194/acp-10-10875-2010.

Manno, C. et al. (2012). *Limacina retroversa*'s response to combined effects of ocean acidification and sea water freshening. *Estuarine, Coastal and Shelf Science* 113:163–171. DOI: 10.1016/j.ecss.2012.07.019.

Manno, C. et al. (2017). Shelled pteropods in peril: Assessing vulnerability in a high CO_2 ocean. *Earth-Science Reviews* 169:132–145. DOI: 10.1016/j.earscirev.2017.04.005.

Manyilizu, M. et al. (2016). Annual cycle of the upper-ocean circulation and properties in the tropical western Indian Ocean. *African Journal of Marine Science* 38(1):81–99. DOI: 10.2989/1814232X.2016.1158123.

Marcantonio, F. et al. (2001). Abrupt intensification of the SW Indian Ocean monsoon during the last deglaciation: Constraints from Th, Pa, and He isotopes. *Earth and Planetary Science Letters* 184(2):505–514. DOI: 10.1016/S0012-821X(00)00342-3.

Martin, J. H. (1990). Glacial-interglacial CO_2 change: The iron hypothesis. *Paleoceanography* 5(1):1–13. DOI: 10.1029/PA005i001p00001.

Martínez-García, A. et al. (2014). Iron fertilization of the subantarctic ocean during the last ice age. *Science* 343(6177):1347–1350. DOI: 10.1126/science.1246848.

McGee, D. et al. (2013). The magnitude, timing and abruptness of changes in North African dust deposition over the last 20,000 yr. *Earth and Planetary Science Letters* 371-372:163–176. DOI: 10.1016/j.epsl.2013.03.054.

McGee, D. et al. (2016). Tracking eolian dust with helium and thorium: Impacts of grain size and provenance. *Geochimica et Cosmochimica Acta* 175:47–67. DOI: 10.1016/j.gca.2015.11.023.

McMinn, A. et al. (2005). Effect of hyperoxia on the growth and photosynthesis of polar sea ice microalgae. *Journal of Phycology* 41(4):732–741. DOI: 10.1111/j.1529-8817.2005.00095.x.

Mehrbach, C. et al. (1973). Measurement of the apparent dissociation constants of carbonic acid in seawater at atmospheric pressure. *Limnology and Oceanography* 18(6):897–907. DOI: 10.4319/lo.1973.18.6.0897.

Mélançon, J. et al. (2015). Effects of dust additions on phytoplankton growth and DMS production in high CO_2 northeast Pacific HNLC waters. *Biogeosciences Discussions* 12(15):12281–12319. DOI: 10.5194/bgd-12-12281-2015.

Melzner, F. et al. (2013). Future ocean acidification will be amplified by hypoxia in coastal habitats. *Marine Biology* 160(8):1875–1888. DOI: 10.1007/s00227-012-1954-1.

Meyer, J. S. et al. (1999). Binding of nickel and copper to fish gills predicts toxicity when water hardness varies, but free-ion activity does not. *Environmental Science and Technology* 33(6):913–916. DOI: 10.1021/es980715q.

Miao, A.-J. et al. (2005). Comparison of Cd, Cu, and Zn toxic effects on four marine phytoplankton by pulse-amplitude-modulated fluorometry. *Environmental Toxicology and Chemistry* 24(10):2603–2611. DOI: 10.1897/05-009R.1.

Millero, F. J. et al. (2009). Effect of ocean acidification on the speciation of metals in seawater. *Oceanography* 22(4):72–85. DOI: 10.5670/oceanog.2009.98.

Milne, A. et al. (2010). Determination of Mn, Fe, Co, Ni, Cu, Zn, Cd and Pb in seawater using high resolution magnetic sector inductively coupled mass spectrometry (HR-ICP-MS). *Analytica Chimica Acta* 665(2):200–207. DOI: 10.1016/j.aca.2010.03.027.

Modaihsh, A. S. (1997). Characteristics and composition of the falling dust sediments on Riyadh city, Saudi Arabia. *Journal of Arid Environments* 36(2):211–223. DOI: 10.1006/jare.1996.0225.

Moffett, A. S. et al. (2015). Biogeochemistry of iron in the Arabian Sea. *Limnology and Oceanography* 60:1671–1688. DOI: 10.1002/lno.10132.

Moore, C. M. (2016). Diagnosing oceanic nutrient deficiency. *Philosophical Transactions of the Royal Society A: Mathematical, Physical and Engineering Sciences* 374(2081):1–20. DOI: 10.1098/rsta.2015.0290.

Moore, C. M. et al. (2009). Large-scale distribution of Atlantic nitrogen fixation controlled by iron availability. *Nature Geoscience* 2(12):867–871. DOI: 10.1038/ngeo667.

Moore, J. K. et al. (2002). Iron cycling and nutrient-limitation patterns in surface waters of the World Ocean. *Deep Sea Research Part II: Topical Studies in Oceanography* 49(1-3):463–507. DOI: 10.1016/S0967-0645(01)00109-6.

Morel, F. M. M. and N. M. Price (2003). The biogeochemical cycles of trace metals in the ocean. *Science* 300(5621):944–947. DOI: 10.1126/science.1083545.

Morton, P. L. et al. (2013). Methods for the sampling and analysis of marine aerosols: Results from the 2008 GEOTRACES aerosol intercalibration experiment. *Limnology and Oceanography: Methods* 11(2):62–78. DOI: 10.4319/lom.2013.11.62.

Murray, J. W. et al. (2015). An inland sea high nitrate-low chlorophyll (HNLC) region with naturally high pCO_2. *Limnology and Oceanography* 60(3):957–966. DOI: 10.1002/lno.10062.

Murray, S. A. et al. (2012). Genetic diversity, morphological uniformity and polyketide production in dinoflagellates (*Amphidinium*, Dinoflagellata). *PLoS ONE* 7(6):1–14. DOI: 10.1371/journal.pone.0038253.

Nishioka, J. et al. (2013). Evidence of an extensive spread of hydrothermal dissolved iron in the Indian Ocean. *Earth and Planetary Science Letters* 361:26–33. DOI: 10.1016/j.epsl.2012.11.040.

Owens, S. A. et al. (2011). Re-evaluating the ^{238}U-salinity relationship in seawater: Implications for the ^{238}U-^{234}Th disequilibrium method. *Marine Chemistry* 127(1-4):31–39. DOI: 10.1016/j.marchem.2011.07.005.

Pavia, F. et al. (in press). Intense hydrothermal scavenging of ^{230}Th and ^{231}Pa in the deep Southeast Pacific. *Marine Chemistry*:1–17. DOI: 10.1016/j.marchem.2017.08.003.

Paytan, A. et al. (2009). Toxicity of atmospheric aerosols on marine phytoplankton. *Proceedings of the National Academy of Sciences* 106(12):4601–4605. DOI: 10.1073/pnas.0811486106.

Pease, P. P. et al. (1998). Aerosols over the Arabian Sea: Geochemistry and source areas for aeolian desert dust. *Journal of Arid Environments* 39(3):477–496. DOI: 10.1006/jare.1997.0368.

Peck, V. L. et al. (2016). Outer organic layer and internal repair mechanism protects pteropod *Limacina helicina* from ocean acidification. *Deep Sea Research Part II: Topical Studies in Oceanography* 127:41–52. DOI: 10.1016/j.dsr2.2015.12.005.

Peckol, P. and J. S. Rivers (1995). Physiological responses of the opportunistic macroalgae *Cladophora vagabunda* (L.) van den Hoek and *Gracilaria tikvahiae* (McLachlan) to environmental disturbances associated with eutrophication. *Journal of Experimental Marine Biology and Ecology* 190(1):1–16. DOI: 10.1016/0022-0981(95)00026-n.

Peltier, G. and P. Thibault (1983). Ammonia exchange and photorespiration in *Chlamydomonas*. *Plant Physiology* 71(4):888–892. DOI: 10.1104/pp.71.4.888.

Peñuelas, J. and J. Llusià (2002). Linking photorespiration, monoterpenes and thermotolerance in *Quercus*. *New Phytologist* 155(2):227–237. DOI: 10.1046/j.1469-8137.2002.00457.x.

Perreault, F. et al. (2011). Effect of cadmium on photosystem II activity in *Chlamydomonas reinhardtii*: Alteration of O-J-I-P fluorescence transients indicating the change of apparent activation energies within photosystem II. *Photosynthesis Research* 107(2):151–157. DOI: 10.1007/s11120-010-9609-x.

Peterhansel, C. et al. (2010). Photorespiration. *The Arabidopsis Book* 8(e0130):1–24. DOI: 10.1199/tab.0130.

Pilson, M. E. Q. (1998). *An Introduction to the Chemistry of the Sea*. Upper Saddle River, NJ: Prentice Hall.

Pope, D. H. (1975). Effects of light intensity, oxygen concentration, and carbon dioxide concentration on photosynthesis in algae. *Microbial Ecology* 2(1):1–16. DOI: 10.1007/BF02010377.

Possmayer, M. et al. (2011). Plasticity of the psychrophilic green alga *Chlamydomonas raudensis* (UWO 241) (Chlorophyta) to supraoptimal temperature stress. *Journal of Phycology* 47(5):1098–1109. DOI: 10.1111/j.1529-8817.2011.01047.x.

Pourmand, A. (2005). Radionuclide and biomarker proxies of past ocean circulation and productivity in the Arabian Sea. *Geophysical Research Letters* 32(10):1–4. DOI: 10.1029/2005GL022612.

Pourmand, A. et al. (2004). Variations in productivity and eolian fluxes in the northeastern Arabian Sea during the past 110 ka. *Earth and Planetary Science Letters* 221(1-4):39–54. DOI: 10.1016/S0012-821X(04)00109-8.

Pourmand, A. et al. (2007). A 28-ka history of sea surface temperature, primary productivity and planktonic community variability in the western Arabian Sea. *Paleoceanography* 22(4):1–14. DOI: 10.1029/2007PA001502.

Qasim, S. Z. (1977). Biological productivity of the Indian Ocean. *Indian Journal of Marine Sciences* 6:122–137.

R Development Core Team (2016). R: A Language and Environment for Statistical Computing. Vienna.

Rabalais, N. N. et al. (2010). Dynamics and distribution of natural and human-caused hypoxia. *Biogeosciences* 7(2):585–619. DOI: 10.5194/bg-7-585-2010.

Rafter, P. A. et al. (2017). Recycled iron fuels new production in the eastern equatorial Pacific Ocean. *Nature Communications* 8(1):1–10. DOI: 10.1038/s41467-017-01219-7.

Raven, J. A. (1997). Inorganic carbon acquisition by marine autotrophs. *Advances in Botanical Research* 27:85–209. DOI: 10.1016/S0065-2296(08)60281-5.

Ren, H. et al. (2015). Glacial-to-interglacial changes in nitrate supply and consumption in the subarctic North Pacific from microfossil-bound N isotopes at two trophic levels. *Paleoceanography* 30(9):1217–1232. DOI: 10.1002/2014PA002765.

Richlen, M. L. et al. (2010). The catastrophic 2008-2009 red tide in the Arabian Gulf region, with observations on the identification and phylogeny of the fish-killing dinoflagellate *Cochlodinium polykrikoides*. *Harmful Algae* 9(2):163–172. DOI: 10.1016/j.hal.2009.08.013.

Ritchie, R. J. (2008). Fitting light saturation curves measured using modulated fluorometry. *Photosynthesis Research* 96(3):201–215. DOI: 10.1007/s11120-008-9300-7.

Robbins, L. L. et al. (2010). CO_2calc: A user-friendly seawater carbon calculator for Windows, Max OS X, and iOS (iPhone). *U. S. Geological Survey Open-File Report 2010-1280*:1–17.

Roberty, S. et al. (2014). PSI Mehler reaction is the main alternative photosynthetic electron pathway in *Symbiodinium* sp., symbiotic dinoflagellates of cnidarians. *New Phytologist* 204:81–91. DOI: 10.1111/nph.12903.

Rowland, G. H. et al. (2017). Investigating the use of $^{232}Th/^{230}Th$ as a dust proxy using co-located seawater and sediment samples from the low-latitude North Atlantic. *Geochimica et Cosmochimica Acta* 214:143–156. DOI: 10.1016/j.gca.2017.07.033.

Roy-Barman, M. (2009). Modelling the effect of boundary scavenging on Thorium and Protactinium profiles in the ocean. *Biogeosciences* 6(12):3091–3107. DOI: 10.5194/bg-6-3091-2009.

Roy-Barman, M. et al. (1996). ^{230}Th-^{232}Th systematics in the central Pacific Ocean: The sources and the fates of thorium. *Earth and Planetary Science Letters* 139(3-4):351–363. DOI: 10.1016/0012-821X(96)00017-9.

Roy-Barman, M. et al. (2009). The influence of particle composition on Thorium scavenging in the Mediterranean Sea. *Earth and Planetary Science Letters* 286(3-4):526–534. DOI: 10.1016/j.epsl.2009.07.018.

Rudnick, R. L. and S. Gao (2003). Composition of the continental crust. In: *Treatise on Geochemistry*. Ed. by R. L. Rudnick. Amsterdam: Elsevier, pp. 1–64. DOI: 10.1016/B0-08-043751-6/03016-4.

Sabine, C. L. et al. (2004). The oceanic sink for anthropogenic CO_2. *Science* 305(5682):367–371. DOI: 10.1126/science.1097403.

Saeedi, H. et al. (2011). Catastrophic impact of red tides of *Cochlodinium polykrikoides* on the razor clam *Solen dactylus* in coastal waters of the northern Persian Gulf. *Journal of the Persian Gulf* 2(6):13–19.

Saunders, P. M. and N. P. Fofonoff (1976). Conversion of pressure to depth in the ocean. *Deep-Sea Research and Oceanographic Abstracts* 23(1):109–111. DOI: 10.1016/0011-7471(76)90813-5.

Schlitzer, R. (2015). Ocean Data View. URL: http://odv.awi.de.

Scholten, J. C. et al. (2005). Radionuclide fluxes in the Arabian Sea: The role of particle composition. *Earth and Planetary Science Letters* 230(3-4):319–337. DOI: 10.1016/j.epsl.2004.11.003.

Schott, F. A. and J. P. McCreary (2001). The monsoon circulation of the Indian Ocean. *Progress in Oceanography* 51(1):1–123. DOI: 10.1016/S0079-6611(01)00083-0.

Schreiber, U. and W. Vidaver (1974). Chlorophyll fluorescence induction in anaerobic *Scenedesmus obliquus*. *Biochimica et Biophysica Acta* 368(1):97–112. DOI: 10.1016/0005-2728(74)90100-5.

Schreiber, U. et al. (1993). PAM fluorometer based on medium-frequency pulsed Xe-flash measuring light: A highly sensitive new tool in basic and applied photosynthesis research. *Photosynthesis Research* 36(1):65–72. DOI: 10.1007/BF00018076.

Schüßler, U. et al. (2005). Dissolved Al distribution, particulate Al fluxes and coupling to atmospheric Al and dust deposition in the Arabian Sea. *Deep-Sea Research Part II: Topical Studies in Oceanography* 52(14-15):1862–1878. DOI: 10.1016/j.dsr2.2005.06.005.

Serno, S. et al. (2014). Eolian dust input to the Subarctic North Pacific. *Earth and Planetary Science Letters* 387:252–263. DOI: 10.1016/j.epsl.2013.11.008.

Shankar, D. et al. (2002). The monsoon currents in the north Indian Ocean. *Progress in Oceanography* 52(1):63–120. DOI: 10.1016/S0079-6611(02)00024-1.

Shi, D. et al. (2010). Effect of ocean acidification on iron availability to marine phytoplankton. *Science* 327(5966):676–679. DOI: 10.1126/science.1183517.

Sirocko, F. and M. Sarnthein (1989). Wind-borne deposits in the northwestern Indian Ocean: Record of Holocene sediments versus modern satellite data. In: *Paleoclimatology and Paleometeorology: Modern and Past Patterns of Global Atmospheric Transport*. Ed. by M. Leinen and M. Sarnthein. Dordrecht: Springer Netherlands, pp. 401–433. DOI: 10.1007/978-94-009-0995-3_17.

Sirocko, Frank et al. (1991). Atmospheric summer circulation and coastal upwelling in the Arabian Sea during the Holocene and the last glaciation. *Quaternary Research* 36(1):72–93. DOI: 10.1016/0033-5894(91)90018-Z.

Sirocko, F. et al. (2000). Processes controlling trace element geochemistry of Arabian Sea sediments during the last 25,000 years. *Global and Planetary Change* 26(1-3):217–303. DOI: 10.1016/S0921-8181(00)00046-1.

Sobrino, C. et al. (2008). Acclimation to elevated carbon dioxide and ultraviolet radiation in the diatom *Thalassiosira pseudonana*: Effects on growth, photosynthesis, and spectral sensitivity of photoinhibition. *Limnology and Oceanography* 53(2):494–505. DOI: 10.4319/lo.2008.53.2.0494.

Srinivas, B. and M. M. Sarin (2013). Atmospheric deposition of N, P and Fe to the Northern Indian Ocean: Implications to C- and N-fixation. *Science of The Total Environment* 456-457:104–114. DOI: 10.1016/j.scitotenv.2013.03.068.

Stegmann, P. M. and N. W. Tindale (1999). Global distribution of aerosols over the open ocean as derived from the Coastal Zone Color Scanner. *Global Biogeochemical Cycles* 13(2):383–397. DOI: 10.1029/1999GB900011.

Steidinger, K. A. and K. Jangen (1996). Dinoflagellates. In: *Identifying Marine Phytoplankton*. Ed. by C. R. Tomas. New York: Academic Press, pp. 387–584.

Strickland, J. D. H. and T. R. Parsons (1972). *A practical handbook of seawater analysis*. 2nd ed. Ottawa: Fisheries Research Board of Canada, pp. 1–310. DOI: 10.1002/iroh.19700550118.

Strong, A. L. et al. (2014). Ocean acidification 2.0: Managing our changing coastal ocean chemistry. *Bioscience* 64(7):581–592. DOI: 10.1093/biosci/biu072.

Suggett, D. J. et al. (2011). Estimating aquatic productivity from active fluorescence measurements. In: *Chlorophyll a Fluorescence in Aquatic Sciences: Methods and Applications*. Ed. by D. J. Suggett et al. Dordrecht: Springer Netherlands, pp. 103–127. DOI: 10.1007/978-90-481-9268-7.

Sunda, W. G. (1989). Trace metal interactions with marine phytoplankton. *Biological Oceanography* 6(5-6):411–442. DOI: 10.1080/01965581.1988.10749543.

Sunda, W. G. (1994). Trace metal/phytoplankton interactions in the sea. In: *Chemistry of Aquatic Systems: Local and Global Perspectives*. Ed. by G. Bidoglio and W. Stumm. Brussels: ECSC, EEC, EAEC, pp. 213–247.

Sunda, W. G. and W.-J. Cai (2012). Eutrophication induced CO_2-acidification of subsurface coastal waters: Interactive effects of temperature, salinity, and atmospheric pCO_2. *Environmental Science and Technology* 46(19):10651–10659. DOI: 10.1021/es300626f.

Sunda, W. G. and S. A. Huntsman (1998). Processes regulating cellular metal accumulation and physiological effects: Phytoplankton as model systems. *Science of the Total Environment* 219(2-3):165–181. DOI: 10.1016/S0048-9697(98)00226-5.

Sunda, W. G. et al. (2005). Trace metal ion buffers and their use in culture studies. In: *Algal Culturing Techniques*. Ed. by R. A. Andersen. Burlington, MA: Elsevier, pp. 35–63.

Tabita, F. R. et al. (2007). Function, structure, and evolution of the RuBisCO-like proteins and their RuBisCO homologs. *Microbiology and Molecular Biology Reviews* 71(4):576–599. DOI: 10.1128/MMBR.00015-07.

Tagliabue, A. et al. (2014). The impact of different external sources of iron on the global carbon cycle. *Geophysical Research Letters* 41(3):920–926. DOI: 10.1002/2013GL059059.

Tagliabue, A. et al. (2016). How well do global ocean biogeochemistry models simulate dissolved iron distributions? *Global Biogeochemical Cycles* 30(2):149–174. DOI: 10.1002/2015GB005289.

Takahashi, S. et al. (2007). Impairment of the photorespiratory pathway accelerates photoinhibition of photosystem II by suppression of repair but not acceleration of damage processes in *Arabidopsis*. *Plant Physiology* 144(1):487–494. DOI: 10.1104/pp.107.097253.

Takeba, G. and A. Kozaki (1998). Photorespiration is an essential mechanism for the protection of C_3 plants from photooxidation. In: *Stress Responses of Photosynthetic Organisms*. Ed. by K. Satoh and N. Murata. Amsterdam: Elsevier, pp. 15–36.

Takeda, S. et al. (1995). Effects of nitrogen and iron enrichments on phytoplankton communities in the Northwestern Indian Ocean. *Marine Chemistry* 50(1–4):229–241. DOI: 10.1016/0304-4203(95)00038-S.

Tang, Y. Z. and C. J. Gobler (2009). *Cochlodinium polykrikoides* blooms and clonal isolates from the northwest Atlantic coast cause rapid mortality in larvae of multiple bivalve species. *Marine Biology* 156(12):2601–2611. DOI: 10.1007/s00227-009-1285-z.

Taylor, S. R. and S. M. McLennan (1995). The geochemical evolution of the continental crust. *Reviews of Geophysics* 33(2):241–265. DOI: 10.1029/95RG00262.

Tcherkez, G. et al. (2008). Respiratory metabolism of illuminated leaves depends on CO_2 and O_2 conditions. *Proceedings of the National Academy of Sciences* 105(2):797–802. DOI: 10.1073/pnas.0708947105.

Tcherkez, G. et al. (2012). Short-term effects of CO_2 and O_2 on citrate metabolism in illuminated leaves. *Plant, Cell and Environment* 35(12):2208–2220. DOI: 10.1111/j.1365-3040.2012.02550.x.

Tindale, N. W. and P. P. Pease (1999). Aerosols over the Arabian Sea: Atmospheric transport pathways and concentrations of dust and sea salt. *Deep Sea Research Part II: Topical Studies in Oceanography* 46(8-9):1577–1595. DOI: 10.1016/S0967-0645(99)00036-3.

Tomczak, M. and J. S. Godfrey (2001). The Indian Ocean. In: *Regional Oceanography: An Introduction*. Delhi: Daya Publishing House, pp. 175–198.

Tortell, P. D. (2000). Evolutionary and ecological perspectives on carbon acquisition in phytoplankton. *Limnology and Oceanography* 45(3):744–750. DOI: 10.4319/lo.2000.45.3.0744.

Turner, A. and G. E. Millward (2002). Suspended particles: Their role in estuarine biogeochemical cycles. *Estuarine, Coastal and Shelf Science* 55(6):857–883. DOI: 10.1006/ecss.2002.1033.

Twining, B. S. and S. B. Baines (2013). The trace metal composition of marine phytoplankton. *Annual Review of Marine Science* 5(1):191–215. DOI: 10.1146/annurev-marine-121211-172322.

Ulstrup, K. E. et al. (2005). Photosynthetic impact of hypoxia on *in hospite* zooxanthellae in the scleractinian coral *Pocillopora damicornis*. *Marine Ecology Progress Series* 286:125–132. DOI: 10.3354/meps286125.

Vaquer-Sunyer, R. and C. M. Duarte (2008). Thresholds of hypoxia for marine biodiversity. *Proceedings of the National Academy of Sciences* 105(40):15452–15457. DOI: 10.1073/pnas.0803833105.

Vu, H. T. D. and Y. Sohrin (2013). Diverse stoichiometry of dissolved trace metals in the Indian Ocean. *Scientific Reports* 3(1745):1–5. DOI: 10.1038/srep01745.

Wallace, R. B. et al. (2014). Coastal ocean acidification: The other eutrophication problem. *Estuarine, Coastal and Shelf Science* 148:1–13. DOI: 10.1016/j.ecss.2014.05.027.

Whitney, S. M. and T. J. Andrews (1998). The CO_2/O_2 specificity of single-subunit ribulose-bisphosphate carboxylase from the dinoflagellate, *Amphidinium carterae*. *Australian Journal of Plant Physiology* 25:131–138. DOI: 10.1071/PP97167.

Wiggert, J. D. et al. (2006). Annual ecosystem variability in the tropical Indian Ocean: Results of a coupled bio-physical ocean general circulation model. *Deep Sea Research Part II: Topical Studies in Oceanography* 53(5-7):644–676. DOI: 10.1016/j.dsr2.2006.01.027.

Winckler, G. et al. (2016). Ocean dynamics, not dust, have controlled equatorial Pacific productivity over the past 500,000 years. *Proceedings of the National Academy of Sciences* 113(22):6119–6124. DOI: 10.1073/pnas.1600616113.

Witt, V. et al. (2011). Effects of ocean acidification on microbial community composition of, and oxygen fluxes through, biofilms from the Great Barrier Reef. *Environmental Microbiology* 13(11):2976–2989. DOI: 10.1111/j.1462-2920.2011.02571.x.

Witter, A. E. et al. (2000). Iron speciation in the Arabian Sea. *Deep Sea Research Part II: Topical Studies in Oceanography* 47(7–8):1517–1539. DOI: 10.1016/S0967-0645(99)00152-6.

Woodward, S. et al. (2005). A simulation of the effect of climate change-induced desertification on mineral dust aerosol. *Geophysical Research Letters* 32(18):2–5. DOI: 10.1029/2005GL023482.

Wu, R. S. S. et al. (2012). Effects of hypoxia on growth of the diatom *Skeletonema costatum*. *Journal of Experimental Marine Biology and Ecology* 420-421:65–68. DOI: 10.1016/j.jembe.2012.04.003.

Wu, Y. et al. (2010). CO_2-induced seawater acidification affects physiological performance of the marine diatom *Phaeodactylum tricornutum*. *Biogeosciences* 7(9):2915–2923. DOI: 10.5194/bg-7-2915-2010.

Xu, Y. et al. (2012). The effect of pH on the uptake of zinc and cadmium in marine phytoplankton: Possible role of weak complexes. *Limnology and Oceanography* 57(1):293–304. DOI: 10.4319/lo.2012.57.1.0293.

Yang, D. et al. (2003). Global potential soil erosion with reference to land use and climate changes. *Hydrological Processes* 17(14):2913–2928. DOI: 10.1002/hyp.1441.

Young, J. N. et al. (2015a). Antarctic phytoplankton down-regulate their carbon-concentrating mechanisms under high CO_2 with no change in growth rates. *Marine Ecology Progress Series* 532:13–28. DOI: 10.3354/meps11336.

Young, J. N. et al. (2015b). Slow carboxylation of RuBisCO constrains the rate of carbon fixation during Antarctic phytoplankton blooms. *New Phytologist* 205(1):172–181. DOI: 10.1111/nph.13021.

Young, J. N. et al. (2016). Large variation in the RuBisCO kinetics of diatoms reveals diversity among their carbon-concentrating mechanisms. *Journal of Experimental Botany* 67(11):3445–3456. DOI: 10.1093/jxb/erw163.

Zhang, Y. et al. (2015). Modeling the global emission, transport and deposition of trace elements associated with mineral dust. *Biogeosciences* 12(19):5771–5792. DOI: 10.5194/bg-12-5771-2015.

Part IV

Appendix

Appendix A

Chapter 2 supplemental material

A.1 Supplemental figures

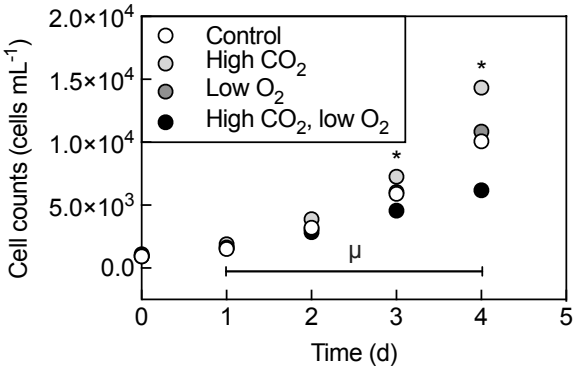

Figure A.1: *Amphidinium carterae* growth curves in the final 4 d of incubation following acclimation (mean ± SEM; n = 4 for all treatments). Growth rates were calculated from exponential increases in cell counts at the last 4 time points from 1 to 4 d. The bar labeled "μ" indicates the time interval over which growth rates were calculated. The asterisk indicates that all treatments were statistically different from the high CO_2, low O_2 treatment at a particular time point (one-way ANOVA, $p < 0.05$).

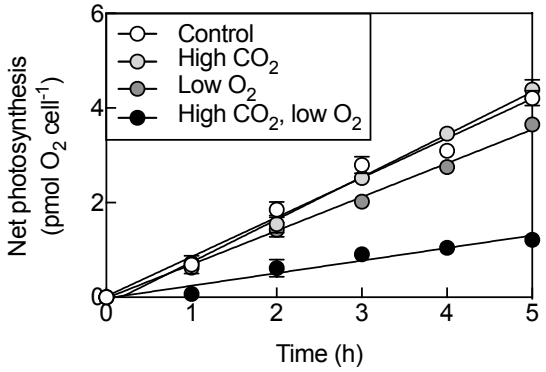

Figure A.2: Representative *Amphidinium carterae* net photosynthesis curves after 7-d incubation (mean ± SEM; n = 4 for all treatments). Rates of net photosynthesis were calculated from the linear increases in O_2 evolution over 5 h (linear regressions).

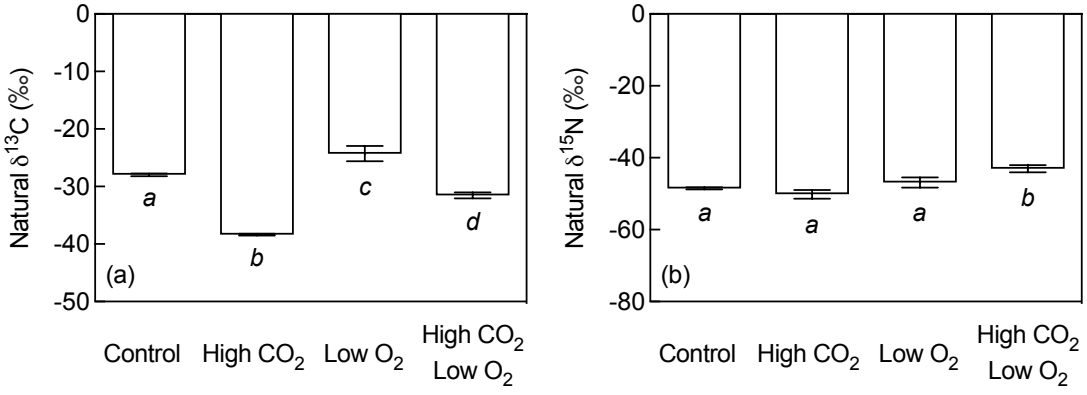

Figure A.3: Natural isotopic δ^{13}C signatures (a) and δ^{15}N signatures (b) of *Amphidinium carterae* cells after 7-d incubation (mean ± SEM; n = 4 for all treatments). Different letters indicate statistical significance compared to the other treatments (one-way ANOVA, $p < 0.05$).

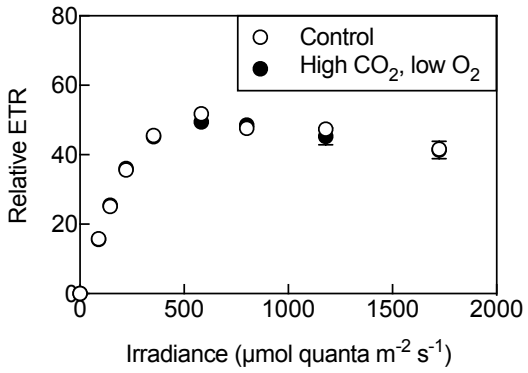

Figure A.4: Photosynthesis-irradiance (PI) curves of relative electron transport rate (ETR) in *Amphidinium carterae* cells as a function of actinic irradiance obtained after 6-h incubation (mean ± SEM; n = 3 for both treatments).

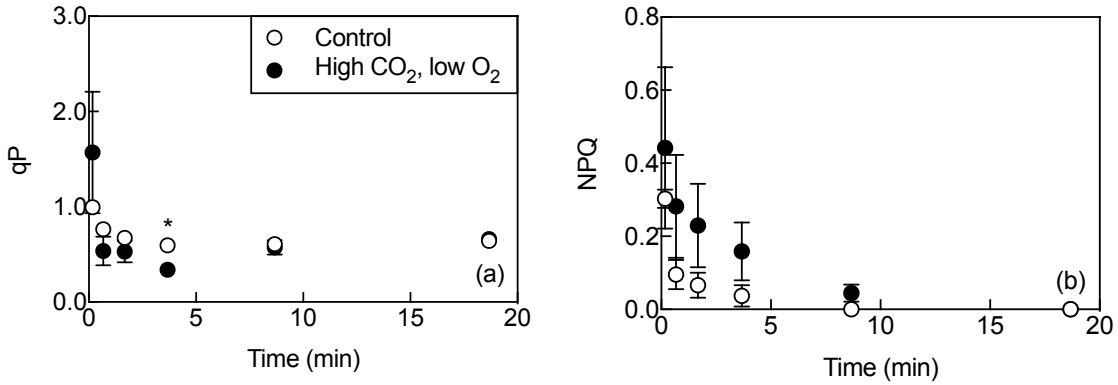

Figure A.5: Photochemical quenching coefficient (qP; a) and nonphotochemical quenching (NPQ; b) in *Amphidinium carterae* cells during recovery of PAM light curve after 6-h incubation (mean ± SEM; n = 3 for both treatments). Note that time reflects recovery time after the actinic light was turned off. The asterisk indicates statistical significance between the treatments at a particular time point (paired t-test, $p < 0.05$).

A.2 Supplemental tables

Table A.1: Daily treatment conditions in the long-term (7-d) *Amphidinium carterae* experiment during the grow-out period following acclimation (mean ± SEM), including number of individual bottles per treatment (N), irradiance (I), temperature (T), salinity (S), pH on the total scale (pH_T), total alkalinity (A_T), partial pressure of carbon dioxide (pCO_2), and dissolved oxygen concentration (O_2).

Treatment	N	I (µmol m^{-2} s^{-1})	T (°C)	S	pH_T	A_T (µmol kg^{-1})	pCO_2 (µatm)	O_2 (µmol L^{-1})
Control								
t_0	4	104.0 ± 4.6	20.0	32	8.18 ± <0.01	2005.0 ± 0.5	242.8 ± 1.7	238.0 ± 8.0
t_1	4	-	19.9	-	8.05 ± 0.01	-	-	230.8 ± 5.5
t_2	4	-	20.0	-	7.97 ± 0.01	-	-	237.3 ± 2.0
t_3	4	-	20.0	-	7.98 ± 0.01	-	-	250.8 ± 1.8
t_4	4	104.8 ± 4.5	19.9	-	7.99 ± 0.01	2056.8 ± 6.9	420.0 ± 10.8	241.7 ± 0.9
High CO_2								
t_0	4	101.8 ± 7.5	19.9	32	7.58 ± 0.01	1988.5 ± 2.8	1171.6 ± 19.7	244.0 ± 1.4
t_1	4	-	19.9	-	7.57 ± <0.01	-	-	246.4 ± 2.8
t_2	4	-	20.0	-	7.61 ± <0.01	-	-	252.6 ± 1.5
t_3	4	-	19.9	-	7.78 ± <0.01	-	-	257.8 ± 3.0
t_4	4	103.5 ± 5.6	20.0	-	7.64 ± 0.01	2122.5 ± 8.9	1086.3 ± 30.5	258.4 ± 3.3
Low O_2								
t_0	4	101.5 ± 7.0	19.9	32	7.83 ± 0.01	1990.6 ± 1.4	631.9 ± 16.0	56.4 ± 2.7
t_1	4	-	20.1	-	7.87 ± <0.01	-	-	56.8 ± 2.0
t_2	4	-	20.0	-	7.91 ± <0.01	-	-	59.7 ± 1.1
t_3	4	-	20.0	-	7.95 ± <0.01	-	-	63.2 ± 1.6
t_4	4	104.5 ± 8.5	19.9	-	8.01 ± <0.01	2006.2 ± 6.0	392.8 ± 5.3	78.3 ± 4.2
High CO_2, low O_2								
t_0	4	100.0 ± 5.6	20.0	32	7.66 ± 0.02	2004.6 ± 1.4	976.6 ± 41.4	61.3 ± 1.8
t_1	4	-	20.0	-	7.57 ± 0.01	-	-	60.0 ± 0.7
t_2	4	-	20.0	-	7.58 ± <0.01	-	-	57.4 ± 1.9
t_3	4	-	20.0	-	7.59 ± <0.01	-	-	62.9 ± 3.3
t_4	4	105.8 ± 5.5	20.0	-	7.59 ± <0.01	2034.2 ± 5.0	1184.5 ± 15.0	57.1 ± 2.6

Table A.2: Macronutrient concentrations in the initial culture media and in the *Amphidinium carterae* media at the end of the long-term (7-d) experiment (mean ± SEM; n = 4 for all treatments), including ammonium (NH_4), nitrite (NO_2), nitrate (NO_3), and orthophosphate (PO_4).

Treatment	NH_4 (mg N L^{-1})	NO_2 (mg N L^{-1})	NO_3 (mg N L^{-1})	PO_4 (mg P L^{-1})
Culture media	0.007 ± 0.001	0.007 ± 0.002	2.743 ± 0.527	1.027 ± 0.006
Control	0.006 ± 0.001	0.021 ± <0.001	7.143 ± 0.858	0.992 ± 0.002
High CO_2	0.003 ± <0.001	0.009 ± 0.002	2.645 ± 0.217	1.059 ± 0.005
Low O_2	0.004 ± 0.000	0.008 ± <0.001	3.995 ± 0.353	1.010 ± 0.002
High CO_2, low O_2	0.005 ± 0.001	0.009 ± <0.001	3.395 ± 0.750	1.043 ± 0.003

Appendix B

Chapter 3 supplemental material

B.1 Supplemental figures

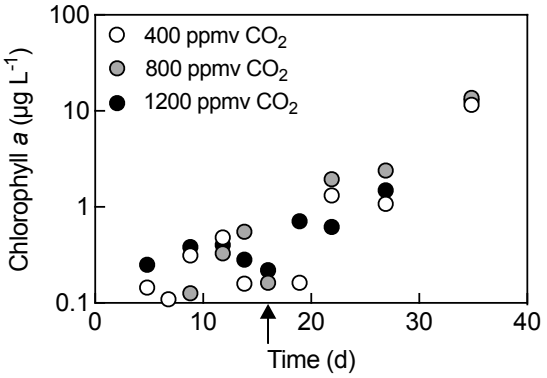

Figure B.1: *Cochlodinium polykrikoides* growth curves from the reference flask (without sediment) in each treatment at 400, 800, and 1200 ppmv CO_2. The arrow indicates the time at which L1 trace metals and EDTA were added to the culture media to initiate growth.

B.2 Supplemental tables

Table B.1: Trace metal content of the size-fractionated sediment from Oman (23.607° N, 58.595° E), compared to upper continental crust (UCC; Rudnick and Gao, 2003) and Oman ophiolite (23.108° N, 58.391° E; Hanghøj et al., 2010).

	Sediment from Oman (ppm)			UCC	Ophiolite
Trace metal	Mean	SEM	n	(ppm)	(ppm)
Fe	25760	730	3	39176	54334
Al	19590	510	3	81501	2276
Ti	979	32	3	3836	102
P	136	8	3	655	22
Cd	0.1	0.0	3	0.09	NR
Ni	454	18	3	47	2241
Cu	21.4	0.9	3	28	10
Zn	23.5	2.5	3	67	NR
Mn	494	24	3	774	883
Co	45.3	1.5	3	17	112
Pb	3.9	0.2	3	17	0.02

NR = not reported

Table B.2: Dissolved oxygen and pH in the *Cochlodinium polykrikoides* growth media with high suspended sediment concentrations at 400, 800, and 1200 ppmv CO_2.

	400 ppmv CO_2			800 ppmv CO_2			1200 ppmv CO_2		
	Mean	SEM	n	Mean	SEM	n	Mean	SEM	n
Dissolved oxygen (µmol L^{-1})									
0 days	211	2	3	217	4	3	207	1	3
7 days	209	3	3	218	6	3	208	2	3
16 days	218	6	3	222	7	3	226	2	3
22 days	211	1	3	210	3	3	206	0	3
35 days	220	6	3	227	9	3	219	2	3
pH_{NBS}									
0 days	8.14	0.01	3	7.93	0.02	3	7.78	0.02	3
7 days	8.12	0.02	3	7.90	0.01	3	7.70	0.05	3
16 days	8.15	0.00	3	7.90	0.02	3	7.74	0.01	3
22 days	8.11	0.01	3	7.84	0.01	3	7.73	0.03	3
35 days	8.12	0.01	2	7.89	0.03	2	7.73	0.01	2

Table B.3: Total dissolved trace metal concentrations in the *Cochlodinium polykrikoides* growth media with high suspended sediment concentrations at 400, 800, and 1200 ppmv CO_2 and in the background L1 media.

	400 ppmv CO_2			800 ppmv CO_2			1200 ppmv CO_2			Background media		
Trace metal	Mean	SEM	n	Mean	SEM	n	Mean	SEM	n	Mean	SEM	n
Fe (nM)												
0 days	2.2	0.1	3	17.0	15.7	2	1.1	0.8	3	4.3	1.8	3
22 days	47.7	26.5	3	25.1	12.1	3	50.3	12.0	3			
35 days	17.2	8.2	3	12.4	3.4	3	77.3	17.0	3			
Cd (nM)												
0 days	0.93	0.00	3	0.91	0.00	3	0.92	0.01	3	0.92	0.02	3
22 days	0.90	0.02	3	0.87	0.09	3	1.05	0.04	3			
35 days	0.91	0.02	3	0.88	0.01	3	1.04	0.08	3			
Ni (nM)												
0 days	57.7	1.2	3	60.8	1.0	3	64.8	4.6	3	57.5	0.9	3
22 days	74.4	2.0	3	95.2	1.9	3	126.4	3.8	3			
35 days	75.9	3.3	3	105.9	3.3	3	130.7	10.0	3			
Cu (nM)												
0 days	23.5	0.1	3	23.4	2.3	3	22.7	0.2	3	25.6	1.5	3
22 days	38.7	13.2	3	29.3	2.0	3	17.2	0.9	3			
35 days	33.4	3.1	3	61.1	18.6	3	30.5	6.3	3			
Zn (nM)												
0 days	266	17	3	533	161	3	344	17	3	679	255	3
22 days	147	28	3	264	51	2	155	13	3			
35 days	407	65	3	453	205	2	326	24	3			
Mn (nM)												
0 days	11.1	0.2	3	14.9	2.0	3	14.0	1.0	3	5.6	1.4	3
22 days	103.6	5.1	3	111.4	7.2	2	102.4	15.4	3			
35 days	133.8	5.2	3	131.3	30.1	3	149.0	11.5	3			
Co (pM)												
0 days	124	4	3	140	3	3	129	1	3	130	7	3
22 days	108	5	3	114	10	2	124	5	3			
35 days	102	7	3	101	4	3	120	3	3			
Pb (pM)												
0 days	402	127	3	2888	2381	3	56	7	3	132	23	3
22 days	133	62	3	192	83	3	52	17	3			
35 days	400	225	3	523	291	3	246	77	3			

Table B.4: Rates of change of total dissolved trace metal concentrations in the *Cochlodinium polykrikoides* growth media with high suspended sediment concentrations at 400, 800, and 1200 ppmv CO_2. Values in italics indicate that the dissolved concentrations increased over time and the rates were significantly different from zero ($p < 0.05$).

Rate of change of trace metal	400 ppmv CO_2			800 ppmv CO_2			1200 ppmv CO_2		
	Mean	SEM	n	Mean	SEM	n	Mean	SEM	n
Fe (nM d^{-1})	0.61	0.74	3	0.09	0.39	3	*2.19*	*0.45*	*3*
Cd (nM d^{-1})	-6.2×10^{-4}	6.8×10^{-4}	3	-8.0×10^{-4}	1.9×10^{-3}	3	3.6×10^{-3}	2.0×10^{-3}	3
Ni (nM d^{-1})	*0.55*	*0.11*	*3*	*1.32*	*0.11*	*3*	*1.99*	*0.35*	*3*
Cu (nM d^{-1})	0.33	0.31	3	1.00	0.46	3	0.17	0.19	3
Zn (nM d^{-1})	3.02	2.98	3	-3.89	6.32	3	-1.36	2.29	3
Mn (nM d^{-1})	*3.60*	*0.24*	*3*	*3.43*	*0.76*	*3*	*3.89*	*0.41*	*3*
Co (pM d^{-1})	-0.65	0.21	3	-1.11	0.18	3	-0.26	0.12	3
Pb (pM d^{-1})	-1.37	6.58	3	0.01	9.38	3	4.85	2.27	3

Table B.5: Macronutrient concentrations in the *Cochlodinium polykrikoides* growth media with high suspended sediment concentrations at 400, 800, and 1200 ppmv CO_2 and in the background L1 media.

	400 ppmv CO_2			800 ppmv CO_2			1200 ppmv CO_2			Background media		
Nutrient	Mean	SEM	n	Mean	SEM	n	Mean	SEM	n	Mean	SEM	n
Phosphate (µM)												
0 days	39.1	0.4	3	38.5	0.3	3	37.3	0.5	3	37.7	0.6	3
5 days	38.0	0.3	3	37.1	0.4	3	35.8	2.3	3			
16 days	36.7	0.5	3	36.6	0.4	3	38.3	0.5	3			
22 days	38.5	0.3	3	38.0	0.9	3	36.3	0.3	3			
35 days	36.5	1.2	3	36.2	0.4	3	32.7	2.6	3			
Nitrate (µM)												
0 days	800	6	3	806	6	3	787	8	3	789	9	3
5 days	780	6	3	787	4	3	715	46	3			
16 days	775	9	3	742	26	3	782	8	3			
22 days	792	3	3	802	9	3	789	6	3			
35 days	764	16	3	785	5	3	692	54	2			
Nitrite (µM)												
0 days	0.0	0.0	3	0.0	0.0	3	0.0	0.0	3	0.0	0.0	3
5 days	0.0	0.0	3	0.0	0.0	3	0.0	0.0	3			
16 days	0.3	0.1	3	0.6	0.1	3	0.1	0.1	3			
22 days	0.6	0.2	3	0.9	0.3	3	0.3	0.3	3			
35 days	2.0	0.6	3	2.0	0.8	3	0.3	0.3	3			
Ammonium (µM)												
0 days	0.4	0.1	3	1.0	0.2	3	0.5	0.1	3	1.8	0.6	3
5 days	1.1	0.4	3	1.7	0.5	3	1.0	0.3	3			
16 days	1.1	0.1	3	0.4	0.1	3	0.3	0.2	3			
22 days	1.4	0.2	3	1.8	0.2	3	1.8	0.4	3			
35 days	2.7	0.2	3	4.4	0.9	3	3.3	0.8	3			
Silicate (µM)												
0 days	22.5	0.2	3	21.8	0.7	3	19.9	0.3	3	21.4	0.2	3
5 days	23.3	0.6	3	22.2	0.2	3	22.1	1.4	3			
16 days	23.3	0.4	3	23.0	0.6	3	24.5	0.1	3			
22 days	23.0	0.4	3	23.3	0.5	3	23.1	0.4	3			
35 days	23.0	0.9	3	23.8	0.2	3	20.1	1.8	3			

Table B.6: *Cochlodinium polykrikoides in vivo* fluorescence and chlorophyll *a* calibration data.

In vivo fluorescence (RFU)			Chlorophyll *a* (µg L^{-1})		
Mean	SEM	n	Mean	SEM	n
4.2	0.0	3	0.2	0.1	3
195.7	8.8	3	21.7	2.2	3
411.9	11.1	3	49.4	1.0	3
818.0	6.5	3	98.8	3.0	3

Table B.7: *Cochlodinium polykrikoides* growth rates in media with high suspended sediment concentrations at 400, 800, and 1200 ppmv CO_2, as well as in the reference flask (without sediment) in each CO_2 treatment.

	Growth rate (d^{-1})			Growth rate of
Treatment	Mean	SEM	n	reference (d^{-1})
400 ppmv CO_2	0.175	0.025	3	0.259
800 ppmv CO_2	0.143	0.006	3	0.202
1200 ppmv CO_2	0.063	0.017	3	0.256

Table B.8: *Cochlodinium polykrikoides* growth rates at ambient CO_2 under a range of total added Cd or Ni concentrations (without sediment).

Added total trace metal (nM)	Growth rate (d^{-1})		
	Mean	SEM	n
Cd			
0	0.184	0.006	3
0.3	0.160	0.003	3
0.6	0.146	0.006	3
1.5	0.121	0.000	3
3.0	0.124	0.001	3
Ni			
10	0.184	0.006	3
30	0.143	0.004	3
60	0.123	0.002	3
150	0.118	0.002	3
300	0.122	0.005	3

Table B.9: Inhibition of *Cochlodinium polykrikoides* growth rates (%) relative to the positive control at ambient CO_2 under a range of total added Cd or Ni concentrations (without sediment).

Added total trace metal (nM)	Growth rate inhibition (%) Mean	SEM	n
Cd			
0	0.0	0.1	3
0.3	12.9	0.9	3
0.6	20.7	2.0	3
1.5	34.5	2.0	3
3.0	32.6	1.9	3
Ni			
10	0.0	0.1	3
30	22.6	1.6	3
60	33.5	2.2	3
150	35.9	2.3	3
300	33.6	3.2	3

Table B.10: Calculated α and P_{max} parameters (mean ± SEM; n = 3 for all treatments), derived from the *Cochlodinium polykrikoides* PI curves (without sediment). Values in italics indicate statistical significance compared to the 0 nM treatment based on pair-wise comparisons of one-way ANOVA ($p < 0.05$).

Added total trace metal (nM)	α Mean	SEM	n	P_{max} (µmol electrons m^{-2} s^{-1}) Mean	SEM	n
Cd						
0	32.2	0.5	3	13972	475	3
0.3	*28.1*	*0.9*	*3*	*11088*	*625*	*3*
0.6	*26.6*	*0.8*	*3*	*9427*	*459*	*3*
1.5	*25.2*	*0.8*	*3*	*8514*	*403*	*3*
3.0	*22.3*	*0.9*	*3*	*7644*	*541*	*3*
Ni						
10	31.7	1.4	3	23713	2679	3
30	33.9	1.6	3	*18748*	*1095*	*3*
60	*35.8*	*0.9*	*3*	*14862*	*605*	*3*
150	34.9	0.7	3	*13810*	*758*	*3*
300	33.1	1.3	3	*13566*	*516*	*3*

Table B.11: Major components of seawater at salinity = 34, used as inputs in Visual MINTEQ.

Component	Concentration (M)
Na	4.67×10^{-1}
K	1.02×10^{-2}
Mg	5.26×10^{-2}
Ca	1.02×10^{-2}
Sr	9.01×10^{-5}
Cl	5.43×10^{-1}
SO_4	2.81×10^{-2}
HCO_3	2.05×10^{-3}
Br	8.40×10^{-4}
$B(OH)_3$	4.14×10^{-4}
F	6.80×10^{-5}

Table B.12: Example of major components of L1 media, used as inputs in Visual MINTEQ for the 10 nM Ni bioassay treatment.

Component	Concentration (M)
Na	9.42×10^{-4}
K	2.00×10^{-8}
Mn	9.09×10^{-7}
Zn	8.00×10^{-8}
Co	5.04×10^{-8}
Cu	1.00×10^{-8}
Ni	1.00×10^{-8}
Fe	1.17×10^{-5}
Se	1.00×10^{-8}
V	1.00×10^{-8}
Cl	3.76×10^{-5}
SO_4	1.00×10^{-7}
NO_3	8.82×10^{-4}
MoO_4	8.22×10^{-8}
CrO_4	1.00×10^{-8}
PO_4	3.62×10^{-5}
EDTA	1.17×10^{-5}

Appendix C

Chapter 5 supplemental material

C.1 Supplemental figures

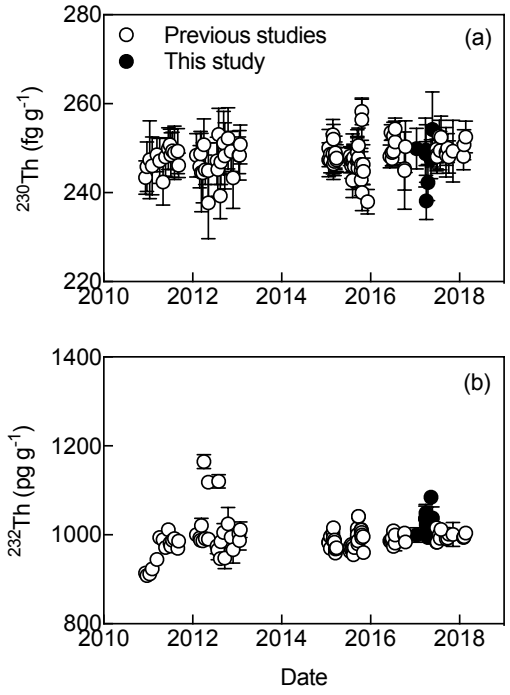

Figure C.1: Intercomparison of (a) ^{230}Th and (b) ^{232}Th in seawater standards from previous studies at Lamont-Doherty Earth Observatory and from this study.

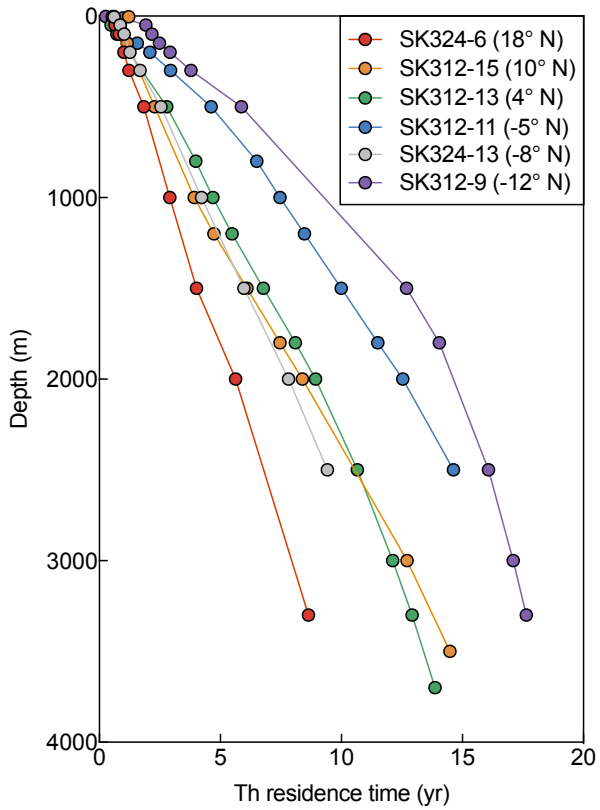

Figure C.2: Residence times of Th (yr) as a function of integration depth in the Indian Ocean (calculated using Equation 5.2). Stations are listed from north to south.

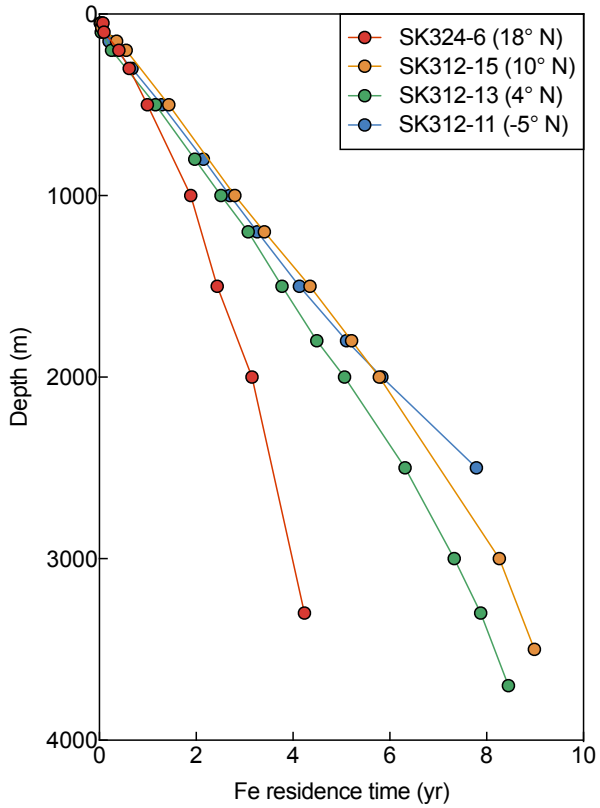

Figure C.3: Residence times of dissolved Fe (yr) as a function of integration depth in the Indian Ocean (calculated using Equation 5.6). Stations are listed from north to south.

C.2 Supplemental tables

Table C.1: Dissolved Th-derived dust fluxes from this study compared to model-derived fluxes (Mahowald et al., 2005).

Cruise-Station	Latitude	Longitude	Sample dust flux ($g\ m^{-2}\ yr^{-1}$)	Model dust flux ($g\ m^{-2}\ yr^{-1}$)
SK324-6	18.17	65.00	10.10	14.50
SK312-15	10.00	65.00	7.11	3.74
SK312-13	4.00	65.00	5.51	2.28
SK312-11	-5.27	67.90	3.02	0.38
SK324-13	-8.30	58.63	7.51	0.22
SK312-9	-12.00	65.00	2.91	0.16

Table C.2: Core-top sediment-derived dust fluxes from this study compared to model-derived fluxes (Mahowald et al., 2005).

Cruise-Core ID	Latitude	Longitude	Sample dust flux ($g\ m^{-2}\ yr^{-1}$)	Model dust flux ($g\ m^{-2}\ yr^{-1}$)
RC17-114TW	19.19	66.29	5.28	14.66
VM34-094TW	18.61	65.18	7.91	14.50
VM34-112TW	17.97	66.23	5.08	14.15
RC27-061TW	16.60	59.90	3.63	10.82
RC17-112TW	11.29	66.02	3.61	4.52
VM34-097TW	10.67	64.48	3.28	4.46
VM34-128TW	9.72	66.41	4.45	3.86
VM34-131TW	9.19	63.78	3.49	4.49
VM19-188TW	6.87	60.67	1.28	4.80
RC17-111TW	6.13	64.83	3.33	3.48
VM14-100TW	3.87	65.52	4.14	2.17
VM34-134TW	3.77	60.50	1.85	3.02
VM14-096TW	-2.83	66.30	0.97	0.68
RC12-330TW	-2.83	67.72	1.58	0.70
VM29-045TW	-6.00	69.82	0.79	0.32
RC17-099TW	-12.30	64.74	0.67	0.16
RC17-100TW	-12.35	63.67	0.45	0.16
RC17-098TW	-13.22	65.62	0.29	0.15

Table C.3: Core-top sediment-derived dust fluxes from Scholten et al. (2005) compared to model-derived fluxes (Mahowald et al., 2005).

Core ID	Latitude	Longitude	Sample dust flux ($g\ m^{-2}\ yr^{-1}$)	Model dust flux ($g\ m^{-2}\ yr^{-1}$)
422	24.41	59.04	16.96	25.72
87KG	23.59	64.22	25.67	17.92
KS8	23.47	59.19	41.05	22.43
419	22.50	61.94	20.68	17.93
95KG	22.49	65.65	16.36	14.32
417	22.18	62.67	19.02	17.14
232SK	21.78	64.60	10.68	13.12
44-1MC	21.61	61.90	4.96	15.81
51KL	20.97	65.56	8.80	13.35
57KL	20.91	63.12	9.10	13.53
37-6MC	20.57	60.05	11.21	16.66
223SK	20.07	66.88	9.32	14.25
3-9MC	19.62	65.83	7.35	13.91
64KL	19.08	64.68	8.59	13.79
14-1MC	17.69	57.75	4.49	14.27
70KL	17.51	61.70	4.75	11.52
36KL	17.07	69.04	6.00	12.54
71KL	16.24	60.26	8.72	10.62
8-1MC	16.17	59.77	3.83	10.82
17-1MC	16.17	59.77	1.44	10.82
918B	15.98	52.85	7.19	21.14
917B	15.91	53.03	6.41	20.54
313B	15.89	53.01	7.07	20.54
4-11MC	15.55	68.57	7.65	11.03
26KL	15.51	68.76	5.37	11.03
15KL	14.88	66.75	3.02	8.21
246K	14.54	51.04	5.74	15.95
923B	14.51	51.68	14.40	15.95
5-11MC	14.44	64.56	3.20	8.83
74KL	14.32	57.35	3.27	12.00
929B	13.71	53.24	4.90	14.07
285K	12.84	47.35	10.10	12.57
82KL	12.68	58.68	3.15	6.89
231K	12.67	50.94	11.70	21.76
105KK	11.27	53.54	2.72	12.83
906B	10.81	52.13	4.74	20.65
915B	10.69	53.52	3.40	12.21
325B	10.68	53.55	3.21	12.21
87KL	10.50	57.74	1.88	5.21
SO117-7	10.16	65.00	4.26	3.97
SO117-18	10.08	64.98	7.08	4.46
93GB	9.92	57.71	1.94	4.94
182SK	8.77	73.70	4.51	4.74
114KK	8.01	51.21	2.93	8.91
SO117-12	8.00	65.00	4.24	3.59
3KL	7.20	61.56	2.13	4.55
7KL	5.91	60.63	1.72	4.29
SO177-3	5.91	64.90	3.60	3.17
11KL	5.39	60.25	1.07	4.29
18KL	1.90	67.34	0.67	1.39
143KK	1.25	44.78	9.86	1.03